BEATRIZ TORRÃO PEREIRA

GELATIN-BASED MEMBRANE FOR ENHANCED PERIODONTAL TISSUE REGENERATION

Dissertation to obtain the Master of Science Degree in Biomedical Engineering

SUPERVISOR

Professor Doctor Catarina Ferreira dos Santos

November 2025

PRR Plano de Recuperação e Resiliência
REPÚBLICA PORTUGUESA
Financiado pela União Europeia NextGenerationEU

BEATRIZ
TORRÃO PEREIRA

GELATIN-BASED MEMBRANE FOR ENHANCED PERIODONTAL TISSUE REGENERATION

EXAMINATION COMMITTEE

Chairperson: Professor Doctor Célio Gabriel Figueiredo Pina, Instituto Politécnico de Setúbal
Supervisor: Professor Doctor Catarina Ferreira dos Santos, Instituto Politécnico de Setúbal
Member of the Committee: Professor Doctor Marta Marques Alves, Instituto Superior Técnico

November 2025

"Now is the time to understand more,

so that we may fear less."

— Marie Curie

Acknowledgments

Gostaria de expressar a minha maior gratidão à minha orientadora, Professora Doutora Catarina Santos, por todo o apoio, e constante encorajamento ao longo deste percurso. A sua confiança em mim e a forma inspiradora como partilha o seu conhecimento e experiência foram essenciais para o meu crescimento. Graças à sua orientação, pude desenvolver este projeto com maior independência, rigor e confiança.

Agradeço também à Escola Superior de Tecnologia de Setúbal, do Instituto Politécnico de Setúbal, por me ter proporcionado a base sólida de conhecimentos e competências que sustentam este trabalho. As oportunidades oferecidas ao longo do mestrado contribuíram tanto para o meu desenvolvimento profissional como pessoal, e estou extremamente grata por todas elas.

Expresso ainda a minha sincera gratidão à Professora Doutora Maria Helena Fernandes bem como à Professora Doutora Liliana Grenho, da Faculdade de Medicina Dentária da Universidade do Porto, e à Professora Doutora Joana Marto, da Faculdade de Farmácia da Universidade de Lisboa, pelas suas valiosas contribuições. Da FFUL, agradeço também à Mestre Sara Bom pela sua ajuda e atenção. As suas perspetivas, vindas de diferentes áreas de conhecimento, enriqueceram de forma significativa este trabalho.

Ao Instituto Superior Técnico, agradeço pela disponibilização dos equipamentos que tornaram possível a concretização de parte experimental deste projeto.

Aos meus colegas e amigos de laboratório, Bruno, Pedro, Ricardo, Rodrigo, Ruben, Sara, Tiago e Tomé, deixo um enorme obrigado pela entreajuda, pela boa disposição e por tornarem cada dia no laboratório mais leve. As vossas perspetivas e a vossa amizade transformaram o trabalho numa experiência verdadeiramente enriquecedora, com um ambiente que nunca esquecerei.

Aos meus amigos fora do meio académico, obrigada pela amizade, pela compreensão e pelos momentos de descontração que me ajudaram a manter o equilíbrio ao longo deste percurso. Um agradecimento especial ao Francisco, pelo apoio incondicional, pela paciência, e por me ajudar a tentar resolver todos os problemas.

Por fim, quero expressar a minha gratidão aos meus pais e à minha família. Obrigada por acreditarem em mim, e por me darem as bases que tornaram possível chegar até aqui.

Resumo

Esta dissertação desenvolveu hidrogéis de gelatina-policaprolactona funcionalizados com nanopartículas inorgânicas para potenciar a regeneração periodontal. Foram sintetizadas nanopartículas de hidroxiapatite, fosfato tricálcico com substituições de ferro e carbonato de cálcio, cuja caracterização confirmou elevada cristalinidade e morfologias nanométricas distintas. Ensaios biológicos demonstraram boa citocompatibilidade para todas as partículas, evidenciando atividade osteogénica através do aumento da atividade de fosfatase alcalina em culturas de linha celular MG-63, células de osteossarcoma humano semelhantes a fibroblastos. A incorporação das nanopartículas nos hidrogéis originou estruturas com diferentes perfis de degradação e modificações nas propriedades reológicas. As análises de gelificação revelaram intervalos térmicos adequados para impressão 3D por extrusão, permitindo produzir membranas homogéneas e estáveis. Entre as composições estudadas, o hidrogel contendo carbonato de cálcio apresentou a maior estabilidade *in vitro*, menor taxa de degradação, mantendo uma boa imprimibilidade. Estes resultados demonstram o seu potencial como biomaterial personalizável para regeneração periodontal, promovendo condições favoráveis à formação de novo tecido ósseo.

Palavras-chave: Hidrogel, Funcionalização, Nanopartículas, Impressão 3D, Regeneração do tecido ósseo, Aplicações periodontais

Abstract

This dissertation developed gelatin–polycaprolactone hydrogels functionalized with inorganic nanoparticles to enhance periodontal regeneration. Hydroxyapatite nanoparticles, iron-substituted tricalcium phosphate, and calcium carbonate were synthesized, and their characterization confirmed high crystallinity and distinct nanoscale morphologies. Biological assays demonstrated good cytocompatibility for all particles, revealing osteogenic activity through increased alkaline phosphatase activity in MG-63 cultures, a human osteosarcoma cell line with fibroblast-like characteristics. Incorporating the nanoparticles into the hydrogels yielded structures with varying degradation profiles and alterations in rheological properties. Gelation analyses indicated thermal windows suitable for extrusion-based 3D printing, enabling the production of homogeneous and stable membranes. Among the compositions investigated, the hydrogel containing calcium carbonate showed the greatest in vitro stability and the lowest degradation rate while maintaining good printability. These results highlight its potential as a customizable biomaterial for periodontal regeneration, fostering conditions conducive to new bone tissue formation.

Keywords: Hydrogel, Functionalization, Nanoparticles, 3D printing, Bone tissue regeneration, Periodontal applications

Table of Contents

List of Figures

List of Tables

List of Acronyms

3D	three-dimensional
2D	two-dimensional
α-TCP	α-tricalcium phosphate
β-TCP	β-tricalcium phosphate
ACP	Amorphous calcium phosphate
ALP	Alkaline Phosphatase
ATR-FTIR	Attenuated Total Reflectance Fourier Transform Infrared
BET	Brunauer-Emmett-Teller
$C_6H_8O_7 \cdot H_2O$	Citric acid monohydrate
Ca^{2+}	Calcium ion
$CaCO_3$	Calcium carbonate
$(Ca(NO_3)_2 \cdot 4H_2O$	Calcium nitrate tetrahydrate
CaO_2	Calcium peroxide
CaP	Calcium phosphate
Ca/P	Calcium-to-phosphorus
CDHA	Calcium-deficient hydroxyapatite
CO_3^{2-}	Carbonate ion
DCPA	Dicalcium phosphate anhydrous
DCPD	Dicalcium phosphate dihydrate
EDS	Energy Dispersive Spectroscopy
HAp	Hydroxyapatite
FC	Field-cooled

Fe	Iron
Fe^{3+}	Trivalent form of iron
$Fe(NO_3)_2 \cdot 4H_2O$	Iron(II) nitrate tetrahydrate
Fe-β-TCP	Iron-*β*-Tricalcium phosphate
H^+	Hydrogen ion
H_2O	Water
H_2O_2	Hydrogen peroxide
HCl	Hydrochloric acid
HCO_3^-	Hydrogen carbonate
HPO_4^{2-}	Monohydrogen phosphate ion
IEP	Isoelectric Point
IS	Isomer Shift values
JCPDS	Joint Committee on Powder Diffraction Standards
M(B)	Isothermal magnetization curves
MCPA	Monocalcium phosphate anhydrous
MCPM	Monocalcium phosphate monohydrate
NaOH	Sodium hydroxide
NaCl	Sodium chloride
NH_4OH	Ammonium hydroxide solution
$(NH_4)_2HPO_4$	Ammonium hydrogen phosphate
NPs	Nanoparticles
OCP	Octacalcium phosphate
OH^-	Hydroxide ion

PCL	Polycaprolactone
PLGA	Poly(lactic-co-glycolic) acid
$P_2O_7^{4-}$	pyrophosphate ion
PO_4^{3-}	Phosphate ion
PZC	Point of zero change
SBF	Simulated body fluid
SEM	Scanning Electron Microscopy
SQUID	Superconducting quantum interference device
XAS	X-Ray absorption spectroscopy
XRD	X-Ray diffraction
ZFC	Zero-field-cooled

List of Symbols

°	Degree
°C	Degrees Celsius
°C/min	Degrees Celsius per minute
µm	Micrometre
µg	Microgram
µL	Microlitre
µg/mL	Microgram per milliliter
cm	Centimeter
cm^3/g	Cubic centimeter per gram
g/mol	Grams per mole
h	Hours
M	Mole
mM	Milimole
mm	Millimeter
mm/min	Millimeters per minute
mm/s	Millimeters per second
mg	Milligram
m^2/g	Square meters per gram
mL	Milliliter
min	Minute
mV	Milivolt
nm	Nanometer

pH	$-\log_{10}[M^+]$
PSI	Pound-Force per Square Inch
rpm	Rotations per minute
w/v	Weight per volume

Chapter 1
Introduction

This chapter provides the framework for the dissertation by presenting the scientific and clinical motivations that led to the development of this research and the structure of the document.

1.1. Motivation

This dissertation is driven by the need to optimize the performance of gelatin-based hydrogels for biomedical applications, particularly in the context of periodontal therapy. Although gelatin-based hydrogels are widely acknowledged for their biocompatibility and feasibility with 3D printing technologies, their fast degradation rate in aqueous environments poses a significant limitation in clinical applications, where effective biofilm control and bone regeneration require sustained drug release from incorporated nanoparticles (NPs) or therapeutic agents. This study aims to address the challenge by enhancing the degradation profile of these hydrogels with a synthetic, biodegradable polymer while maintaining their structural integrity, printability, and biological compatibility. The personalized nature of three-dimensional (3D) printing enables the fabrication of patient-specific therapeutic membranes, offering promising avenues for individualized treatment strategies. By integrating advanced biomaterials with precision additive manufacturing, this work aims to contribute to the development of more effective, customizable, and regenerative solutions for managing periodontal disease.

1.2. Problem statement

Periodontitis is a persistent inflammatory condition affecting the periodontium. In its more severe stages, the disease results in the degradation of the alveolar bone and the progressive detachment of the periodontal ligament [1]. It represents the most prevalent oral health issue among humans, with recent epidemiological data estimating that approximately 62% of the global population is affected by moderate forms of the disease. In comparison, 23.6% endure its most severe stages [2]. Several critical limitations, including a lack of individualized treatment strategies, limited application, and financial constraints of emerging technologies, hinder current therapeutic approaches to periodontal disease. These shortcomings stress the urgent need for innovative methodologies, particularly those producing personalized membranes tailored to patient-specific anatomical and pathological conditions, which could be achieved by employing 3D printing techniques. This dissertation aims to address these deficiencies through the development of a novel approach that integrates a novel gelatin-based hydrogel with NPs with properties ideal for tissue regeneration and biofilm degradation, ultimately striving to enhance clinical outcomes.

1.3. Research objectives

The principal aim of this research is to design and fabricate composite, gelatin-based membranes using 3D printing technologies, with enhanced degradation control and multifunctional therapeutic capabilities. Specifically, the objectives of this work are as follows:

- To produce and incorporate NPs conferring osteoinductive, antimicrobial, and anti-inflammatory functionalities to the hydrogels;
- To develop a hydrogel formulation that balances controlled biodegradation with optimal printability;
- To evaluate the structural and biological properties of the fabricated membranes.

Through these objectives, this dissertation aims to innovate and advance the synthesis of nanomaterials and hydrogel formulations tailored for periodontal tissue regeneration, while demonstrating the potential of additive manufacturing as a versatile platform for translational biomedical applications.

1.4. Academic publications related to the thesis

During the course of this research, the results and findings have been disseminated through both a peer-reviewed publication and scientific conferences. A review article entitled “Oxygen-releasing Calcium Peroxide Nanoparticles for Biomedical Applications: From Synthesis to Clinical Relevance” was submitted, addressing a significant gap in the existing literature regarding the analysis of current synthesis methods and characterization of these NPs.

Additionally, the research was presented at two national scientific meetings, including a poster presentation entitled “Development of Composite Gelatin-Based 3D Membrane for Wound Healing”, authored by Beatriz Pereira, Joana Marto, and Catarina Santos, delivered at the Centro de Química Estrutural in May 2025. Furthermore, an oral presentation entitled “Development of Composite Gelatin-Based 3D Membrane for Periodontitis Treatment”, also by Beatriz Pereira, Joana Marto, and Catarina Santos, was given at the Congresso Nacional de Biomecânica in February 2025.

1.5. Dissertation organization

This dissertation is organized into five main chapters, each designed to provide a comprehensive and logical progression of the research work developed throughout this project.

- **Chapter 1** – Introduction: This chapter presents the general context and motivation behind the study, defines the main research problem, outlines the scientific objectives pursued, and presents the academic publications resulting from this work. A brief description of the dissertation structure is also provided.

- **Chapter 2** – Literature Review: This chapter offers an overview of periodontitis, focusing on its characterization, current treatment approaches, and their limitations. It establishes the clinical context that sustains the problem statement and guides the formulation of the research objectives addressed in the subsequent chapters.

- **Chapter 3** – Production of NPs for osteoinductive applications in periodontal treatment: This chapter, organized as a paper, is dedicated to the synthesis and characterization of different particles, including calcium phosphate (CaP) and calcium carbonate ($CaCO_3$).

- **Chapter 4** – 3D Printing of functionalized hydrogels for periodontal regeneration: This chapter explores the development and characterization of functionalized hydrogels based on gelatin and poly(ε-caprolactone) (PCL), designed for 3D printing applications in periodontal regeneration. The chapter, also organized as a paper, includes hydrogel formulation, characterization, printing optimization, and biological assessments.

- **Chapter 5** – Conclusion: The final chapter summarizes the main findings of the research, highlighting the contributions to the field and identifying potential directions for future work.

This structure ensures a coherent and methodical presentation of the research, enabling a clear understanding of the scientific motivation, experimental development, and outcomes achieved throughout the project.

Chapter 2
Literature review

2.1. Periodontitis – Characterization and treatments

Periodontal disease represents a significant global health concern, affecting millions of individuals and posing serious risks to both oral and systemic health. Recent epidemiological data estimate that approximately 62% of the worldwide population is affected by moderate forms of the disease, while 23.6% endure its most severe stages [2]. Periodontitis is primarily characterized by chronic inflammation and the progressive destruction of the periodontium, the specialized tissues that provide structural support to teeth. This condition is intricately associated with bacterial biofilms that trigger an immune response, ultimately leading to tissue degradation and alveolar bone loss, as illustrated in Figure 2.1 [3].

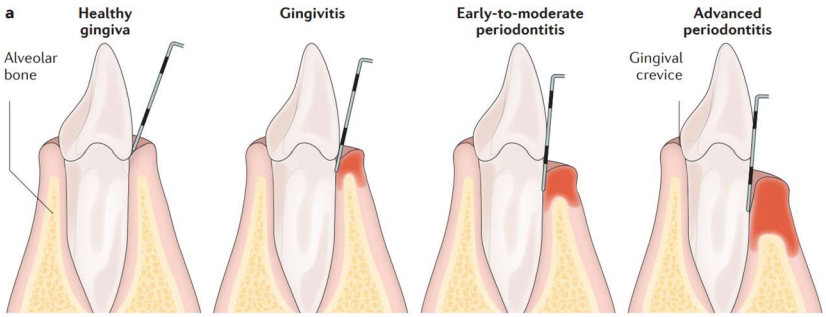

Figure 2.1 – Main stages of periodontal disease, retrieved from [3].

The primary initiating factor of periodontal disease is the accumulation of a complex microbial biofilm, commonly referred to as dental plaque, on the surfaces of teeth and the gingiva [4]. This biofilm comprises a highly diverse microbial community, with over 150 bacterial species typically identified in a single individual and more than 800 species identified across human populations. The microbial etiology of periodontitis is no longer attributed to a single pathogen but rather to a state of microbial dysbiosis, an imbalance within the commensal oral microbiota, that perturbs host-microbial homeostasis and initiates an inflammatory cascade [5].

While historically some bacterial species, such as *Porphyromonas gingivalis*, *Tannerella forsythia*, and *Treponema denticola* (collectively known as the "red complex"), were implicated as principal pathogens in the periodontium, contemporary research suggests that no single microorganism is solely responsible for disease onset. Instead, the entire dysbiotic microbial community acts as a pathogenic unit, wherein specific keystone pathogens modulate the local environment to favor the growth of more pro-inflammatory species [Figure 2.2] [6].

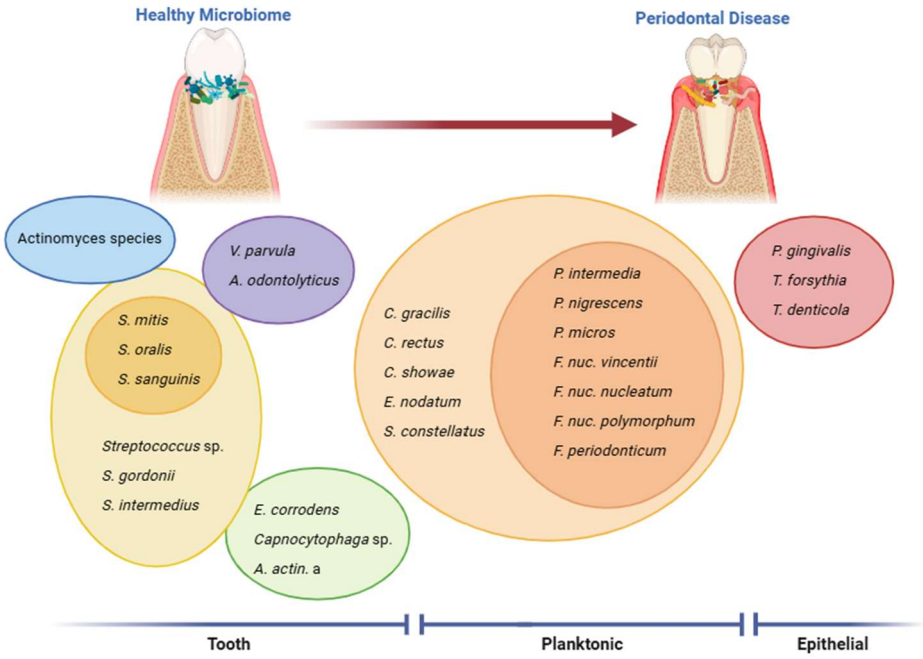

Figure 2.2 – Socransky's complexes of bacteria in the periodontium, from healthy to disease. Image created with BioRender, based on [6].

Current therapeutic protocols focus on mechanical debridement to eliminate subgingival plaque, systemic or local antibiotic administration, and surgical interventions to remove damaged tissues [7]. While antibiotics offer a convenient and non-invasive treatment option, their long-term use can lead to undesirable side effects, including the disruption of the gut microbiome and the emergence of antibiotic-resistant bacteria. Localized antibiotic delivery systems, although more targeted, face challenges such as limited retention time within the periodontal pocket due to the dynamic oral environment [4]. Furthermore, both systemic and localized approaches fail to adequately address the hypoxic microenvironment characteristic of periodontal pockets, a factor that exacerbates bacterial resistance and compromises the efficacy of treatments [8].

Given these limitations, the focus of contemporary research has progressively shifted from mere infection control to promoting periodontal regeneration. Regenerative periodontal therapy aims to restore the structure and function of the periodontium by stimulating new bone formation and reattachment of periodontal ligament cells. Various strategies have been explored in the literature, including the use of growth factors, stem cell therapies, and bioactive scaffolds that mimic the extracellular matrix, providing a conducive environment for cell proliferation and differentiation.

For these reasons, there is a growing interest in developing biomaterial-based therapeutic systems capable of localized, sustained, and controlled agent delivery. Among these, functionalized hydrogels stand out due to their exceptional biocompatibility, biodegradability, and versatility in encapsulating and delivering NPs and therapeutic agents, and for this reason, will be the subject of study in this thesis.

Chapter 3
Production of NPs for osteoinductive applications in periodontal treatment

Abstract

This work reports the synthesis, physicochemical characterization, and preliminary biological assessment of Ca-based NPs engineered as bioactive additives for hydrogel scaffolds intended for periodontal tissue regeneration. Particles were synthesized by controlled hydrothermal crystallization. SEM/TEM confirmed distinct morphologies, with HAp displaying a nanorod hedgehog architecture, Fe-*β*-TCP forming compact spherical nanoaggregates, and $CaCO_3$ yielding micrometric calcite crystals surrounded with nanospherical particulates. XRD validated the crystalline phases, while ATR-FTIR spectroscopy revealed characteristic phosphate and carbonate vibrational bands, as well as reduced hydroxylation in Fe-*β*-TCP due to Fe substitution. Zeta potential analysis demonstrated pH-responsive surface charge behavior, with Fe-*β*-TCP exhibiting an acidic shift in the isoelectric point and enhanced colloidal stability. BET analysis indicated porosity in Fe-*β*-TCP and HAp particles, with surface areas of 24.79 $m^2 \cdot g^{-1}$ and 38.73 $m^2 \cdot g^{-1}$, respectively, while $CaCO_3$ showed a lower external surface area but larger interparticle pores. SQUID magnetometry and Mössbauer spectroscopy confirmed paramagnetism in Fe-*β*-TCP with evidence of a low-temperature ordered phase. Overall, these results validate the feasibility of developing Ca-based particles toward multifunctional behavior, establishing a foundation for their integration into 3D-printed hydrogel scaffolds for periodontal regeneration.

3.1. Literature review

Nanomedicine has emerged as a transformative field in biomedical science, offering novel strategies for the diagnosis, prevention, and treatment of various diseases through the manipulation of materials at the nanoscale. Among the most promising tools in this domain are functional NPs, which possess unique physicochemical properties, such as high surface area-to-volume ratio, tunable surface chemistry, and the capacity for targeted delivery, that render them highly effective in therapeutic applications [9]. In the context of periodontal diseases, particularly periodontitis, functional NPs have garnered increasing attention due to their potential to overcome the limitations of conventional therapies. Traditional treatments, including mechanical debridement and systemic antibiotics, often fail to eradicate the pathogenic microorganism biofilms and are limited in promoting tissue regeneration, opening the need for the study of more effective alternatives [10].

In this work, HAp, *β*-tricalcium phosphate (*β*-TCP), and $CaCO_3$ were developed for this study due to their well-established biocompatibility, biodegradability, and bioactivity [11]. HAp and *β*-TCP, as calcium phosphate (CaP)-based ceramic biomaterials, closely mimic the mineral phase of bone and are known for their excellent osteoinductive and osteoconductive properties [12]. As for $CaCO_3$ NPs, they provide a biocompatible carrier system with potential for both controlled drug delivery and bone tissue regeneration, as well as antibacterial properties [13]. The integration of these functional NPs thus presents a synergistic approach to periodontitis therapy, addressing both microbial infection and the regenerative requirements of debilitated periodontal tissues.

3.1.1. Calcium phosphate

CaP-based biomaterials have garnered broad interest in the field of functional particles for the treatment of multiple diseases due to their exceptional biocompatibility, osteoconductivity, and composition resemblance to the mineral phase of the natural human bone [14]. For these reasons, they have been extensively studied in literature for applications such as bone graft substitutes as scaffolds, and bioactive coatings or composites for improving the properties of other materials [15]. Nanoscale CaPs, in particular, demonstrate enhanced characteristics due to their high surface area [16]. Parallel to that, the reduced particle size also allows for the incorporation of these particles into inks for 3D printing and robocasting [17].

Table 3.1 presents the principal types of CaP compounds encountered in biomedical applications. These compounds differ significantly in their chemical composition, crystallographic structure, solubility, and calcium-to-phosphorus (Ca/P) molar ratios, which directly influence their physicochemical properties and biological performance [18].

Table 3.1 – The main types of CaP compounds, adapted from [16].

CaP Compound	Formula	Ca/P ratio	pH Stability
Monocalcium phosphate monohydrate	$Ca(H_2PO_4)_2 \cdot H_2O$	0.5	0.0–2.0
Monocalcium phosphate anhydrous	$Ca(H_2PO_4)_2$	0.5	2.0–5.5 (>80ºC)
Dicalcium phosphate dihydrate	$CaHPO_4 \cdot 2H_2O$	1.0	2.0–6.0
Dicalcium phosphate anhydrous	$CaHPO_4$	1.0	5.5–7.0
Octacalcium phosphate	$Ca_8H_2(PO_4)_6 \cdot 5H_2O$	1.33	5.0–7.0
α-Tricalcium phosphate	$Ca_3(PO_4)_2$	1.5	Unstable
β-Tricalcium phosphate	$Ca_3(PO_4)_2$	1.5	5.0–12.0
Amorphous calcium phosphate	$Ca_x(PO_4)_y \cdot nH_2O$ (1.2 ≤ x/y ≤ 2.2)	1.2-2.2	6.5–9.5
Calcium-deficient hydroxyapatite	$Ca_{10-x}(HPO_4)_x(PO_4)_{6-x}(OH)_{2-x}$	1.5-1.67	9.5–12.0
Hydroxyapatite	$Ca_{10}(PO_4)_6(OH)_2$	1.67	4.2–12.0

In this study, *β*-TCP and HAp were selected as the CaP biomaterials of interest due to their promising potential in treating periodontitis. HAp, with a Ca/P molar ratio of 1.67, is chemically similar to the mineral phase of human hard tissues and is well known for its excellent biocompatibility, bioactivity, and ability to promote osteoconduction. Its physicochemical stability under physiological conditions makes it particularly suitable for maintaining structural integrity in periodontal defects [19]. Conversely, *β*-TCP, with a Ca/P ratio of 1.5, exhibits greater solubility and resorbability, enabling its gradual replacement by newly formed bone. These characteristics make *β*-TCP especially attractive for promoting bone regeneration in dynamic biological environments such as the periodontal region [16]. The selection of these two CaP phases enables a comparative and synergistic evaluation of their performance in periodontal regeneration, aiming to understand how their structural differences influence the healing process. Their combined or complementary use may provide an effective strategy for developing functional hydrogels capable of supporting periodontal tissue repair and regeneration.

3.1.1.1. Hydroxyapatite

Hydroxyapatite [$Ca_{10}(PO_4)_6(OH)_2$] is one of the most common biomaterials in the bone, and it is widely recognized for its crystalline structure and chemical composition similar to natural bone tissue, represented in Figure 3.1, with a Ca/P of 1.67, which gives it excellent biocompatibility and the ability to promote integration within bone tissue [20]. Additionally, it is characterized by high biotolerance and controlled resorption in tissues [19].

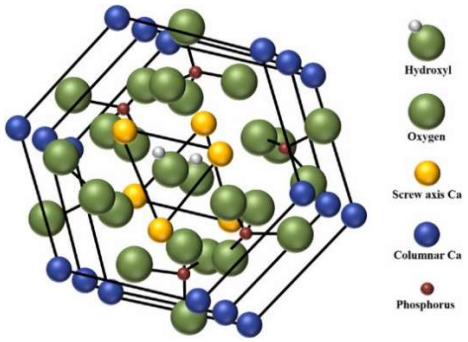

Figure 3.1 – Crystalline structure of HAp, retrieved from [20].

HAp particles have been utilized in various medical and dental applications, such as alveolar ridge reconstruction and bone-defect filling [21]. Moreover, its low solubility at physiological pH renders it ideal for localized drug delivery through surgical implantation or injection [22]. These attributes have made HAp a prominent material for addressing challenges in hard tissue engineering, particularly for bone regeneration. HAp NPs in particular have emerged as an alternative to conventional HAp due to their enhanced biocompatibility, biodegradability, and higher surface-to-volume ratio. These NPs can be functionalized to introduce hydrophobic interactions, optimize charge density, and elicit biological responses, making them more effective in interacting with the biological environment [10].

Those can be synthesized through various techniques, including wet chemical precipitation, sol-gel processing, hydrothermal synthesis, microwave-assisted methods, and ultrasonic techniques, as described in Table 1 of Appendix I. Among these, hydrothermal synthesis stands out as a cost-effective method for producing highly crystalline NPs [23]. This process often incorporates additives such as citric acid, a reducing and stabilizing agent. Citric acid, known for its chelating properties, plays a crucial role in controlling the size, shape, and stability of HAp NPs. At lower temperatures, citrate forms strong bonds with calcium ions, promoting particle aggregation, whereas at higher temperatures, these interactions weaken, resulting in increased negative surface charge and better particle dispersion [24].

Given its unique properties and versatile applications, HAp continues to be at the forefront of innovations in tissue engineering and regenerative medicine, as described in Table 2 of Appendix I. The introduction of composites for periodontal therapies marked a significant milestone in regenerative medicine. In 2005, the first composite designed explicitly for periodontal applications was developed, consisting of a three-layered structure that incorporates nano-carbonated HAp, collagen, and poly(lactic-co-glycolic acid). This innovative composite featured a smooth surface to inhibit unwanted cell adhesion on one side. In contrast, the opposite side was porous to promote cellular attachment, making it ideal for guided tissue regeneration [25].

In recent years, many studies on the use of HAp NPs for the treatment of periodontitis have proved their regenerative potential in periodontal therapy. For instance, Tamburaci *et al*., fabricated bilayer nanocomposite membranes incorporating silicon-doped HAp NPs. These membranes exhibited significant promise as biomaterials for guided bone regeneration in periodontal applications [26]. Similarly, Niu *et al*., developed bilayered scaffolds composed of polyamide-6, chitosan, and HAp NPs. These scaffolds demonstrated excellent bioactivity and osteoconductivity, making them effective for promoting bone regeneration [27].

Research by Baskar *et al*., revealed enhanced viability and odontogenic differentiation of dental pulp stem cells when exposed to HAp-carboxymethyl chitosan scaffolds [28]. Similarly, Bozoğlu *et al*., demonstrated that boron-doped HAp-coated PEEK implants significantly improved the adhesion and proliferation of periodontal ligament cells, further highlighting the compatibility of HAp NPs in periodontal applications [29].

Furthermore, the versatility of HAp NPs in tissue engineering has been exemplified by innovative scaffold designs. For example, Fang *et al*., employed gelatin-based scaffolds incorporating HAp NPs and metformin for alveolar bone regeneration in rat models, and these scaffolds produced superior results compared to conventional graft materials [30].

3.1.1.2. Iron-β-Tricalcium phosphate

β-TCP is a CaP ceramic with the chemical formula $Ca_3(PO_4)_2$, belonging to the

rhombohedral crystal system, specifically the space group R3c. Its unit cell comprises 21 formula units, accommodating three crystallographically distinct phosphate groups (PO_4^{3-}), each exhibiting slightly varied bond lengths and tetrahedral geometries [31]. These internal structural features influence the material's physicochemical properties. Compared to HAp, *β*-TCP lacks the OH^- group, which is reflected in the absence of corresponding vibrational peaks, enabling differentiation between the materials through spectroscopic methods [32].

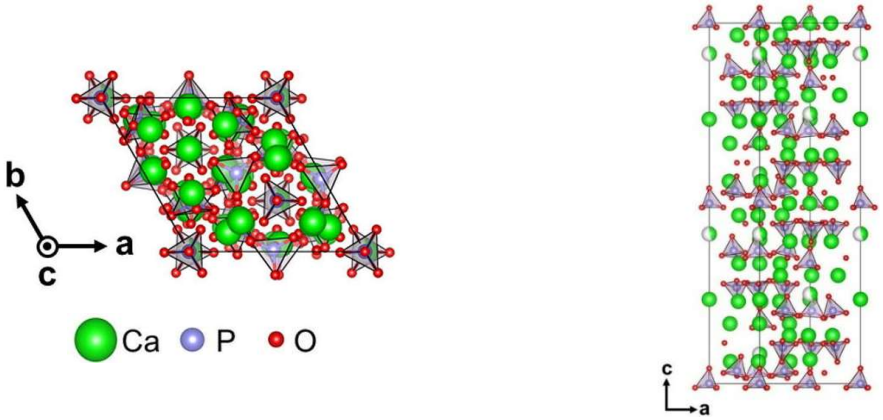

Figure 3.2 – Crystalline structure of *β*-TCP, retrieved from [33].

β-TCP is typically synthesized through high-temperature processes, including the thermal decomposition of Ca-deficient HAp, amorphous CaP, and solid-state reactions involving precursors such as DCPA and calcium oxide. The synthesis process generally involves heating the calcium phosphate precursors to temperatures above 650-750°C, which promotes phase transformation and decomposition required for *β*-TCP formation [34]. Solid-state reactions often require temperatures of 1000°C or higher to ensure complete conversion [35].

The synthesis of these NPs can be made through several techniques, including wet chemical precipitation, sol-gel processing, hydrothermal and solvothermal synthesis, mechanochemical methods, and microwave-assisted routes, as summarized in Table 3 of Appendix I. These methods allow the fine-tuning of *β*-TCP physicochemical characteristics, such as crystallinity, particle size, and porosity, which are critical parameters determining its biodegradability, ion release behavior, and osteoconductivity in biomedical and tissue engineering applications [36].

The incorporation of iron (Fe) into the *β*-TCP structure, resulting in Fe-*β*-TCP, alters its crystallographic and functional characteristics. Iron ions can substitute for calcium due to their comparable ionic radius, particularly in the trivalent form (Fe^{3+}), leading to modifications in lattice parameters and potentially promoting the stabilization of the *β*-phase. The presence of Fe in the crystal matrix influences the material's magnetic and electronic properties. Furthermore, Fe incorporation enhances the bioactivity and osteoinductive potential of *β*-TCP, as Fe is known to play a role in cellular metabolism and osteogenesis [37].

Fe-*β*-TCP has demonstrated the capacity to support apatite nucleation upon immersion in simulated body fluids (SBF), a phenomenon attributed to its favorable surface energy and ionic

exchange characteristics. In addition, the release of iron ions from the Fe-*β*-TCP matrix has been associated with antibacterial effects, likely due to interference with bacterial enzymatic systems and redox imbalance. These dual functionalities, osteogenic stimulation and antimicrobial activity, show the potential of Fe-*β*-TCP as a multifunctional biomaterial in the context of periodontitis therapy, where both bone regeneration and infection control are needed [38].

Due to its biocompatibility and resorbability, Fe-*β*-TCP has been explored not only as a constituent in bone cements but also as a dopant in hydrogel matrices and composite scaffolds designed for 3D printing. When combined with HAp, Fe-*β*-TCP contributes to the formation of biphasic CaP systems, offering a balance between structural stability and resorption rates suitable for tailored clinical applications [39]. Particularly in periodontitis applications, *β*-TCP is widely studied due to its capacity for promoting bone regeneration, biocompatibility, osteoconductivity, and resorbability. It can be applied as a grafting material for intrabony defects, socket preservation after tooth extraction, and periodontal regeneration, as *β*-TCP encourages new bone formation by acting as a biomaterial that gradually resorbs and is replaced by native bone tissue, making it suitable for reconstructing lost periodontal structures [40].

Recent studies have proved the efficacy of *β*-TCP as part of composite grafts (e.g., biphasic CaP, made of HAp and *β*-TCP) in treating periodontal defects in treating pocket depth reduction, clinical attachment level, and bone regeneration in periodontal intrabony defects [41]. Injectable *β*-TCP-loaded hydrogels, particularly those based on chitosan, have exhibited promise in tissue engineering for periodontitis by supporting cell delivery and offering an adaptable scaffold for defect filling and regeneration [42]. This versatility extends to the development of *β*-TCP-based membranes, which have shown superior clinical attachment gains over traditional barriers, largely due to the sustained release of Ca ions that stimulate cell differentiation and bone growth. When combined with stem cells or other bioactive agents, *β*-TCP scaffolds have shown further potential to enhance periodontal bone and soft tissue repair, proving their expanding role in advanced regenerative periodontal procedures [43].

3.1.2. Calcium carbonate

$CaCO_3$ is one of the most common naturally occurring compounds, holding significant importance across various scientific, industrial, and environmental fields. Found extensively in the Earth's crust, it is the principal constituent of sedimentary rocks such as limestone, marble, and chalk. Chemically, $CaCO_3$ is a white, odorless powder or crystalline substance that is sparingly soluble in water but reacts readily with acids, releasing carbon dioxide gas in the process [44].

The synthesis can occur through several distinct methods, each offering specific advantages in controlling particle size, morphology, and crystallinity [45]. As illustrated in Figure 3.3, the precipitation method (a) involves the reaction between carbonate (CO_3^{2-}) and calcium (Ca^{2+}) ions in the presence of additives, followed by filtration and separation to obtain the $CaCO_3$ NPs. The CO_2 bubbling method (b), also known as carbonation, utilizes gaseous carbon dioxide bubbled

through a Ca-containing solution, promoting the gradual formation of $CaCO_3$ under controlled conditions. The emulsion method (c) employs a water-in-oil (W/O) emulsion system stabilized by surfactants such as Tween 20 or Tween 80, enabling the synthesis of uniformly dispersed NPs through microreactor environments. Finally, the ball milling method (d) is a mechanical approach that generates $CaCO_3$ NPs by applying centrifugal and shear forces to reactant powders within rotating milling vials. Collectively, these techniques allow the fine-tuning of $CaCO_3$ NPs characteristics for diverse biomedical and industrial applications.

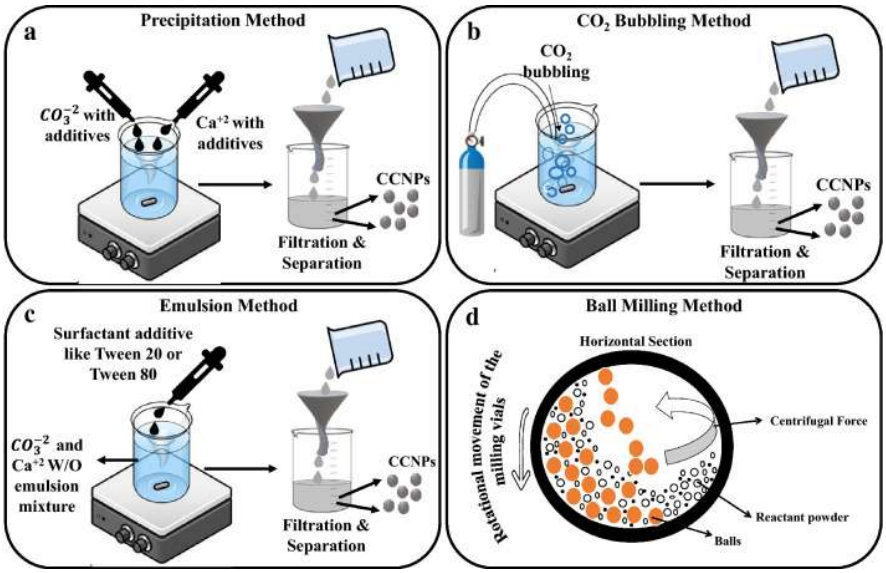

Figure 3.3 – Methods for the synthesis of $CaCO_3$ NPs: a) Precipitation, b) CO_2 bubbling (carbonation), c) Emulsion (W/O), and d) Mechanical (ball milling), retrieved from [45].

The precipitation method is one of the simplest and most widely used approaches, offering good control over particle size and morphology through adjustment of parameters such as pH, temperature, and the presence of additives. It typically produces NPs with high purity and tunable polymorphs; however, agglomeration can occur if stabilization agents are not adequately used [46]. CO_2 bubbling (carbonation) method also uses a calcium precursor to generate $CaCO_3$ NPs under relatively mild conditions and with excellent control over crystallinity and polymorphism due to the gradual diffusion of CO_2 gas. This technique often yields uniform and spherical particles while being environmentally friendly and energy-efficient. Its main limitation is the slower reaction rate compared to direct precipitation [47].

As for emulsion, it allows precise control of NP size and distribution through microemulsion droplets that act as confined reaction sites. This method can produce monodisperse NPs with narrow size distributions and high surface area. Nonetheless, it often involves complex preparation and the use of organic solvents or surfactants [48]. In contrast, the ball milling method is a solvent-free, scalable approach that relies on mechanical forces to induce solid-state reactions. It is particularly advantageous for large-scale synthesis for producing nanostructured

powders with high defect density. However, this method often results in less uniform particle shapes, broader size distributions, and possible contamination from the milling media [49].

Through all the methods, the crystallization behavior of $CaCO_3$ is highly sensitive to environmental parameters, such as temperature, pH, and pressure, each of which significantly influences the resulting polymorphic phase. Studies by Weiss *et al.* have demonstrated that vaterite tends to be the dominant phase at both ambient (25 °C) and elevated temperatures (80 °C). In comparison, an intermediate temperature near 50 °C favors the formation of calcite, and only minimal amounts of aragonite (below 5%) are typically detected at around 70 °C [50].

Table 3.2 –Typical morphologies of $CaCO_3$ particles. A) Morphology; B) Average Diameter; C) Structure. Adapted from [51].

	Calcite	**Aragonite**	**Vaterite**	
A	Cubic	Rod	Sphere	Flower
	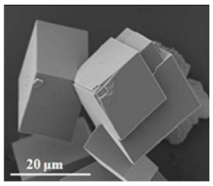	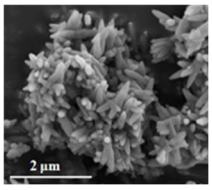	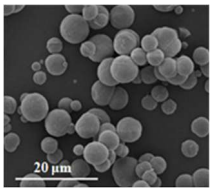	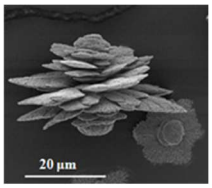
B	2-20µm	2-3µm	0.2-5µm	20-100µm
C	Rhomboedric	Orthorhombic	Hexagonal	

Morphologically, in the precipitation method, vaterite forms as spherical crystallites, especially abundant and smallest (1-2 µm) at 25 °C, with increasing size up to 10 µm at 30-40 °C. At 40 °C, calcite began to emerge, and by 50 °C, it became the dominant phase with rhombohedral crystals around 1-2 µm, while vaterite nearly disappeared. At 60 °C, calcite decreased and vaterite reappeared in smaller quantities. By 70 °C, large vaterite crystals were predominant, accompanied by traces of calcite and needle-shaped aragonite. At 80 °C, only vaterite and calcite remained, with aragonite absent [Figure 3.4] [50].

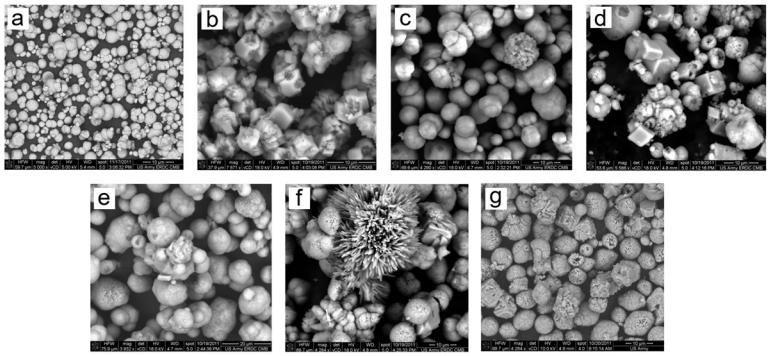

Figure 3.4 – SEM images of $CaCO_3$ crystals precipitated at (a) 25 °C, (b) 30 °C, (c) 40 °C, (d) 50 °C, (e) 60 °C, (f) 70 °C, and (g) 80 °C, retrieved from [50].

The pH of the reaction medium also plays a critical role in determining the phase and morphology of $CaCO_3$ crystals. When the gas diffusion method is employed for precipitation, acidic conditions (pH ≈ 0.5) result in a mixture of calcite and aragonite. As the pH increases beyond 5.5, calcite becomes the predominant phase, exhibiting a range of particle sizes and morphologies [Figure 3.5] [52]. Alkaline environments are generally considered to promote calcite nucleation and growth. Several works have confirmed that increasing pH values correlate with enhanced calcite formation [53]. Additionally, reduced supersaturation levels under acidic conditions have been associated with improved control over crystal shape, as well as prolonged induction times for nucleation events [54].

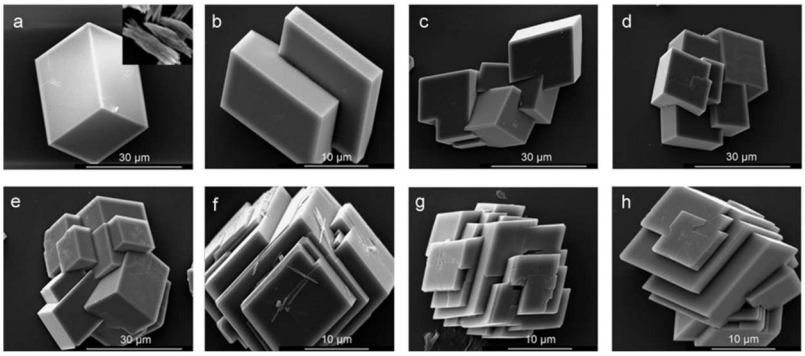

Figure 3.5 – SEM images of $CaCO_3$ precipitated in the solutions at different pH values: (a) 5.5, (b) 6.0, (c) 6.5, (d) 7.0, (e) 7.5, (f) 8.0, (g) 8.5, and (h) 9.0, retrieved from [52].

$CaCO_3$, particularly in NP form, exhibits favorable biocompatibility and osteoconductive properties that make it suitable for use in periodontal tissue regeneration. Studies have demonstrated that $CaCO_3$-based materials can provide structural scaffolding in periodontal defects, facilitating the infiltration and growth of new bone tissue. When combined with guided tissue regeneration techniques, these particles contribute to enhanced bone formation, although their osteoconductive effect in isolation is relatively limited [55].

In addition to its regenerative properties, $CaCO_3$ has been explored as a vehicle for targeted drug delivery in periodontal therapy. By enabling controlled release of anti-inflammatory or antimicrobial agents directly to affected tissues, these particles can enhance local therapeutic efficacy while minimizing systemic exposure [56]. This dual function, simultaneously serving as a scaffold for tissue regeneration and a carrier for pharmacological agents, represents a promising strategy for comprehensive periodontal management. Furthermore, $CaCO_3$-based formulations have demonstrated efficacy in remineralizing enamel, which supports the recovery of oral surfaces compromised during the progression or treatment of periodontitis [57].

$CaCO_3$ also presents benefits in patient comfort and post-treatment outcomes. When combined with compounds such as arginine, it has been shown to reduce dentine hypersensitivity, a common side effect of periodontal therapy [57]. Its low cytotoxicity and favorable tissue compatibility further reinforce its suitability for clinical application, particularly in minimally invasive

interventions aimed at promoting periodontal regeneration, representing a multifunctional biomaterial with significant potential in the treatment of periodontitis.

3.2. Materials and Methods

3.2.1. Materials

For the CaP NPs, Citric acid monohydrate ($C_6H_8O_7 \cdot H_2O$, 99%) was purchased from Panreac AppliChem (Germany). Ammonium hydroxide solution (NH_4OH, 25%) was purchased from Honeywell Fluka (USA). Iron(III) nitrate tetrahydrate ($Fe(NO_3)_3 \cdot 4H_2O$, 98%) was obtained from Thermo Scientific (USA). Calcium nitrate tetrahydrate (($Ca(NO_3)_2 \cdot 4H_2O$, 99%) was purchased from Riedel-deHaën (Germany). Ammonium hydrogen phosphate (($(NH_4)_2HPO_4$, 99.5–102.0%) was also obtained from Panreac AppliChem (Germany).

As for the $CaCO_3$ particles, $Ca(NO_3)_2 \cdot 4H_2O$ used was the same as previously. Hydrogen peroxide (H_2O_2, 35%) and sodium hydroxide (NaOH, 98%) were purchased from LABCHEM (Portugal) and Labkem (Spain), respectively.

3.2.2. Production of Hydroxyapatite particles

HAp NPs were synthesised via a hydrothermal precipitation method using $Ca(NO_3)_2 \cdot 4H_2O$ as the calcium salt source, as illustrated in Figure 3.6. Initially, a 0.6 M aqueous solution of citric acid was prepared under continuous stirring at 300rpm. Subsequently, NH_4OH (25% w/v) was added dropwise to the solution until the pH turned 8.5. After the solution reached 25ºC, $Ca(NO_3)_2 \cdot 4H_2O$ was added to the solution to a concentration of 0.2M. Then, a 0.2M $(NH_4)_2HPO_4$ solution was stirred into the initial solution.

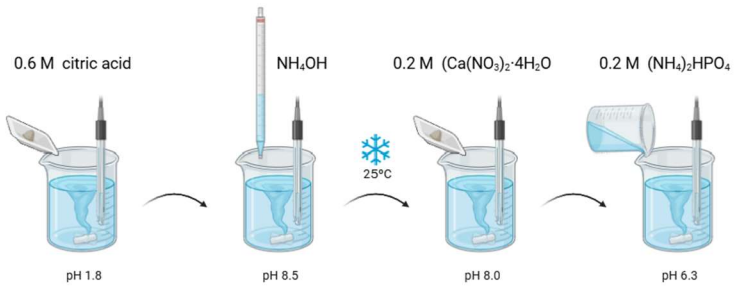

Figure 3.6 – Synthesis of HAp particles.

The resulting reaction mixture was then transferred into Teflon-lined stainless-steel autoclaves, sealed, and placed in an oven [ARGO LAB, TCN 30] preheated to 180 °C, where the hydrothermal synthesis was allowed to proceed for 24 hours. The precipitated NPs were recovered by centrifugation [Phoenix Instruments, CD2012 Plus] at 15,000 rpm for 3 minutes.

The solid product was washed three times with H_2O and dried at 40 °C. Finally, the dried material was ground using an agate mortar and pestle to obtain a homogeneous fine powder.

3.2.3. Production of Iron-β-Tricalcium phosphate particles

Fe-*β*-TCP NPs were synthesised via a hydrothermal precipitation method, depicted in Figure 3.7, using $Ca(NO_3)_2{\cdot}4H_2O$ as the calcium salt source and $Fe(NO_3)_3{\cdot}4H_2O$ as the iron salt source. Initially, a 0.6 M aqueous solution of citric acid was prepared. Subsequently, NH_4OH (25% w/v) was added dropwise to the solution until the pH reached 8.5. Following this, $Ca(NO_3)_2{\cdot}4H_2O$ and $Fe(NO_3)_2{\cdot}4H_2O$ were added to the solution to a concentration of 0.15M and 0.05M, respectively. Then, a 0.2M $(NH_4)_2HPO_4$ solution was stirred into the initial solution.

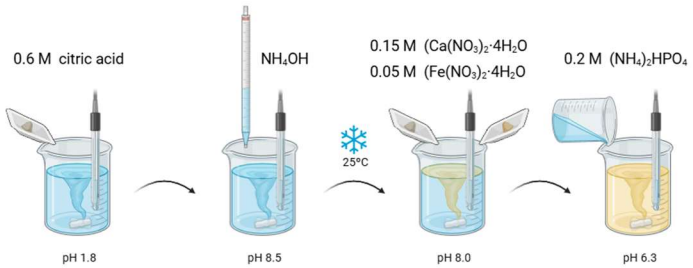

Figure 3.7 – Synthesis of Fe-*β*-TCP particles.

The resulting reaction mixture was subsequently subjected to the same processing and treatment conditions as those employed for the synthesis of the HAp NPs.

3.2.4. Production of Calcium carbonate particles

$CaCO_3$ particles were synthesised via a hydrothermal precipitation method using $Ca(NO_3)_2{\cdot}4H_2O$ as the calcium salt source. Initially, a 0.2 M aqueous solution of $Ca(NO_3)_2{\cdot}4H_2O$ was prepared under continuous stirring at 300rpm in a controlled temperature bath of 10 °C. The resulting solution was subjected to ultrasonic treatment for 5 minutes in an ultrasonic bath [ARGO LAB, AU-32]. Subsequently, 20 mL of H_2O_2 (30% w/v) was added dropwise to the solution. Following the complete addition of H_2O_2, the pH of the solution was adjusted to 10 through the controlled addition of a 1 M NaOH solution. This solution was left stirring in the ice bath for 2 hours, as illustrated in Figure 3.8.

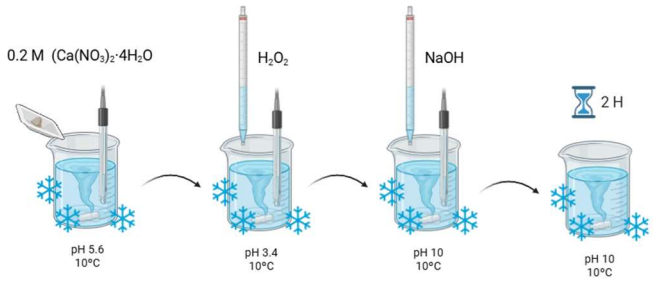

Figure 3.8 – Synthesis of Calcium carbonate particles.

The resulting reaction mixture was subsequently subjected to the same processing and treatment conditions as those employed for the synthesis of the HAp NPs.

3.2.5. Particle characterization

This section describes the methodologies employed to comprehensively characterize the synthesized particles in terms of their morphological, structural, physicochemical, magnetic, and biological properties, assessing their potential for periodontal applications.

3.2.5.1. Scanning Electron Microscopy

SEM analyses were performed using the Phenom XL Desktop SEM system (Thermo Fisher Scientific, USA), operated at 5 kV, purchased through Aero.Next PRR project.

3.2.5.2. Energy Dispersive Spectroscopy

EDS analyses were also performed using the Phenom XL Desktop SEM system (Thermo Fisher Scientific, USA), in the same conditions.

3.2.5.3. Transmission Electron Microscopy

Particles were observed by Transmission Electron Microscope (TEM) for the evaluation of morphology and size. Prior to TEM analysis, particles were ultrasonically dispersed in ethanol and deposited onto carbon-coated copper grids. Samples were photo documented by JEOL JEM 1400 TEM (JEOL, Japan).

3.2.5.4. X-Ray Diffraction

In this study, XRD was employed to confirm the crystalline phases present in the fabricated particles and to evaluate their degree of crystallinity. XRD measurements were performed using a LYNXEYE XE (Bruker, Germany) diffractometer operating with Cu Kα radiation (λ = 1.5418 Å). The obtained diffractograms were analyzed using the QualX software, and phase identification was performed by comparing them with reference patterns from the COD database [58]. The X-ray measurements were performed through a collaborative protocol between IPS and CQE/Instituto Superior Tecnico.

3.2.5.5. ATR-FTIR spectroscopy

Attenuated Total Reflectance Fourier Transform Infrared (ATR-FTIR) spectroscopy was employed to identify the characteristic vibrational bands associated with specific chemical bonds,

thereby confirming the incorporation of functional groups and potential interactions between components in composite systems. The measurements were carried out using a Nicolet 5700 FT-IR [Thermo Electron Corporation, USA] equipped with a diamond crystal, operating in the range of 4000–400 cm^{-1} with a spectral resolution of 4 cm^{-1}. All spectra were collected at room temperature, after the measurement of the vibrations in the environment. The ATR-FTIR measurements were performed through a collaborative protocol between IPS and CQE/Instituto Superior Tecnico.

3.2.5.6. Zeta Potential

Zeta potential measurements were conducted to evaluate the surface charge and colloidal stability of the synthesized particles in aqueous suspension. Measurements were performed using the equipment ZetaSizer Pro (Malvern Panalytical, UK). Samples were dispersed in 1 mM KCl at a fixed concentration of 1 mg/mL and sonicated before analysis. To construct the isoelectric curve, the pH of the suspensions was systematically adjusted over a range from 4 to 11 using 1 mM HCl and 1 mM NaOH. Equipment was obtained from PRR SONDA 2026.

3.2.5.7. SQUID Magnometry

Superconducting quantum interference device (SQUID) magnetometry was employed to characterize the magnetic properties of Fe-*β*-TCP. To assess the magnetic properties of the sample Fe-*β*-TCP, a S700X SQUID magnetometer (Cryogenic Ltd., UK) was used. Zero-field cooling and field cooling cycles were performed at various magnetic fields between 10 K and 300 K. The magnetic field dependence of the magnetization was also obtained at different temperatures (10 K, 50 K, 210 K, and 300 K) within a -5 T to 5 T range.

3.2.5.8. Mössbauer spectroscopy

Mössbauer spectroscopy was employed to investigate the local chemical environment, valence state, and magnetic ordering of iron in the Fe-*β*-TCP sample. The sample was collected between room temperature and 4 K in transmission mode using a conventional constant acceleration spectrometer and a 25-mCi 57Co source in Rh matrix. The velocity scale was calibrated using a Fe foil at room temperature. Low-temperature measurements were performed with the sample in liquid He (4 K) or He exchange gas (100 K) in a Janis bath cryostat, model SVT-400. The spectra were fitted to Lorentzian lines using a non-linear least-squares method. Relative areas and line widths of peak pairs 1-6, 2-5, and 3-4 in the magnetic sextets were constrained to remain equal during the refinement procedure.

3.2.5.9. BET surface area analysis

The Brunauer–Emmett–Teller (BET) method was used to determine the specific surface area of the samples through nitrogen adsorption–desorption isotherms. The measurements were carried out using a Sync 400 [3P Instruments, Germany] at liquid nitrogen temperature (-196,15 °C). Prior to analysis, the samples were degassed under vacuum at 120 °C for 3 hours to remove physisorbed contaminants and moisture. The BET surface area was calculated from the linear region of the adsorption isotherm according to the BET equation. Equipment was obtained from PRR SONDA 2026.

3.2.5.10. Antibacterial assay

The antibacterial activity of the NPs was evaluated against Staphylococcus aureus ATCC 25923 (Gram-positive) and Escherichia coli ATCC 25922 (Gram-negative). Minimum Inhibitory Concentration (MIC) and Minimum Bactericidal Concentration (MBC) values were determined according to the Clinical and Laboratory Standards Institute (CLSI) guidelines. Serial two-fold dilutions of each NP, ranging from 1600 to 1 µg/mL, were prepared in Mueller-Hinton (MH) broth in 96-well microplates. Bacterial suspensions were adjusted to 106 colony-forming units (CFU)/mL and added to the wells, followed by incubation at 37 °C for 24 hours. The MIC was defined as the lowest NP concentration that inhibited visible bacterial growth. To determine the MBC and eliminate false-positive readings due to NP-induced turbidity, aliquots from each well were plated on MH agar. Plates were incubated for 24 hours at 37 °C. The MBC was defined as the lowest concentration at which no bacterial colony growth was observed.

3.2.5.11. Cytocompatibility assay

Cell culture and particle exposure were conducted according to the procedures described in Appendix II.

3.3. Results and discussion

3.3.1. Calcium phosphate particles

The crystalline structure of the HAp and Fe-*β*-TCP NPs is presented in Figure 3.9. It can be observed that the two NPs exhibit very distinct crystalline features, consistent with the respective lattice symmetries of HAp and *β*-TCP, as referenced by the Joint Committee on Powder Diffraction Standards (JCPDS) files [58].

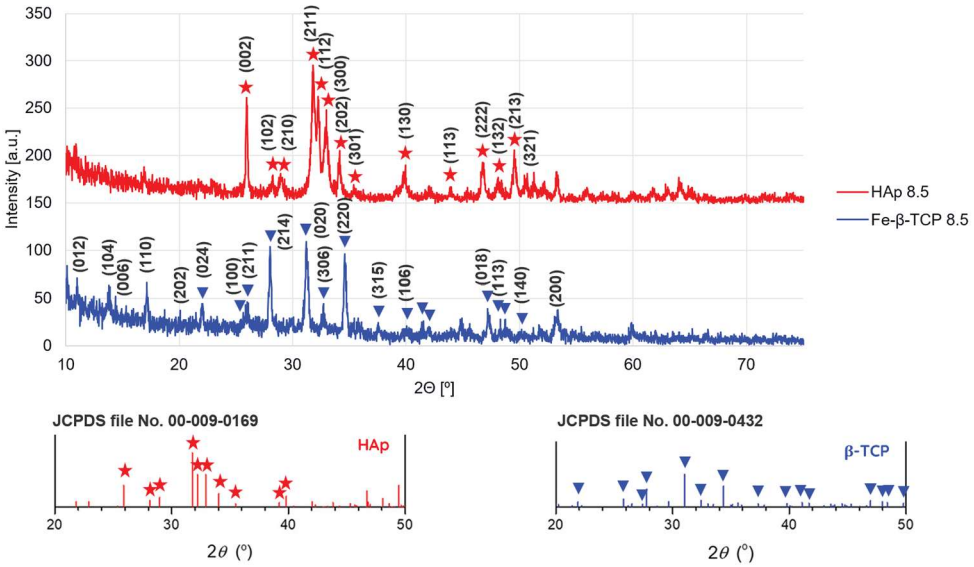

Figure 3.9 – XRD of HAp and Fe-*β*-TCP particles, compared with the JCPDS standards [58].

The HAp spectra exhibit a first peak at 25.9º corresponding to (002) and an interplanar spacing of $d_{(002)}$=3.44 Å, followed by three prominent peaks within the 2θ range of 31° to 33° at 31.7°, 32.2°, and 32.9°, corresponding to the (211), (112), and (300) crystallographic planes of a hexagonal $P6_3/m$ structure. These peaks exhibit a narrow full-width at half maximum, indicative of high crystallinity. The corresponding interplanar spacings are calculated as $d_{(211)}$= 2.814 Å, $d_{(112)}$= 2.778 Å, and $d_{(300)}$ = 2.720 Å, matching the standard HAp reference pattern JCPDS 00-009-0169 [58]. Additional peaks at 2θ ≈ 25.8° ($d_{(002)}$ ≈ 3.45 Å), 34.1° ($d_{(310)}$ ≈ 2.63 Å), 46.9° ($d_{(222)}$ ≈ 1.94 Å), and 49.4° ($d_{(213)}$ ≈ 1.84 Å) further corroborate a well-crystallized HAp phase free from secondary by-products [58].

The XRD of Fe-*β*-TCP [Figure 3.9] displays the characteristic peaks of *β*-TCP in the $R\bar{3}c$ trigonal space group [58]. Major diffraction peaks are observed 2θ ≈ 27.8° (d(214) ≈ 3.21 Å), 2θ ≈ 34.4° (d(300) ≈ 2.60 Å), and 2θ ≈ 35.8° (d(306) ≈ 2.51 Å) [58]. Reflections at higher angles, notably at 2θ ≈ 47.1° (d(140) ≈ 1.93 Å), 48.4° (d(220) ≈ 1.87 Å), and 49.8° (d(113) ≈ 1.83 Å), further confirm the *β*-TCP phase.They could also be an indicator of the presence of microstrain, likely due to the substitution of smaller Fe^{3+} ions (ionic radius ~ 0.64 Å) for Ca^{2+} (0.99 Å) in the TCP lattice [59]. The absence of α-TCP reflections justifies that iron incorporation effectively stabilizes the *β* polymorph under the applied synthesis conditions [31].

In the ATR-FTIR spectra of Figure 3.10, it is also possible to verify the structural differences between the produced HAp and Fe-*β*-TCP. Both spectra exhibit the characteristic bands attributable to phosphate species (PO_4^{3-}), which dominate the fingerprint region. In the Fe-*β*-TCP, the asymmetric stretching vibration $v_3(PO_4^{3-})$ appears prominently around 1110–1000 cm^{-1}, while the symmetric stretching $v_1(PO_4^{3-})$ is observed near 960 cm^{-1} [60]. Additional bending mode v_2 of PO_4^{3-} is identified at approximately 570 cm^{-1} [61]. HAp spectrum also displays strong phosphate vibrations, but it is distinguished by the presence of a pronounced band at around 875

cm^{-1}, assigned to the HPO_4^{2-} group, indicating the presence of partially protonated phosphate species. Furthermore, the HAp spectrum reveals small absorption bands at approximately 630 cm^{-1} and 3570 cm^{-1}, which correspond to the bending and stretching vibrations of structural hydroxyl (O–H) groups, respectively [61]. These features are typical of stoichiometric HAp and are notably weaker or absent in the Fe-*β*-TCP NPs, indicating a reduced hydroxyl content [62].

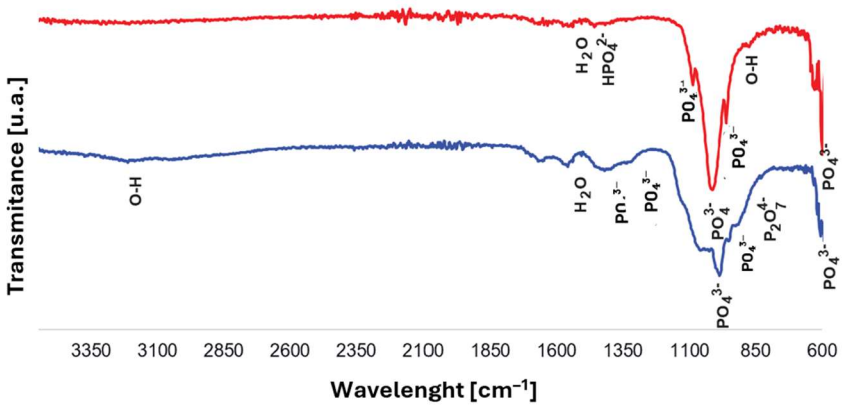

Figure 3.10 – ATR-FTIR spectra of developed HAp and Fe-*β*-TCP NPs.

The weak bands detected between 1450 and 1400 cm^{-1} and near 870 cm^{-1} in both spectra are attributed to the bending and stretching vibrations of PO_4^{3-}, characteristic of CaP phases, and within their crystal lattices. The more intense bands in the Fe-*β*-TCP spectrum suggest a higher content of HPO_4^{2-} species or more ordered phosphate environments. This is consistent with the typical vibrational modes of phosphate groups, where v_3 and v_2 bands of PO_4^{3-} and HPO_4^{2-} appear within this spectral range [64]. In the Fe-*β*-TCP spectrum, an additional band near 725–740 cm^{-1} can be observed, which may correspond to the vibrational mode of pyrophosphate groups ($P_2O_7^{4-}$), indicating a deviation from the stoichiometric *β*-TCP structure and the possible formation of Fe-substituted secondary phosphate phases [65].

Following the successful identification of the developed NPs, their morphology was subsequently analyzed. SEM images [Figure 3.11 A] revealed that the HAp particles consist of agglomerated clusters composed of nanosized (in 2 dimensions), rod-like structures radiating outward, forming a “hedgehog” morphology. The EDS spectrum [Figure 3.11 B] confirmed the presence of 6.7% Ca, 4.1% P, 32.4% O, and 56.8% C. The Ca/P ratio was calculated to be approximately 1.63, which is within the range for Ca-deficient HAp, but close to the theoretical value of 1.67 for stoichiometric HAp. The relatively high carbon content can be attributed to the presence of organic components from citrate species used in the synthesis process. TEM analysis [Figure 3.11 C] corroborated the presence of rod-shaped agglomerates and provided dimensional measurements, indicating average particle widths of ~60 nm and lengths of ~170 nm, with certain particles exhibiting significantly greater lengths while maintaining a consistent width.

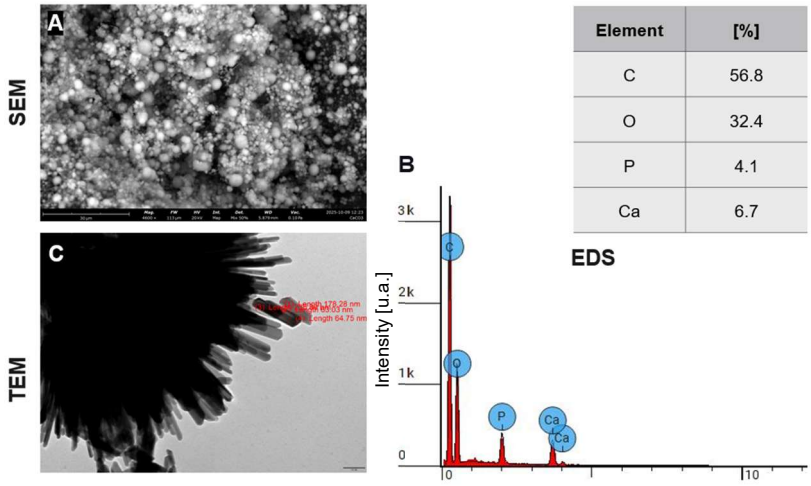

Element	[%]
C	56.8
O	32.4
P	4.1
Ca	6.7

Figure 3.11 – Morphological analysis of HAp particles in A) SEM, B) EDS, and C) TEM analysis.

Comparatively, SEM images of Fe-*β*-TCP revealed that the particles present a spherical-like morphology with a nanometric size, and some of them are agglomerated [Figure 3.12 A]. The EDS spectrum [Figure 3.12 B] confirmed the presence of 21.8% Ca, 15.4% P, 34.4% O, 9.9% Fe, and 8.0% C. The calculated Ca/P molar ratio of approximately 1.42 is close to the stoichiometric value for *β*-TCP (1.5), confirming the successful formation of the TCP phase. The presence of Fe peaks indicates effective incorporation within the structure. TEM analysis [Figure 3.12 C] confirmed the spherical morphology with particles from ~30 to ~50 nm in diameter on average.

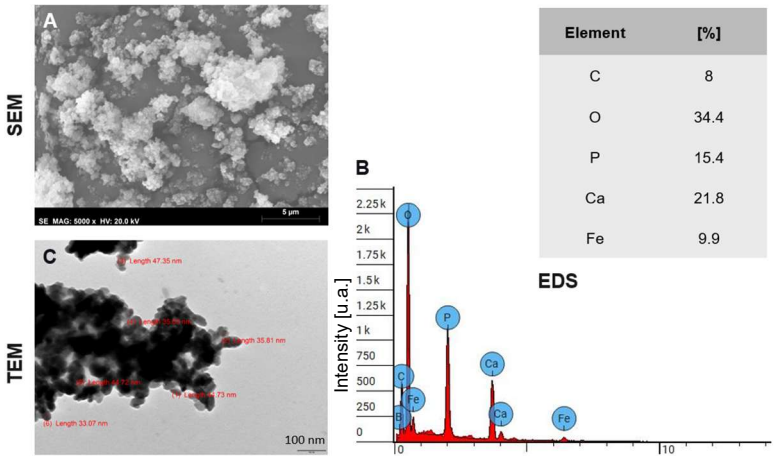

Element	[%]
C	8
O	34.4
P	15.4
Ca	21.8
Fe	9.9

Figure 3.12 – Morphological study of Fe-*β*-TCP particles in A) SEM, B) EDS, and C) TEM analysis.

The zeta potential measurements of HAp and Fe-*β*-TCP NPs as a function of pH of their suspension are presented in Figure 3.13. In the case of HAp, the zeta potential curve demonstrates a clear pH-dependent behavior, transitioning from positive to negative values as the pH increases. At low pH, the surface exhibits a positive zeta potential of approximately +10.5 mV, which gradually decreases with increasing pH. The isoelectric point (IEP) is observed near pH 6, where the IEP of HAp typically falls between pH 5.5 and 7.0, depending on factors such as morphology, synthesis, and ionic strength of the medium [66]. Above the IEP, the surface

becomes increasingly negatively charged, reaching approximately -38 mV at pH 12. This negative shift reflects the deprotonation of phosphate and hydroxyl surface groups, making the surface more electronegative under alkaline conditions [67].

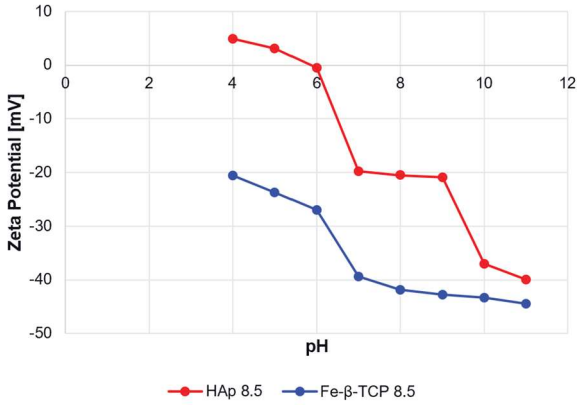

Figure 3.13 – Zeta Potential of experimental HAp and Fe-β-TCP particles.

Fe-*β*-TCP NPs exhibit a slightly different surface charge behavior. At pH 4, the zeta potential also begins to decrease with increasing pH [68]. As the pH increases, the zeta potential becomes increasingly negative, reaching values close to -45 mV at a pH of 12. This trend suggests a higher colloidal stability of Fe-*β*-TCP across the pH range [69].

The magnetic behavior of the Fe-*β*-TCP NPs was also investigated through temperature-dependent magnetization measurements under zero-field-cooled (ZFC) and field-cooled (FC) conditions, as well as through isothermal magnetization curves, M(B), at selected temperatures, by the SQUID magnometry analysis. The ZFC and FC magnetization curves measured under different applied magnetic fields are presented in Figure 3.14.

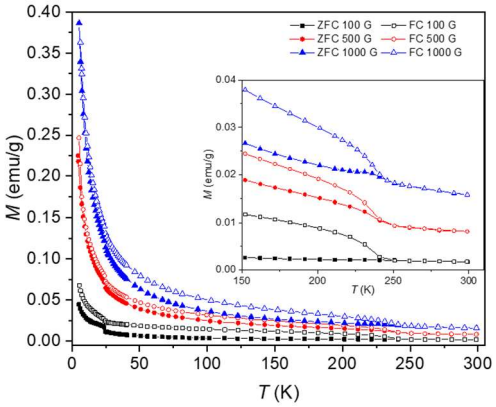

Figure 3.14 – Temperature dependence of ZFC and FC magnetization in several magnetic fields.

As expected for a paramagnetic material, the magnetization decreases with increasing temperature, typical of systems in which thermal fluctuations progressively overcome magnetic alignment, resulting in a reduced susceptibility [70]. A slight divergence between the ZFC and FC curves is observed below approximately 230 K, indicating a weak irreversibility at low temperatures. This suggests the onset of a magnetically ordered phase, which is most likely

responsible for the observed bifurcation. Above this temperature, the curves converge and overlap entirely, which is consistent with a transition to a paramagnetic state.

To further clarify the magnetic nature of the Fe-*β*-TCP NPs, magnetization as a function of M(B) was recorded at various temperatures [Figure 3.15]. M(B) curves exhibit a linear dependence on the applied field at all temperatures, consistent with paramagnetic behavior [71]. Notably, at 10 K, there is a deviation from linearity, displaying weak curvature at high magnetic fields. This is likely attributable to the enhanced alignment of magnetic moments at low temperatures and strong fields. No evidence of magnetization saturation was observed up to the maximum applied field of 5 T, further supporting the absence of ferromagnetic or superparamagnetic contributions.

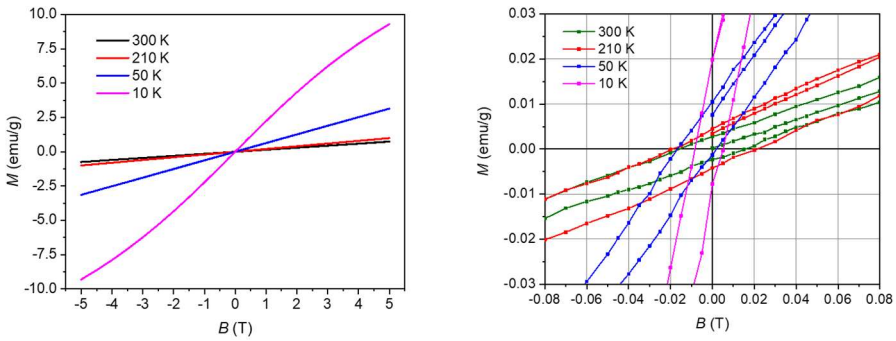

Figure 3.15 – Left: Magnetic field dependence of M(B). Right: Detail of M(B) data at small magnetic fields.

Examination of the low-field region shows small but clear hysteresis in all M(B) curves, with coercive fields of about 160 G, 200 G, 18 G, and 60 G at 300 K, 210 K, 50 K, and 10 K, respectively. The increase in coercivity around 210 K indicates the onset of local magnetic ordering or spin freezing below the transition temperature observed in the ZFC-FC data, suggesting that this behavior is intrinsic to the material. Since stoichiometric *β*-TCP is diamagnetic, the observed paramagnetism confirms the successful substitution of Fe ions into the *β*-TCP lattice, likely replacing Ca^{2+}. Nevertheless, the magnetic transition near 230 K and the presence of coercivity imply the coexistence of secondary magnetic phases, such as iron-rich phosphate or oxide inclusions formed during synthesis, which may not appear in the previously analyzed ART-FTIR bands as Fe-O bands typically occur in ~400-700 cm^{-1} and would therefore be masked or overlap with phosphate v_4/v_1 bands.

The Mössbauer spectra [Figure 3.16] are complex due to overlapping signals from multiple Fe species, revealing both high-spin Fe^{3+} (S = 5/2) and Fe^{2+} (S = 2) in different local environments [72], [73]. The data indicate that about 26% of Fe^{3+} and 35% of Fe^{2+} ions remain paramagnetic down to 4 K, while additional fractions of 17% Fe^{3+} and 22% Fe^{2+} exhibit magnetic hyperfine splitting at 100 K and 4 K, reflecting strong magnetic interactions. These findings confirm the coexistence of Fe^{3+} and Fe^{2+} ions and support the magnetic transition near 230 K observed in the SQUID measurements.

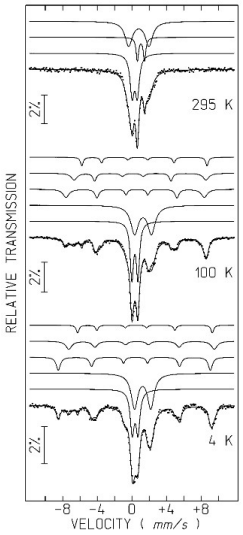

Figure 3.16 – Mössbauer spectra taken at different temperatures.

Table 3.3 – Estimated parameters from the Mössbauer spectra taken between 295 K and 4 K.

T	IS mm/s	ε mm/s	B_{hf} tesla	I	Fe oxidation state
295 K	0.44	0.60	-	41%	Fe^{3+}
	1.16	0.83	-	14%	Fe^{2+}
	0.92	2.33	-	45%	Fe^{2+}
100 K	0.46	0.70	-	29%	Fe^{3+}
	1.40	1.93	-	34%	Fe^{2+}
	0.48	-0.08	49.7	16%	Fe^{3+}
	0.98	0.23	47.2	14%	Fe^{2+}
	1.01	1.13	44.8	7%	Fe^{2+}
4 K	0.49	0.66	-	26%	Fe^{3+}
	1.36	1.88	-	35%	Fe^{2+}
	0.47	-0.14	54.4	17%	Fe^{3+}
	0.97	0.53	52.1	15%	Fe^{2+}
	1.10	1.05	48.2	7%	Fe^{2+}

Fe^{2+} that remain paramagnetic below 230 K, ~35% of the total Fe [Table 3.3], may be incorporated in the $Ca_3(PO_4)_2$ phase, replacing Ca on Ca-(5) sites and vacancies on Ca(4) sites. Fe^{3+} paramagnetic down to 4 K may also be substituting for Ca on Ca-(5) sites in $Ca_3(PO_4)_2$, forming vacancies on Ca-(4) sites, or may be present in an additional phase [72], [73]. Other phases containing Fe^{3+} and/or Fe^{2+} with strong magnetic correlations below 230 K are also present. No evidence of superparamagnetic behaviour was detected across the temperature range, confirming that the observed magnetic features arise from stable, long-range ordered interactions rather than thermally fluctuating nanometric domains [72], [73].

BET analysis was conducted on the Fe-*β*-TCP and HAp particles [Figure 3.17], and the resulting data show significant differences in BET adsorption curves, as well as surface area and pore characteristics, which can be correlated with the observed modifications in microstructure, crystal structure, morphology, and the presence of ion substitutions.

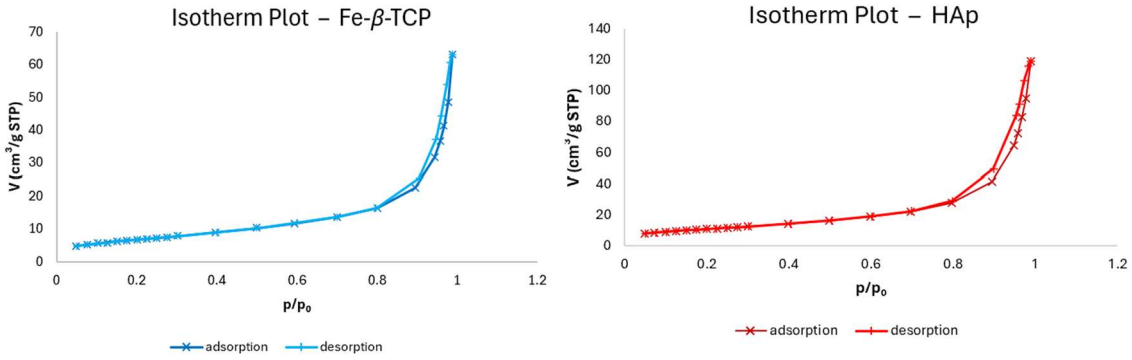

Figure 3.17 – BET isotherm plot of Fe-*β*-TCP and HAp particles.

Fe-*β*-TCP exhibited a BET surface area of 24.79 $m^2 \cdot g^{-1}$, with a total pore volume of 0.098 $cm^3 \cdot g^{-1}$ and an average pore diameter of 15.76 nm. The isotherm displayed a profile typical of

mesoporous materials, likely of Type IV according to IUPAC classification, with a small but distinct hysteresis loop at higher relative pressures ($p/p_0 > 0.8$), indicative of capillary condensation within mesopores, most likely of type H3 [74]. Such hysteresis loops are typically associated with slit-shaped pores or irregular mesoporous networks. The BET constant (C) is equivalent to 61.75, indicating relatively strong interactions between the nitrogen adsorbate and the Fe-*β*-TCP surface, possibly due to surface heterogeneity introduced by Fe incorporation. The presence of Fe^{3+} ions within the *β*-TCP lattice can modify local surface charge distribution and create defect sites, thereby increasing surface energy and enhancing the adsorption affinity for nitrogen molecules. The monolayer capacity (Vm = 5.70 $cm^3 \cdot g^{-1}$ STP) further supports the observation of an enlarged external surface compared to non-substituted TCP materials, which typically exhibit BET surface areas of 5-60 $m^2 \cdot g^{-1}$ [75].

In contrast, HAp presented a significantly higher BET surface area of 38.73 $m^2 \cdot g^{-1}$, with a total pore volume of 0.184 $cm^3 \cdot g^{-1}$ and an average pore diameter of 19.02 nm, reflecting a substantially more developed surface and a more open pore network than that of Fe-*β*-TCP. The nitrogen adsorption–desorption isotherm obtained for HAp exhibits a profile characteristic of a Type IV isotherm, consistent with the behaviour of mesoporous materials, showing a gradual increase in adsorption at intermediate relative pressures followed by a sharp rise at higher pressures ($p/p_0 > 0.8$) [76], [77]. The divergence between the adsorption and desorption branches reveals a pronounced hysteresis loop, likely of H3 type, commonly associated with slit-shaped pores or aggregated plate-like particles typical of CaP systems [76], [78], [79]. This hysteresis behaviour indicates mesoporosity arising from interconnected voids between the needle-like crystallites forming the HAp aggregates [79]. The high BET constant (C = 82) reinforces the reliability of the monolayer model and suggests strong adsorbate–surface interactions, while the elevated monolayer capacity (Vm = 8.90 $cm^3 \cdot g^{-1}$ STP) is consistent with the extensive accessible surface area of the particles [80].

The distinct difference in surface area between the two developed NPs can be attributed to their morphological characteristics. As mentioned before, the HAp particles developed exhibit a hedgehog-like morphology, composed of numerous needle-shaped nanocrystals radiating from a common center to form spherulitic aggregates. This structure results in an extremely high surface-to-volume ratio, where the individual nanoneedles expose extensive external surfaces and generate mesopores at their interstices. Such architecture enhances both the total surface area and pore volume, which explains the superior BET results obtained. The difference in average pore diameter between Fe-*β*-TCP (15.76 nm) and HAp (19.02 nm) further supports this interpretation. The slightly larger pores in HAp are consistent with the presence of inter-needle spaces and open voids, whereas the Fe-*β*-TCP pores likely originate from intergranular gaps within a more isotropic matrix or the Fe substitution may induce local densification during synthesis, resulting in smaller pore volumes and reduced surface accessibility [81].

When compared with literature, the BET surface area of the Fe-*β*-TCP falls lower than the

range of reported values for doped *β*-TCP materials, suggesting that the particular synthesis conditions, and specifically Fe-induced local densification or grain coalescence, inhibited the formation of accessible mesoporosity and surface exposure, nonetheless, the absence of detectable secondary phases in the XRD diffraction indicates that Fe substitution was accommodated within the *β*-TCP lattice without major crystallographic disruption, preserving the material's structural integrity [34]. In contrast, HAp surface area exceeds that of conventional HAp microparticles, a result that can be directly correlated with the nanoscale, needle-like morphology achieved under the employed synthesis conditions [81].

Following physicochemical characterization, the antimicrobial and cytocompatibility profiles of the obtained particles were investigated. Across all tested concentrations (1600 to 1 µg/mL), HAp and Fe-*β*-TCP NPs did not inhibit the growth of *S. aureus* or *E. coli*, as indicated by turbidity in broth cultures and colony formation on agar plates. Accordingly, no MIC or MBC values could be determined.

As illustrated in Figure 3.18, HAp particles were not cytotoxic within the tested concentration range. Metabolic activity was similar to the control. DNA content also revealed the absence of toxicity; indeed, MTT values of the treated cultures were higher (~30%, $p<0.5$) than those in the control. ALP activity was similar to that of the control.

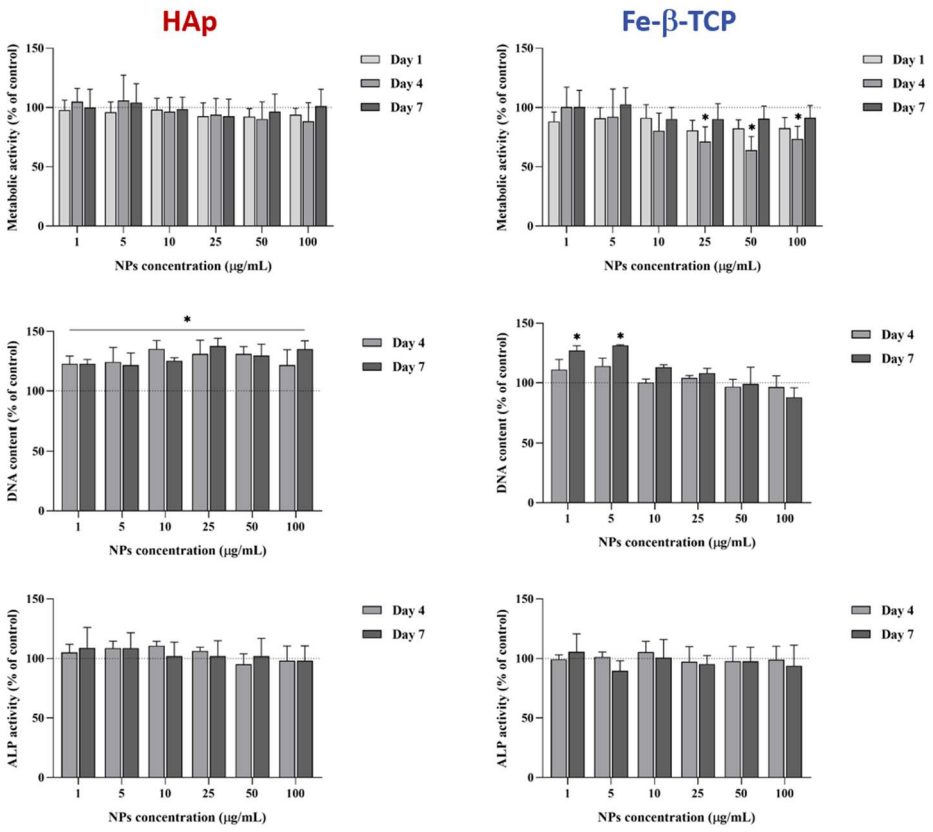

Figure 3.18 – Metabolic activity, DNA content, and ALP activity of MG63 cell cultures exposed to HAp and Fe-*β*-TCP particles (1 to 100 µg/mL) for 7 days. * Significantly different from control, set up at 100%.

Fe-*β*-TCP NPs revealed a slightly different biological response [Figure 3.18]. After 1 day of exposure, metabolic activity was similar to the control within the tested concentration range. However, values decreased slightly at day 4 of exposure for the higher concentrations (25, 50, and 100 μg/mL (~30%, $p<0.5$). Nevertheless, cells recovered, and values were similar to those of the control after 7-day exposure. Compared to the control, the DNA content of the cultures exposed to 1 and 5 μg/mL was higher after long exposure time (7 days, ~30%, $p<0.5$), but similar in the other conditions.

3.3.2. Calcium carbonate

The SEM images of $CaCO_3$ [Figure 3.19 A] revealed the presence of well-defined cubic microstructures with an average size of approximately 8 μm. These micrometric particles appeared as compact, faceted crystals with mostly smooth surfaces, indicative of a high degree of crystallinity. The cubic morphology is consistent with the calcite polymorph of $CaCO_3$ [44]. In addition to the micrometric cubic structures, finer spherical NPs could be observed dispersed on the surface and surroundings of the cubes. TEM analysis of these nanospheres [Figure 3.19 C] revealed particle sizes ranging from approximately 10 to 60 nm, with some even smaller. The coexistence of micrometric cubes and smaller nanosized particles suggests heterogeneous nucleation and growth during synthesis, potentially influenced by local variations in supersaturation and reaction kinetics.

The elemental composition of the sample was evaluated using EDS analysis [Figure 3.19 B]. The obtained spectrum exhibited strong peaks corresponding to 46.0% Ca, 51.7% O, and 2.3% C. This Ca/O ratio closely aligns with the theoretical stoichiometry of $CaCO_3$, confirming the chemical identity of the synthesized material [82]. The slightly lower C content could be attributed to surface effects or partial decomposition of carbonate species under the electron beam, leading to local degassing of CO_2 during analysis.

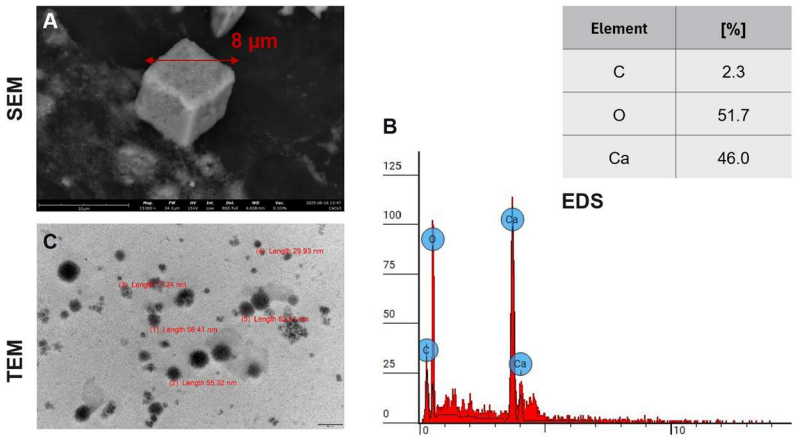

Figure 3.19 – Morphological analysis of $CaCO_3$ particles in A) SEM, B) EDS, and C) TEM analysis.

As shown in Figure 3.19, the crystalline structure of the synthesized $CaCO_3$ exhibits distinct and sharp diffraction peaks, indicating a high degree of crystallinity. All observed peaks

correspond well with the standard diffraction pattern of calcite-phase $CaCO_3$, as referenced by the JCPDS card No. 47-1743 [58].

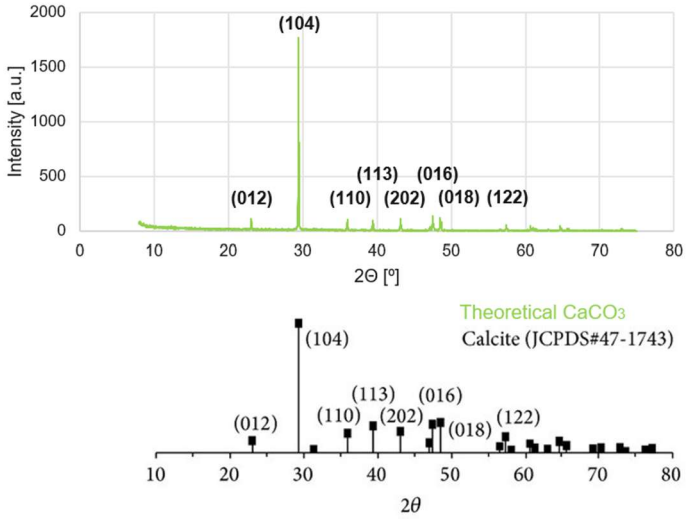

Figure 3.20 – X-Ray Diffraction of $CaCO_3$ NPs, compared with the JCPDS standard retrieved from [58].

The most intense diffraction peak is observed at approximately 2θ ≈ 29.4°, which corresponds to the (104) crystallographic plane, a characteristic reflection of the rhombohedral calcite structure. Other significant peaks appear at 2θ ≈ 23.1° (012), 2θ ≈ 35.9° (110), 2θ ≈ 39.4° (113), 2θ ≈ 43.2° (202), 2θ ≈ 47.5° (016), 2θ ≈ 48.5° (018), and 2θ ≈ 56.6° (122), all of which are consistent with the theoretical pattern of calcite $CaCO_3$ [83]. The good agreement in both position and relative intensity between the experimental and reference diffraction profiles strongly suggests the successful formation of pure calcite without polymorphic phases such as aragonite or vaterite [84]. The absence of peak broadening further supports the formation of well-ordered crystals with relatively large crystallite size, indicating favorable synthesis conditions [84].

The ATR-FTIR spectrum obtained for the $CaCO_3$ particles, present in Figure 3.21, reveals characteristic absorption bands of calcite [85].

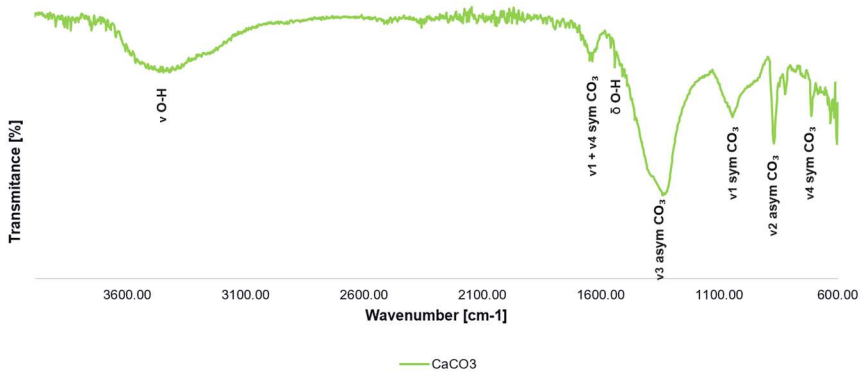

Figure 3.21 – ATR-FTIR spectra of developed $CaCO_3$ particles.

In this spectrum, a prominent absorption band is observed at 1425 cm^{-1}, corresponding to the asymmetric stretching vibration of the carbonate group (v_3). This vibrational mode is generally

the most intense in calcite spectra due to its substantial dipole moment change and is consistently reported in the 1415-1450 cm^{-1} range in literature [85]. The sharpness and intensity of this peak are indicative of well-ordered carbonate groups within a crystalline lattice. The out-of-plane bending mode (v_2) of the carbonate ion is evident at 875 cm^{-1}. This band is characteristic of rhombohedral carbonates and is commonly reported at a wavelength of 870-880 cm^{-1} [86], [87]. Its presence, along with the symmetric stretching mode (v_1) near 1080-1100 cm^{-1}, may reflect slight lattice distortions or defect sites that activate otherwise forbidden modes [85].

Another key peak appears near 712 cm^{-1}, which corresponds to the in-plane bending vibration (v_4) of the carbonate ion. This band is well known as the v_4 band of calcite, which occurs at slightly lower wavenumbers compared to that of aragonite or vaterite [88]. For calcite, this mode is typically found between 708 and 714 cm^{-1}, consistent with the position observed in the present analysis. The absence of additional bands in the 710-750 cm^{-1} region, which would be indicative of polymorphs such as vaterite, further corroborates the purity of the calcite phase [88].

A broad absorption centered around 3400 cm^{-1}, along with a smaller bending vibration near 1630 cm^{-1}, is attributed to O-H stretching vibrations, indicating the presence of adsorbed water or surface hydroxyl groups [85]. Combination and overtone bands are also visible in the regions around 1790 cm^{-1} and 2500 cm^{-1}. The band at approximately 1790 cm^{-1} is generally assigned to a combination of the v_1 and v_4 modes, whereas the broader feature near 2500 cm^{-1} corresponds to the $v_1 + v_3$ combination [86]. These features, although less intense, are consistent with the vibrational behavior of calcite and support the assignment of the characteristic modes.

The variation of the zeta potential as a function of pH is presented in Figure 3.22. The measurements reveal a unique surface behaviour, with a clear PZC and a progressive shift in surface charge across the examined pH range. This behaviour is not consistent with previous reports for calcite, as at higher pH levels (around 9), $CaCO_3$ typically exhibits a small positive zeta potential. As the pH decreases toward neutral (around 7), the zeta potential tends to increase in magnitude, often becoming more positive [89], [90].

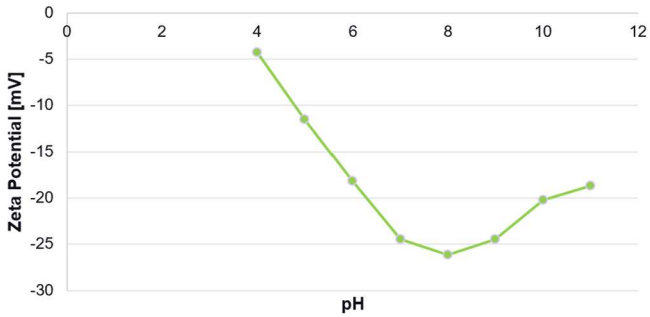

Figure 3.22 – Variation in the zeta potential of $CaCO_3$ particles, upon pH suspension variation.

Analysing the particles obtained, at acidic pH values, zeta potential is negative, close to neutral, reaching approximately -4 mV at pH 4. Never reaching the IEP, the surface increases in negative charge, with the zeta potential decreasing steadily to approximately -27 mV at pH 9. This

behaviour is attributed to the deprotonation of surface –OH and $–CO_3H$ groups, yielding $–O^-$ and $–CO_3^-$ terminated surfaces [91]. The negatively charged surface is stabilized by the adsorption of counterions, Ca^{2+} or H^+, from the medium, and the magnitude of the zeta potential suggests a reasonably high colloidal stability under mildly alkaline conditions [92]. A slight recovery in the zeta potential is observed above pH 9, where the curve begins to ascend moderately, approaching –20 mV at pH 11.

BET surface analysis of $CaCO_3$ particles revealed a BET surface area was 10.41 $m^2 \cdot g^{-1}$, accompanied by a total pore volume of 0.045 $cm^3 \cdot g^{-1}$ and an average pore diameter of 17.13 nm, consistent with the reported data from calcite microspheres [93]. The isotherm derived from the adsorption–desorption data presents the typical features of a nonporous or weakly mesoporous material, with a gradual increase in the adsorbed nitrogen volume as the relative pressure rises. The isotherm plot of Figure 3.23 can be classified between Type II and Type IV according to the IUPAC classification, indicating monolayer–multilayer adsorption on the external surface followed by capillary condensation in mesopores at higher relative pressures [74]. The small hysteresis loop observed during desorption suggests the presence of interparticle voids of irregular geometry, likely slit-shaped mesopores formed by the aggregation of primary calcite particles rather than intrinsic porosity within individual crystals [74].

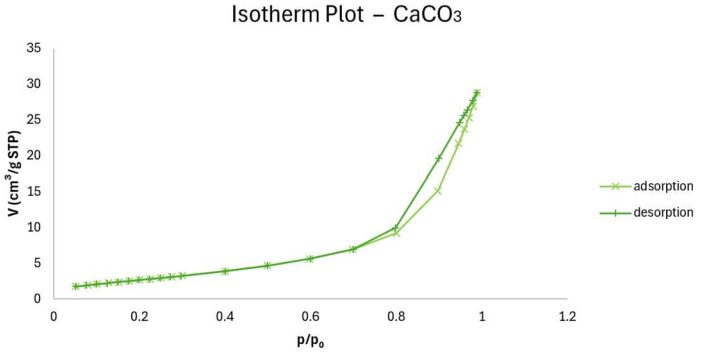

Figure 3.23 – BET isotherm plot of $CaCO_3$ particles.

C was found to be 33.35, indicating a moderately low strength of interaction between the nitrogen adsorbate and the $CaCO_3$ surface [89]. The monolayer capacity (Vm) was calculated as 2.39 $cm^3 \cdot g^{-1}$ (STP), which is consistent with the overall surface area and indicative of a limited number of accessible adsorption sites per unit mass. Precipitated $CaCO_3$ with a calcite polymorph generally shows similar values to the ones obtained when prepared under non-templated conditions. In contrast, vaterite or amorphous $CaCO_3$ particles often present higher surface areas (20–60 $m^2 \cdot g^{-1}$) due to their smaller particle sizes and less dense packing. The relatively low value measured for the present sample thus implies the predominance of large, well-crystallized calcite particles with limited external surface exposure [94]. The overall data may suggest that the sample possesses low external reactivity and a reduced capacity for adsorption-driven processes.

Building upon this physicochemical characterization, the biological behavior of the synthesized $CaCO_3$ NPs was subsequently investigated. Across all tested concentrations (1600

to 1 µg/mL), $CaCO_3$ NPs did not inhibit the growth of *S. aureus* or *E. coli*, as indicated by turbidity in broth cultures and colony formation on agar plates. Accordingly, no MIC or MBC values could be determined.

$CaCO_3$ NPs were evaluated for cytotoxicity/cytocompatibility with MG63 cells through 7 days of exposure time [Figure 3.24]. NPs were tested in the concentration range 1 to 100 µg/mL. Cultures were characterized for metabolic activity (MTT assay, days 1, 4, and 7), DNA content (days 4 and 7), and ALP activity. Results were compared to those of the control cultures (absence of NPs), set up at 100%.

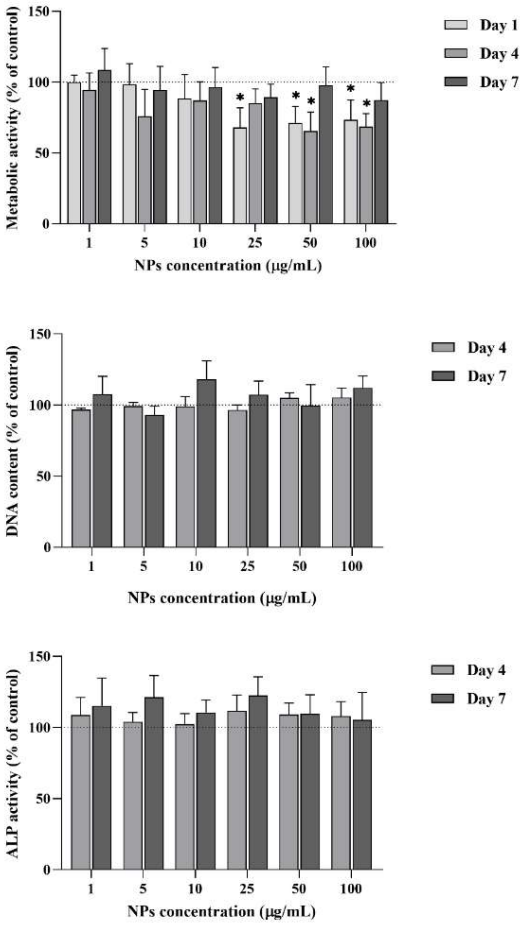

Figure 3.24 – Metabolic activity, DNA content, and ALP activity of MG63 cell cultures exposed to $CaCO_3$ particles (1 to 100 µg/mL) for 7 days. * Significantly different from control, set up at 100%.

Compared to control, exposure to $CaCO_3$ NPs resulted in similar values of metabolic activity at concentrations ≤ 10 µg/mL. At higher concentrations, values were lower on days 1 and 4, but the culture recovered during the exposure, and MTT reduction was similar following 7-day exposure. Regarding DNA content and ALP activity, control and treated cultures presented comparable values.

3.4. Conclusion

This work successfully achieved a novel path for the hydrothermal synthesis, with detailed physicochemical characterization, and preliminary biological evaluation of three Ca-based NPs designed for osteoinductive applications in periodontal tissue regeneration.

The structural characterization confirmed the successful formation of phase-pure crystalline NPs consistent with reference standards. XRD and ATR-FTIR analyses verified the structures, confirming the absence of secondary phases and validating the reproducibility of the adopted synthetic routes. Morphological assessment by SEM and TEM revealed the distinctive architectures of each material: HAp displayed nanorod aggregates forming a “hedgehog-like” morphology; Fe-*β*-TCP formed compact spherical nanoaggregates with homogeneous dispersion of Fe within the matrix; and $CaCO_3$ exhibited well-defined micrometric calcite crystals surrounded by nanospherical particulates. These microstructural differences were further reflected in their BET surface characteristics, where HAp showed the highest surface area (38.73 $m^2 \cdot g^{-1}$), Fe-*β*-TCP demonstrated intermediate values (24.79 $m^2 \cdot g^{-1}$), and $CaCO_3$ exhibited comparatively lower surface accessibility (10.41 $m^2 \cdot g^{-1}$), consistent with their morphological profiles. Zeta potential analysis revealed that all particles presented pH-responsive surface charge behavior, indicating good colloidal stability within the physiological range. Fe-*β*-TCP exhibited an acidic shift in its isoelectric point relative to HAp, a direct consequence of Fe^{3+} substitution within the lattice. The inclusion of Fe was further substantiated by SQUID magnetometry and Mössbauer spectroscopy, which demonstrated paramagnetic behavior with evidence of a low-temperature magnetic transition near 230 K, confirming the coexistence of Fe^{2+} and Fe^{3+} species within the *β*-TCP lattice.

From a biological perspective, the absence of antibacterial activity in all three NP systems against *S. aureus* and *E. coli* indicates that further functionalization or doping may be necessary to achieve antimicrobial performance. Nevertheless, cytocompatibility assays revealed that all materials were non-cytotoxic and maintained high levels of cell viability and metabolic activity. HAp and Fe-*β*-TCP promoted enhanced DNA content and ALP activity, suggesting a positive influence on osteogenic differentiation. $CaCO_3$ also exhibited favorable cellular responses, with transient decreases in metabolic activity at higher concentrations being reversible over time, confirming its suitability for biocompatible hydrogels.

Collectively, the experimental outcomes demonstrate that these Ca-based NPs possess synergistic functionalities that can be strategically integrated into advanced biomaterial systems. HAp offers structural stability and a highly developed surface area favorable for cell adhesion and osteoconduction; Fe-*β*-TCP introduces biodegradability, resorbability, and magnetic responsiveness with potential for osteoinductive enhancement; and $CaCO_3$ contributes additional bioresorbability and potential as a carrier for localized therapeutic delivery. These combined characteristics provide a versatile platform for their incorporation into hydrogel matrices and 3D-

printed composite scaffolds aimed at promoting controlled regeneration of periodontal tissues.

Building upon the findings of this study, future research should aim to deepen the understanding of the interfacial and biological behavior of the synthesized Ca-based NPs under physiologically relevant conditions. Particular attention should be devoted to elucidating the degradation kinetics, ion release profiles, and bioresorption rates within SBF and cell culture environments.

Integrating these NPs into biocompatible polymeric matrices or hydrogel systems represents a logical next step toward developing composite scaffolds with tunable properties. By bridging the gap between materials engineering and biological performance, future developments based on the present findings may lead to new therapeutic platforms that not only restore lost periodontal structures but also actively modulate the local microenvironment to promote sustained tissue regeneration and functional recovery.

Chapter 4
3D printing of functionalized hydrogels for periodontal treatment

Abstract

This work explores the design, optimization, and characterization of gelatin–polycaprolactone (GPCL) hydrogels functionalized with inorganic NPs for bone tissue engineering applications. Four hydrogel formulations were developed: pure GPCL and GPCL composites incorporating HAp, Fe-*β*-TCP, and $CaCO_3$ NPs. The study examined how NP inclusion affected rheological behavior, printability, and structural integrity during extrusion-based 3D printing. Optimal parameters for temperature, pressure, and printing speed were established to ensure controlled deposition and high shape fidelity. Morphological and micro-CT analyses revealed that NP type strongly influenced pore architecture: GPCL displayed uniform porosity, HAp induced denser microstructures, Fe-*β*-TCP increased pore heterogeneity, and $CaCO_3$ generated vertical porosity gradients. Surface evaluation by SEM confirmed consistent trends at the microscale. Degradation studies in SBF and culture medium demonstrated superior structural stability of the GPCL_$CaCO_3$ formulation compared with other variants, which underwent rapid *in vitro* degradation. The enhanced durability of $CaCO_3$-incorporated scaffolds indicates their potential for subsequent biological testing and osteogenic applications. Overall, this research establishes the performance parameters of functionalized GPCL hydrogels, demonstrating their suitability as tunable biomaterials for advanced 3D bioprinting and regenerative periodontal treatment.

4.1. Literature review

4.1.1. 3D printing of NP loaded hydrogels for periodontal regeneration

Current treatment approaches for replacing damaged organs and tissues often rely on autologous tissue harvesting or organ transplantation [95]. However, these methods are inherently limited due to a shortage of available donors and the lack of more effective and sustainable alternatives [95]. In response to these challenges, 3D printing has emerged as a transformative technology, aiming to overcome these barriers by enabling the creation of structures with highly specific porosity, shapes, and intricate designs, such as scaffolds, with remarkable precision [96].

To address the increasing demand for advanced solutions, 3D printing technology has evolved to integrate principles from biological and materials sciences, giving rise to a new tissue engineering approach known as 3D printing. This cutting-edge technique has been extensively researched for its potential to enhance the functionality of tissue engineering constructs [96]. By fabricating implantable patches, 3D printing supports the regeneration of native tissues in terms of anatomical accuracy, precise cellular placement, and the replication of a suitable microenvironment. These bioengineered constructs provide essential mechanical support, facilitate effective nutrient transport for integration into the systemic circulation, and enable the incorporation of multiple cell types required for comprehensive tissue repair [97].

One critical aspect of this technology is the choice of ink, which typically consists of a single biomaterial or a composite of multiple biomaterials in hydrogel form. These inks serve as both substrates for the printing process and as scaffolds for tissue engineering, intending to replicate the structural, physiological, and mechanical attributes of native tissues [98].

Recent advancements in 3D printing have significantly expanded its applications, driven by its unique advantages. These include precise control over scaffold architecture, scalability for clinical applications, and the ability to employ a diverse range of biomaterials. For instance, 3D printing enables fine-tuning of scaffold porosity and the creation of interconnected channels that support efficient nutrient and waste exchange. During the printing process, inks are often cross-linked, ensuring the constructs achieve their desired shape and mechanical properties. Chosen inks can be derived from natural, synthetic polymers, or hybrid materials, each tailored to meet the specific mechanical, rheological, and biological requirements of the target tissue.

The primary techniques employed in 3D printing include inkjet printing, laser-assisted printing, and extrusion-based printing. Inkjet printing, the earliest method, operates similarly to conventional 2D printing, where inks are stored in cartridges and dispensed electronically through a printhead [99]. Laser-assisted printing, derived from laser engraving technologies, involves a donor layer, an energy-absorbing layer, and an ink solution. Laser pulses vaporize targeted regions of the donor layer, propelling droplets of ink onto a receiving substrate, where cross-linking occurs [100]. Extrusion-based printing, a modification of the inkjet method, enables the deposition of highly viscous materials using air pressure pumps or mechanical screw plungers, which makes it particularly suitable for hydrogel-based constructs [101]. For this study, extrusion-based printing was selected due to its efficiency and compatibility with hydrogels.

Hydrogels are three-dimensional, hydrophilic polymer networks that can absorb and retain significant amounts of water or other biological fluids, often exceeding 90% of their total weight, within their interstitial spaces. This high-water content, combined with their structural and functional resemblance to the natural extracellular matrix, makes hydrogels highly attractive for a wide range of biomedical applications. They have been extensively utilized in drug delivery systems, wound dressings, biosensors, and tissue engineering, serving as versatile platforms for both therapeutic and diagnostic purposes [102].

Despite their promising potential, hydrogels face several challenges that limit their broader clinical application, including inadequate mechanical strength, low thermal and enzymatic stability, and rapid degradation rates in physiological environments [103]. Addressing these limitations requires advanced material engineering and functionalization strategies to enhance their physicochemical and biological properties.

4.1.2. Gelatin-based hydrogels

The modification of gelatin-based hydrogels through functionalization constitutes a key approach in enhancing hydrogel properties. Gelatin, a biopolymer derived from collagen, offers inherent biocompatibility and bioactivity [104]. Functionalized gelatin hydrogels can undergo efficient crosslinking, resulting in more stable and tunable structures due to the formation of covalent or non-covalent bonds between polymer chains, which significantly impacts the mechanical and thermal properties of the hydrogel [105]. Hydrogels with a lower degree of crosslinking exhibit enhanced elasticity and flexibility, while those with higher crosslinking density demonstrate increased rigidity and structural integrity, making them suitable for load-bearing or high-stress applications [106].

Furthermore, integrating gelatin-based hydrogels with other biomaterials, such as NPs, growth factors, or bioactive ceramics, can create synergistic effects that amplify their functionality [107]. For instance, hybrid hydrogels combining gelatin with NPs can provide enhanced mechanical properties, controlled degradation rates, and tailored bioactivity. Such combinations also enable the development of stimuli-responsive hydrogels, which can respond to environmental triggers such as temperature, pH, or ionic strength, thereby broadening their scope for precision medicine and regenerative therapies [103].

To further investigate the current state-of-the-art, a review was conducted, focusing on various types of gelatin-based hydrogels in the treatment of periodontitis, as outlined in Table 4 of the Appendice I. As an example, Caballero-Flores *et al.* developed a gelatin-chitosan-genipin hydrogel, crosslinked using genipin and subjected to freeze-drying to create porous structures critical for cellular adhesion and proliferation. This innovative hydrogel not only fostered a microenvironment conducive to tissue regeneration but also exhibited notable antibacterial properties, effectively reducing bacterial colony-forming units by day six [108].

In a similar work, Dallas Ortega *et al.* introduced a gelatin/nisin hydrogel that leveraged temperature-induced crosslinking. This hydrogel provided a sterile environment by disrupting bacterial membranes, while creating a 3D structure to support tissue regeneration [109]. The hydrogel was highly effective against *Staphylococcus aureus* and *Pseudomonas aeruginosa*, proving its dual regenerative and antibacterial functionalities [109]. Other studies have focused

on integrating HAp into gelatin-based scaffolds, thereby enhancing their osteogenic potential. For example, Huang *et al.* demonstrated that gelatin-HAp hydrogels mimic the extracellular matrix to promote osteogenesis and cementogenesis, thereby enhancing periodontal regeneration [110].

The incorporation of advanced structural configurations has also been explored. Kim *et al.* developed gelatin-HA(hyaluronic acid)-HAp scaffolds through temperature crosslinking and biomineralization techniques. These scaffolds demonstrated high bioactivity, which facilitated superior cell attachment, proliferation, and differentiation [111]. Similarly, Han *et al.* fabricated 3D-printed gelatin-fibrinogen scaffolds, which served as inks for odontogenic differentiation and collagen integration, thereby enhancing scaffold-bone integration [112].

In addition to promoting osteogenesis, some gelatin-based hydrogels have exhibited strong antibacterial properties. For instance, Liu *et al.* introduced a gelatin-PLA-MgO hydrogel prepared via electrospinning, which not only enhanced osteogenic differentiation *in vitro* but also suppressed bacterial growth by over 90% within 24 hours against pathogens such as *E. coli* and *S. aureus* [113]. Similarly, Dong *et al.* reported the development of a gelatin-CaO_2 hydrogel crosslinked with oxidized dextran. This hydrogel created an alkaline environment that promoted osteogenic differentiation while demonstrating robust antibacterial efficacy against *Porphyromonas gingivalis* [114].

A parallel trend in these studies is the use of crosslinking agents to enhance the mechanical and biological properties of gelatin hydrogels. For example, Outstadi *et al.* utilized genipin to crosslink a gelatin-PLLA hydrogel, improving its mechanical properties and making it suitable for mimicking the natural bone matrix [115]. Dou *et al.* used carbodiimide crosslinking with EDC and NHS to fabricate gelatin-PLGA-HAp scaffolds, which facilitated early-stage cell adhesion and proliferation while promoting new bone formation and scaffold integration with host tissue [116].

The slow-release properties of hydrogels have also been leveraged for antibacterial efficacy. Sun *et al.* developed a gelatin-alginate hydrogel crosslinked with transglutaminase, which acted as a slow-release system for antibiotics. This hydrogel demonstrated significant improvements in bone volume and structure, along with effective antibacterial activity against methicillin-resistant *Staphylococcus aureus* and other strains [117]. In another study, Hutomo *et al.* focused on the structural stability and biocompatibility of gelatin-EDC-NHS hydrogels, enhancing gingival fibroblast proliferation and differentiation [118].

Still, a critical gap persists in the literature concerning the development of dual-step strategies to address this multifaceted disease, as well as the mitigation of the inherently rapid degradation of gelatin, without the use of photopolymerization. To address these challenges, this thesis proposes the incorporation of another polymer, PCL, into gelatin hydrogels, evaluating its impact on both degradation behavior and printability.

4.1.2.1. PCL

PCL is a synthetic, aliphatic polyester derived from petrochemical sources and is well recognized for its biodegradability and biocompatibility. As a semi-crystalline and hydrophobic polymer, PCL exhibits a relatively low melting temperature in the range of 59–64 °C. Depending on the molecular weight, which can vary from approximately 3,000 to 90,000 g/mol, PCL exhibits different levels of crystallinity, with higher molecular weights generally associated with reduced crystallinity [119]. In terms of solubility, PCL easily dissolves in a variety of organic solvents, such as chloroform, dichloromethane, acetic acid, benzene, and toluene, but exhibits poor solubility in polar solvents such as alcohols and acetone [120], [121], [122], [123].

Due to its distinctive combination of biocompatibility and biodegradability, PCL has garnered significant attention in biomedical research. Unlike conventional polyolefins that persist in the environment for centuries, PCL undergoes gradual degradation through hydrolytic and enzymatic processes, yielding non-toxic byproducts within a relatively short timescale [119]. These attributes have facilitated its use in diverse applications such as controlled drug delivery systems, resorbable sutures, vascular grafts, wound dressings, and scaffolds for bone and cartilage tissue engineering [124]. However, its inherent hydrophobicity and slow degradation rate limit cellular adhesion and timely resorption in periodontal regeneration applications. In particular, its ability to be copolymerized or blended with other polymers has enabled the tailoring of degradation rates and mechanical strength to meet the specific biomedical requirements of each application [125] [126].

Blending PCL with natural biopolymers such as gelatin has emerged as a promising strategy to overcome these limitations. The incorporation of gelatin enhances the hydrophilicity and bioactivity of PCL-based scaffolds. This combined hydrogel approach improves cell attachment, proliferation, and differentiation by providing bioactive environments that interact with receptors on periodontal ligament stem cells. Furthermore, gelatin accelerates the biodegradation kinetics of PCL while maintaining the structural integrity required for guided tissue regeneration throughout the healing process [127]. As an example, Tian *et al*. developed trilayered gelatin/PCL nanofibers that closely mimic the native architecture of the periodontal ligament–bone interface. Their results revealed enhanced proliferation and osteogenic differentiation of human periodontal ligament stem cells, accompanied by increased mineralization and upregulation of osteogenic gene expression. The hierarchical scaffold design facilitated the spatial organization of cells, supporting functional tissue regeneration [128]. Other investigations corroborate these findings, reporting that 3D printed and electrospun PCL/gelatin scaffolds promote angiogenesis and osteogenesis while enabling PDL fiber alignment [120], [121], [122], [123], [127]. Moreover, their controlled degradation profiles align with the physiological timeline of periodontal tissue healing, thus providing a favorable microenvironment for coordinated regeneration of both soft and hard tissues [119].

4.2. Materials and Methods

4.2.1. Materials

Gelatin (95%) and glycerin (99%) were both purchased from LABCHEM (Portugal). Sucrose was obtained from Fisher Scientific (USA). NPs were synthesized in-lab [as described in the previous chapter]. Poly(ε-caprolactone) (PCL, Mn ≈ 14,000 g·mol^{-1}) was purchased from Sigma-Aldrich (USA), and PCL (Mn ≈ 80,000 g·mol^{-1}) was obtained from Thermo Scientific (USA).

4.2.2. Preparation of Gelatin-PCL-based hydrogels

Hydrogel formulations were prepared by combining deionized water and glycerin in a glass Schott flask, which was placed in a water bath maintained at 50 °C. For formulations containing NPs, the NPs were added simultaneously with the water. Once the solution reached the target temperature, sucrose and gelatin were introduced. The mixture was then subjected to an ultrasonic bath [ARGO LAB, AU-32] for 1 hour while maintained at 50 °C to facilitate homogenization and eliminate air bubbles, as described in Figure 4.1, and with the specific percentages of each component used in the hydrogel formulations detailed in Table 4.1.

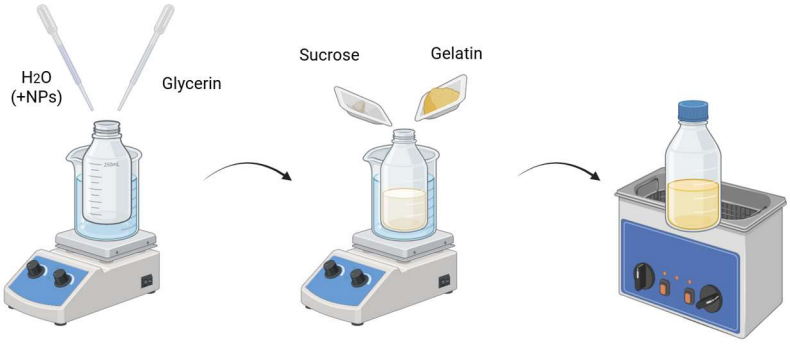

Figure 4.1 – Preparation of Gelatin-PCL-based hydrogels, designed with software BioRender.

Table 4.1 – Hydrogel formulations in percentage.

Reagent	**Gel50** [%]	**Gel50 + NPs** [%]
Glycerin	8.7	8.7
H_2O	32.6	31.6
Sucrose	8.7	8.7
Gelatin	50	50
NPs	---	1

The final Gel50+PCL (GPCL) formulation was prepared by combining equal parts of Gel50 with a mixture containing 50% PCL14000 dissolved in chloroform, followed by thorough mixing to ensure homogeneity.

4.2.3. Characterization of hydrogels

This section outlines the experimental procedures employed to assess the physicochemical and functional properties of the developed hydrogels. The characterization includes rheological behavior, surface wettability through water contact angle measurements, degradation profiles, and chemical structure analysis.

4.2.3.1. ATR-FTIR spectroscopy

ATR-FTIR spectroscopy was employed to identify the characteristic vibrational bands associated with specific chemical bonds, thereby confirming the incorporation of functional groups and potential interactions between components in composite systems. The measurements were carried out using a Nicolet 5700 FT-IR [Thermo Electron Corporation, USA] equipped with a diamond crystal, operating in the range of 4000-400 cm^{-1} with a spectral resolution of 4 cm^{-1}. All spectra were collected at room temperature, after the measurement of the vibrations in the environment. The ATR-FTIR measurements were performed through a collaborative protocol between IPS and CQE/Instituto Superior Tecnico.

4.2.3.2. Water contact angle

To assess the wettability and surface energy characteristics of the produced hydrogels, static water contact angle measurements were performed. A 20 µL droplet of distilled water was gently deposited onto the hydrogel surface at a perpendicular (90°) angle. The contact angle formed between the water droplet and the hydrogel surface was captured using the burst mode of an OM-D E-M10 camera (Olympus, Japan) with a macro 60mm lens. The resulting images were subsequently analyzed using ImageJ software to determine the contact angle values, thereby indicating the hydrophilic or hydrophobic nature of the biomaterial.

4.2.3.3. Degradation tests

The water absorption and biodegradability of the scaffolds were evaluated by immersing them in a SBF solution. Two types of specimens were used: dense hydrogel cubes with side lengths of 80 mm and a height of 50 mm, and 3D-printed scaffolds with square bases measuring 170 mm on each side and a height of 1 mm. Each sample was placed in a 6-well cell culture plate containing 10 mL of SBF solution at pH 7.4. The plates were left in an oven at 37 °C. At predetermined time intervals (1, 2, 3, 7, 14, and 21 days), the scaffolds were retrieved, rinsed

twice with distilled water, and dried in a desiccator for 7 days. Structural integrity was assessed via an Illuminated Stereo Microscope ZoomM 2000 [Leica, Germany]. Both hydrated and dehydrated samples were weighed using an analytical balance. Water absorption and weight loss were calculated according to Equations 4.1 and 4.2, respectively.

$$Water\ absortion\ (\%) = \frac{W_{wet\ 3D\ structures} - W_0}{W_0} \times 100 \quad (4.1)$$

$$Weigth\ loss\ (\%) = \frac{W_0 - W_{dry\ 3D\ structures}}{W_0} \times 100 \quad (4.2)$$

Where W_0 is the initial weight of the 3D structures before conducting the tests, $W_{wet\ 3D\ structures}$ corresponds to the weight of the wet 3D structures after a specific immersion time, and $W_{dry\ 3D\ structures}$ refer to the weight of the dry 3D structures after each drying stage.

4.2.3.4. Rheological characteristics

The rheological behavior of the hydrogels was evaluated using a Kinexus rheometer (NETZSCH, Germany) equipped with the PU20 SR 3098 SS accessory. Measurements were conducted over a temperature range of 55°C to 25°C, applying a cooling rate of 2.5°C/min. Data were collected at 15-second intervals, using a constant working gap of 1 mm.

4.2.4. 3D printing of functionalized hydrogels

4.2.4.1. Printing parameters

To determine the optimal printing temperature, each gelatin-PCL-based hydrogel formulation was loaded into the cartridge of the Allevi 2 hydrogel 3D printer and subjected to gradual heating until the printed structure exhibited the desired line width compatible with the 25G red plastic tapered nozzle, as illustrated in Figure 4.2.

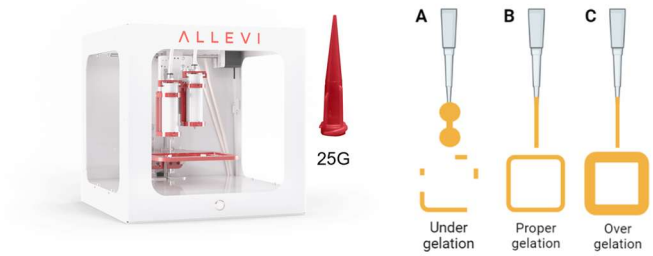

Figure 4.2 – Hydrogel 3D printer, and how to evaluate proper gelation, designed with software BioRender.

4.2.4.2. Line tests

To determine the optimal printing speed, a line test was conducted comparing three different

speeds (300 mm/s, 600 mm/s, and 900 mm/s) using a specific nozzle, as illustrated in Figure 4.3.

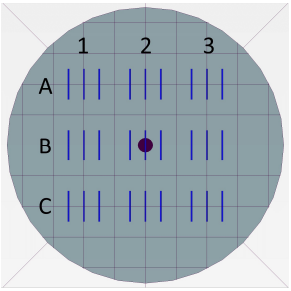

Figure 4.3 – Speed line tests, retrieved from [129].

Linear filaments with 50mm in length were printed under optimal temperature and pressure conditions, defined in the previous section, to analyze the impact of these parameters on experimental filament width (W'), compared to the nozzle gauge, corresponding to the deviation described in Equation 4.3.

$$\%Deviation = \left(\frac{W' - W}{W}\right) \times 100 \tag{4.3}$$

For this test, the nozzle used was the red plastic tapered tip needle, with a gauge of 25G, corresponding to 0.25mm of inner diameter (W) [130].

Furthermore, to investigate the influence of angular geometry on the line definition of the printed structures, a star-shaped design was tested, comprising interior angles of 36º and exterior angles of 108º. Additionally, a configuration with an angle of 90º was also examined. The widths of both the straight segments and the junctions formed at the angles were measured to assess the differences.

4.2.4.3. Scaffold tests

To create biocompatible structures similar to the extracellular matrix of the periodontium tissues, the 3D models used to test the printing parameters of the hydrogels were designed to have a specific porosity. This porosity was achieved by printing in layers with different orientation angles, these angles being 45º, 90º, and -45º [Figure 4.4]. All layers were printed with a 0.15 mm layer height, 30 mm/s printing velocity, and 0.6 mm line width.

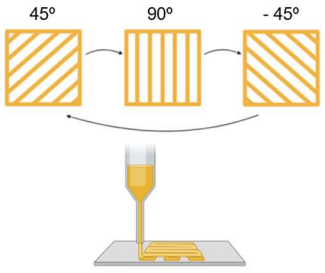

Figure 4.4 – Different orientation angles in the printing process, designed in software BioRender.

4.2.4.4. Micro-Computed Tomography

The 3D structural characterization of the hydrogel membranes was performed using a micro-computed tomography (micro-CT) system NeoScan N60 [Neoscan, Belgium]. The 3D structures were scanned using an aluminium filter of 0.5 mm to optimize beam hardening correction and improve image contrast. The rotation step was set to 0.20°, ensuring high-resolution image acquisition throughout the 360° rotation. For each projection, 35 frames were averaged to reduce noise and enhance image quality. The resulting scans were reconstructed with an image pixel size of 7.4 µm, allowing detailed visualization and quantitative analysis of the internal microarchitecture of the hydrogel membranes.

4.2.4.5. Biological characterization

Since the particles demonstrated no antibacterial activity, the procedures employed to evaluate the biological performance of the 3D-printed scaffolds focused primarily on assessing whether NP functionalization conferred the intended osteoinductive properties and maintained stability in cellular media.

For the cytocompatibility to osteoblastic cells, MG63 cells (5x103 cells/cm^2) were cultured in alpha-minimum essential medium (α-MEM) supplemented with 10% fetal bovine serum (FBS), 100 IU/mL penicillin, 100 µg/mL streptomycin, and 2.5 µg/mL amphotericin B (All reagents from Gibco, NY, USA), for 24 hours, for cell adhesion. Subsequently, cultures were exposed to the 3D-printed membranes' extracts for periods up to 7 days. Cultures performed in the absence of the extracts were used as a control.

For the preparation of the extracts, following the ISO 10993 standard, the membranes were sterilized under UV light for 30 min on each side, incubated in α-MEM supplemented with antibiotics for 24 hours, and subsequently, the supernatant was collected and diluted (5% and 10%) to be added to the adhered cell cultures. The membrane of GPCL_$CaCO_3$ (the unique membrane that preserved the integrity in culture medium) was seeded with MG63 cells ($4x10^4$ cells/cm^2) and cultured for periods up to 7 days.

Cultures were incubated at 37°C in a humidified 5% CO_2 atmosphere. In both assays, cultures exposed to the membranes' extracts (indirect assay) and cultures performed over the membrane GPCL_$CaCO_3$ (direct assay) were characterized for metabolic activity (MTT assay), morphology (F-actin staining), and ALP activity. Some of these methods were the same as those described in Appendix II.

4.3. Results and Discussion

This section presents and discusses the results obtained from the characterization, printing,

and biological evaluation of the functionalized hydrogels developed for periodontal regeneration. The findings are analyzed in relation to the physicochemical, structural, and biological properties of the hydrogels, as well as their performance during the 3D printing process.

4.3.1. Characterization of Hydrogels

For the characterization of the hydrogels, the influence of PCL on the structural properties of the polymer-polymer matrix and on the degradation behaviour was first evaluated [Figure 4.5].

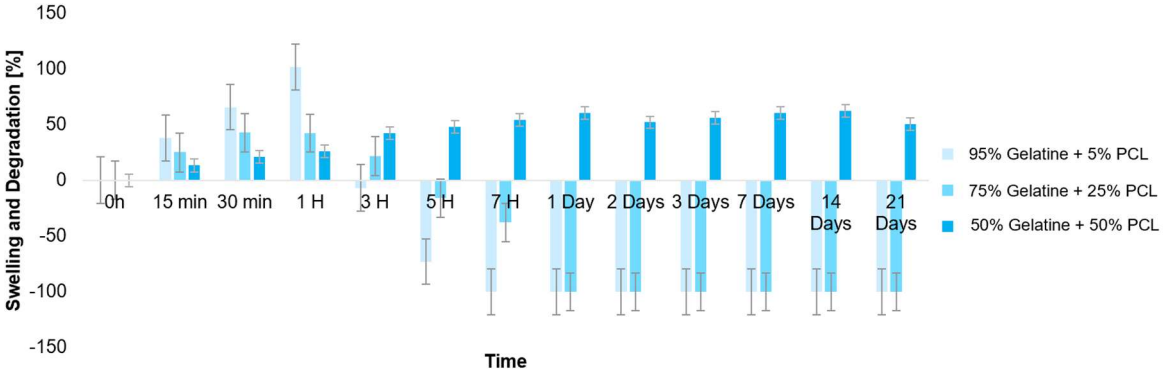

Figure 4.5 – Swelling and degradation of GPCL with different compositions, in PBS at pH 7.4 and 37ºC.

Based on the obtained data, it can be inferred that the formulation containing 50% gelatin and 50% PCL exhibited the most favorable performance, as it remained partially intact after 21 days of degradation. To further investigate the structural differences between the formulations, the ATR-FTIR spectra of the gelatin hydrogel (Gel) and the PCL/gelatin hydrogel (GPCL) are presented in Figure 4.6.

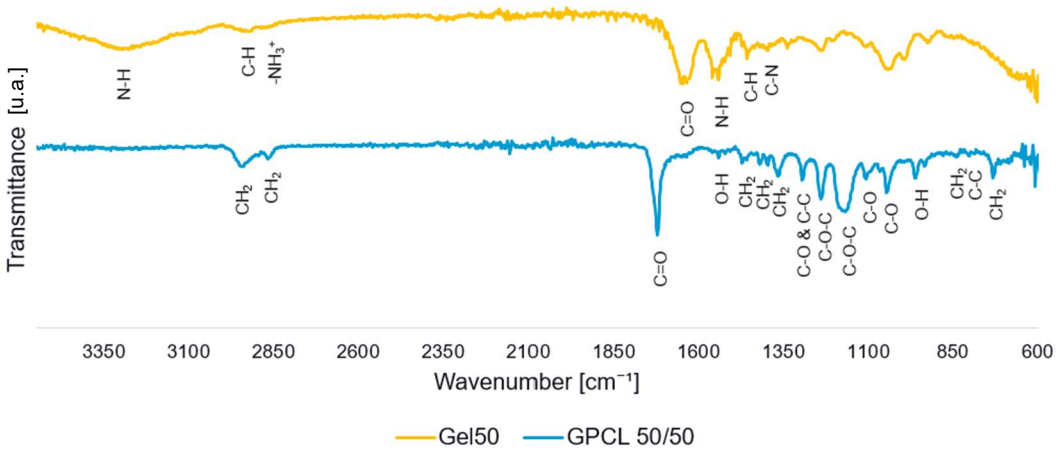

Figure 4.6 – ATR-FTIR spectra of Gel50 and GPCL.

In the FTIR spectrum of Gel, characteristic absorption bands were observed at 1633 cm^{-1}, corresponding to the C=O stretching vibration (amide I), and at 1544 cm^{-1}, attributed to N–H bending vibrations (amide II). Additional bands were detected at 1452 cm^{-1} and 1338 cm^{-1},

corresponding to C–H bending and C–N stretching vibrations, respectively [131]. Furthermore, bands characteristic of Amide A and Amide B were also present, appearing around 3100-3400 cm^{-1} and 2852-2851 cm^{-1}, respectively, with the first overlapping with O-H stretching from water. These bands arise from N–H stretching vibrations and are commonly associated with hydrogen bonding and peptide structures in gelatin [132].

As for the FTIR spectrum of the GPCL hydrogel, it exhibited its typical characteristic peaks at 2948 cm^{-1} (asymmetric $–CH_2$ stretching), 2859 cm^{-1} (symmetric $–CH_2$ stretching), 1718 cm^{-1} (C=O stretching), 1294 cm^{-1} (C–O and C–C stretching), 1239 cm^{-1} (asymmetric C–O–C stretching), and 1169 cm^{-1} (symmetric C–O–C stretching) [133]. The peaks at 2948 cm^{-1} and 2859 cm^{-1} are again attributed to the stretching vibrations $–CH_2$ groups; the sharp band at 1718 cm^{-1} is indicative of the ester carbonyl (C=O) stretching vibration; the absorption at 1294 cm^{-1} arises from C–O and C–C stretching associated with the polymer backbone; while the bands at 1239 cm^{-1} and 1169 cm^{-1} are assigned to asymmetric and symmetric C–O–C stretching vibrations, characteristic of ester linkages. The spectrum retains the amide I and II bands, indicating that the gelatin structure remains intact, with subtle shifts and intensity changes in these bands suggesting potential hydrogen bonding or dipole–dipole interactions between the gelatin and PCL chains. As for the bands in the lower frequency (below 900 cm^{-1}), these may correspond to skeletal deformations, out-of-plane C–H bending, and crystalline lattice modes of PCL [134].

Upon functionalization, the ATR-FTIR spectra revealed noticeable differences, even at low particle concentrations within the hydrogels [Figure 4.7]. Three spectral regions were analysed in detail: 3000-2800 cm^{-1}, 1800-1500 cm^{-1}, and 900-750 cm^{-1}.

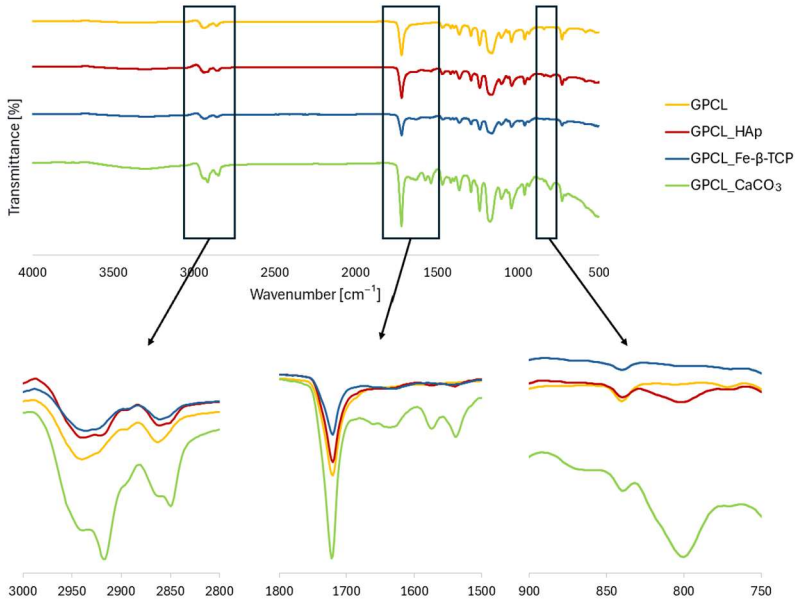

Figure 4.7 – ATR-FTIR spectra of GPCL and GPCL_NPs, with zooms on predominantly heterogeneous transmittances between hydrogels.

In the high-wavenumber region between 3000 and 2800 cm^{-1}, characteristic absorption

bands corresponding to the asymmetric and symmetric stretching vibrations of methylene groups ($\nu_{assymetric}(CH_2)$ ≈ 2920–2950 cm^{-1} and $\nu_{symetric}(CH_2)$ ≈ 2850–2870 cm^{-1}) are observed. These bands primarily originate from the aliphatic chains of PCL, while gelatin contributes less intensely in this region [135]. The spectra of the unmodified GPCL and those containing HAp or Fe-*β*-TCP display similar profiles, indicating preservation of the PCL chain environment. However, the $CaCO_3$-containing hydrogel exhibits noticeable broadening and intensity variations in these CH_2 stretching bands. Such changes suggest reduced segmental mobility of PCL chains and increased interfacial interactions between the polymer matrix and $CaCO_3$. The small downshifts and broadening observed across all hydrogels indicate enhanced hydrogen bonding or van der Waals interactions that restrict polymer chain movement, with the effect being most pronounced for the $CaCO_3$ hydrogel [136].

The mid-infrared region between 1800 and 1500 cm^{-1} covers the carbonyl and amide absorptions of both polymeric components. A strong absorption near 1720-1730 cm^{-1} corresponds to the stretching vibration of the ester carbonyl (C=O) group in PCL [137]. Gelatin contributes prominent Amide I and Amide II bands, centred around 1640–1660 cm^{-1} and 1530–1550 cm^{-1}, respectively, arising from C=O stretching and N–H bending/C–N stretching modes of the peptide backbone [131]. Upon incorporation of NPs, the Amide I band undergoes a slight shift to lower wavenumbers and exhibits increased bandwidth in the hydrogels containing HAp, Fe-*β*-TCP, and most notably $CaCO_3$. These spectral modifications indicate the formation of hydrogen bonds or coordination interactions between the carbonyl groups of gelatin or PCL and surface cations such as Ca^{2+} or Fe^{3+} [138]. The observed downshift in the Amide I band is consistent with a weakening of the C=O bond due to hydrogen bonding, while the relative intensity changes between Amide I and Amide II suggest minor alterations in gelatin's secondary structure [139].

In the region between 900 and 750 cm^{-1}, GPCL_$CaCO_3$ exhibits a strong and well-defined band near 870 cm^{-1}, characteristic of the out-of-plane bending vibration (ν_2) of the carbonate ion (CO_3^{2-}) [85]. This feature, absent in the spectra of the other hydrogels, provides direct spectroscopic confirmation of $CaCO_3$ incorporation within the hydrogel matrix. Additional minor peaks around 710-720 cm^{-1} further support the presence of calcite phases [88]. In contrast, the spectra of GPCL_HAp and GPCL_Fe-β-TCP show only weak activity in this range, as their phosphate (PO_4^{3-}) vibrations occur predominantly at higher wavenumbers (approximately 1000–1100 cm^{-1} for ν_3 and 560-600 cm^{-1} for ν_4 modes) [61].

Among the tested hydrogels, the GPCL_$CaCO_3$ demonstrates the strongest perturbations across all spectral regions, suggesting the formation of strong interactions between $CaCO_3$ and the polymer network, likely contributing to its altered bonds. Such phenomena are likely to influence the hydrogel's macroscopic properties, including its hydrophilicity, structure, and stability. In agreement with this interpretation, the subsequent water contact angle measurements [Figure 4.8] provide further insight into how these nanoscale interactions translate into observable changes in surface wettability.

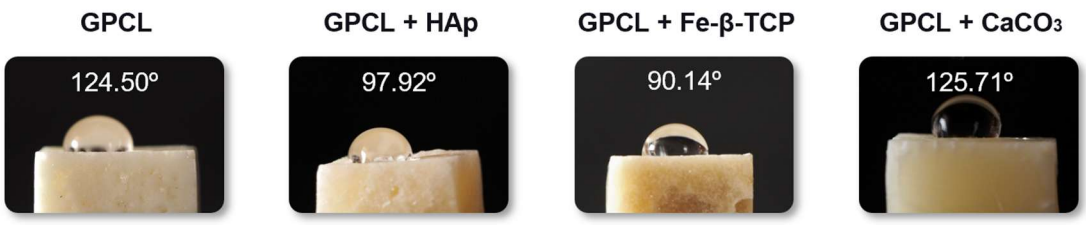

Figure 4.8 – Water contact angle of H_2O droplet in each hydrogel.

The unmodified GPCL hydrogel exhibited a contact angle of 124.5±1.2°, indicating a predominantly hydrophobic surface. Upon functionalization with HAp particles, the contact angle decreased significantly to 97.9±2.6°, indicating an increase in surface hydrophilicity. This enhancement is likely attributable to the inherent hydrophilic nature and surface roughness introduced by HAp, which promotes better water spreading. Similarly, functionalization with Fe-*β*-TCP NPs resulted in a slight decrease in the contact angle of 90.14±4.6°, approaching the threshold for hydrophilicity [140].

Conversely, the incorporation of $CaCO_3$ led to a contact angle of 125.71±1.1°, which is slightly higher than that of the GPCL hydrogel. This suggests that $CaCO_3$ may potentially enhance the hydrophobic character due to particle morphology or surface chemistry, as proven in the degradation tests. It is also important to note that the surface uniformity and smoothness of the hydrogels may influence these measurements.

The rheological analysis of GPCL hydrogels and their composites with different particles, illustrated in Figure 4.9, also reveals differences in the thermo-viscous behavior of the systems.

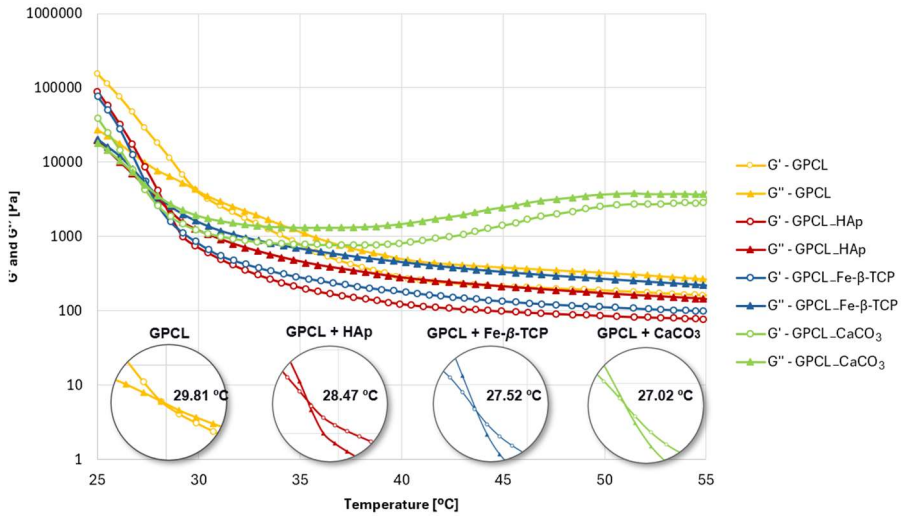

Figure 4.9 – Rheological behavior of hydrogels through temperature variation.

GPCL hydrogel demonstrates the characteristic thermoresponsive profile of gelatin-based matrices [141]. At lower temperatures, it exhibits a very high viscosity, which decreases sharply as the temperature increases towards physiological conditions. This behavior reflects the gradual

disruption of gelatin's triple-helical domains and the transition to a more disordered coil conformation [142]. The viscosity subsequently stabilizes at a plateau at 40ºC, indicating that a new equilibrium is achieved.

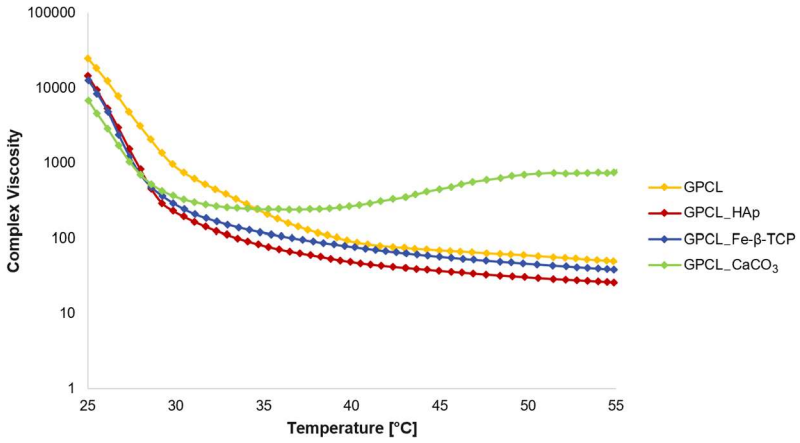

Figure 4.10 – Behaviour of complex viscosity of the hydrogels through temperature variation.

When HAp is incorporated, the hydrogel exhibits the lowest viscosity values across the entire temperature range. This suggests that HAp particles interfere with the native polymer–polymer interactions of the hydrogel, most likely by reducing the effective density of crosslinks within the network. The outcome is a hydrogel that remains structurally weaker but highly flowable, which is advantageous for applications requiring injectability, but not ideal for 3D printing. Moreover, the diminished viscosity also implies reduced post-gelation mechanical stability, which could limit its applicability in load-bearing scenarios [142]. The addition of Fe-*β*-TCP produces an intermediate response. Compared to GPCL_HAp, the hydrogel maintains higher viscosity values, although it remains lower than that of the GPCL hydrogel.

The most distinctive rheological profile is observed in the GPCL_$CaCO_3$ hydrogel. Similar to the other hydrogels, viscosity initially decreases with increasing temperature. However, beyond approximately 37 °C, the viscosity begins to increase steadily, reaching the highest values among all at temperatures above 45 °C. From an application perspective, this property is highly advantageous, as the hydrogel remains easily printable at slightly above room temperature but becomes significantly less viscous once exposed to physiological conditions, offering a material well-suited for *in situ* scaffolds or bone defect fillers.

Having the hydrogels characterized, the degradation and swelling behaviors of GPCL hydrogel and its composites with NPs were systematically evaluated through immersion in SBF over 21 days, to see if the previously inferred characteristics had an impact on degradation and if the particles disturbed the hydrogel matrix. The results [Figure 4.11] combine quantitative assessments of weight loss and water uptake with representative macroscopic images of the scaffolds at different immersion times.

All hydrogels exhibited similar low weight loss within the first 24 hours, confirming their initial

stability in aqueous medium. From Day 7 onwards, marked differences emerged. The GPCL_Fe-β-TCP scaffolds demonstrated the most accelerated degradation, reaching nearly 80% weight loss after 21 days. This behavior is likely attributed to the hydrophilicity, demonstrated with the water contact angle tests. GPCL_HAp followed a similar trend, with degradation approaching 75% at Day 21, consistent with the less soluble nature of HAp. In contrast, GPCL and GPCL_$CaCO_3$ degraded more gradually, reaching approximately 60% and 55% weight loss, respectively. The relative stability of the GPCL_$CaCO_3$ formulation may be related to the buffering capacity of $CaCO_3$, which reduces the autocatalytic degradation typically associated with polyesters. These results are supported by the macroscopic observations, where GPCL_Fe-*β*-TCP exhibited severe fragmentation after 14 days, while GPCL_$CaCO_3$ maintained its morphology throughout the experiment.

The swelling behavior is consistent with the previously stated. GPCL_$CaCO_3$ exhibited the highest swelling capacity, with weight gain peaking at around 90% on Day 7. Despite this higher hydration, the scaffold retained its shape, demonstrating that water uptake did not compromise its stability. GPCL followed a similar but less pronounced trend, reaching a maximum swelling of 60% before gradually decreasing due to concurrent degradation. GPCL_HAp exhibited moderate swelling that stabilized after 14 days. GPCL_Fe-β-TCP exhibited unstable swelling kinetics, characterized by an initial increase over the first 3 days, followed by a sharp decrease, resulting in negative values at Day 21. This behavior indicates that scaffold collapse and extensive degradation rapidly surpassed water absorption capacity, leading to material disintegration.

It is possible to infer that incorporating different particles into the hydrogel matrix has a significant influence on scaffold performance. These results prove that the GPCL is capable of surviving at least 21 days in an SBF solution, representing a substantial improvement over previous gelatin-based hydrogels.

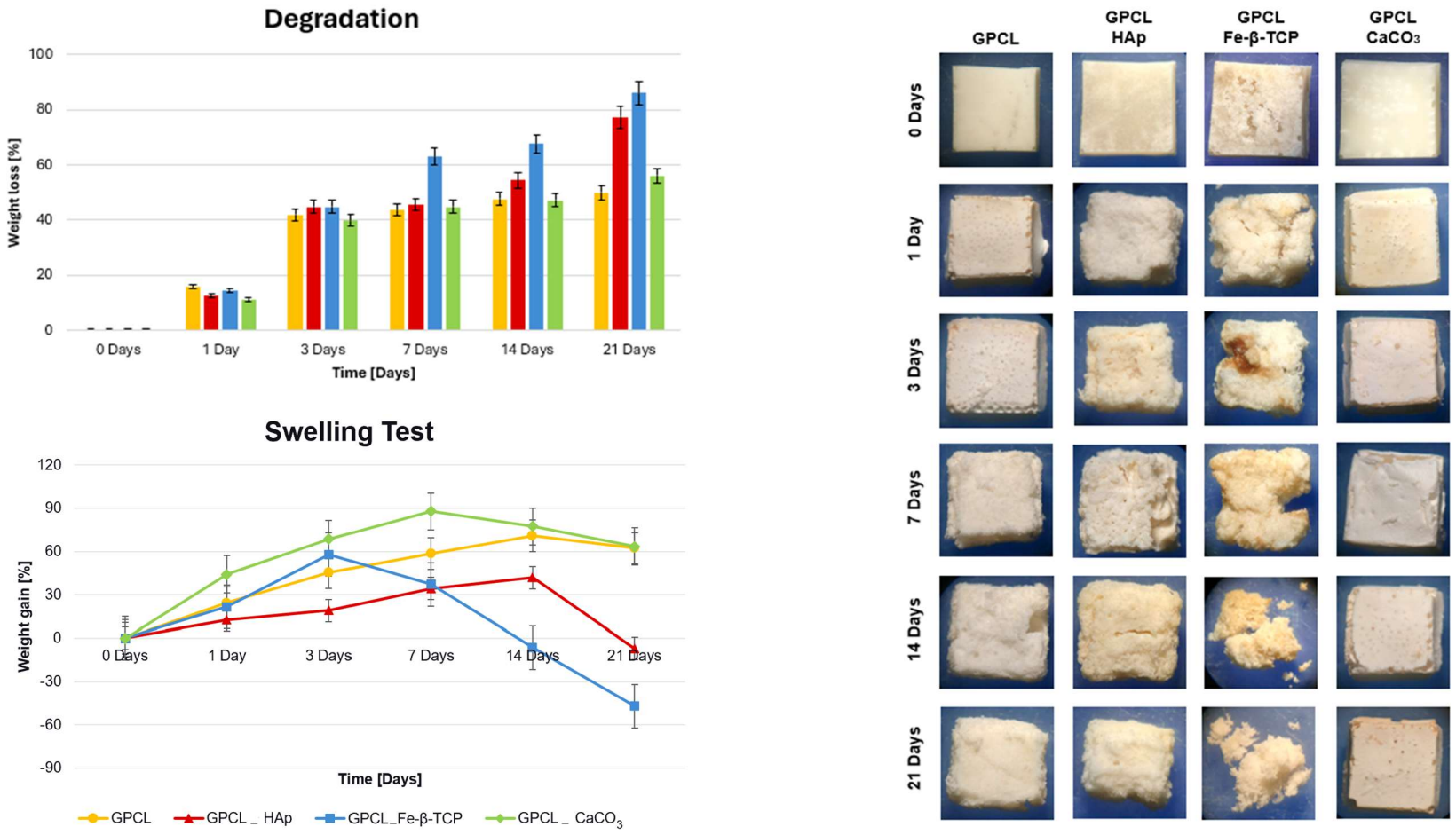

Figure 4.11 – Degradation and Swelling behaviour of GPCL hydrogels in SBF at 37ºC.

4.3.2. 3D printing of functionalized hydrogels

To initiate the analysis of the printing parameters, the optimal temperature of the printer cartridge and the applied internal pressure were evaluated, as presented in Figure 4.12.

Table 4.2 – Optimal printing temperature and pressure for each hydrogel to achieve proper gelation.

	Temperature [ºC]	Pressure [PSI]
GPCL	25	25
GPCL_HAp	32	
GPCL_Fe-β-TCP	35	
GPCL_$CaCO_3$	35	

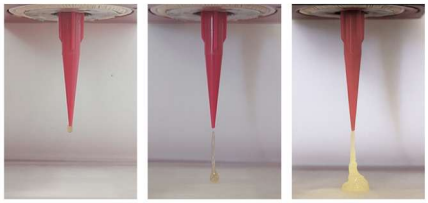

Figure 4.12 – Experimental examples of under, proper, and over gelation.

As described in Table 4.2, the control formulation, GPCL, exhibited ideal flow behavior at room temperature (25 °C), without the need for cartridge heating. In contrast, the functionalized hydrogels with NPs required heating of the cartridge to reach similar levels of printability. Specifically, GPCL combined with HAp required heating to 32 °C to achieve proper gelation. Formulations containing Fe-*β*-TCP and $CaCO_3$ demanded an even higher temperature of 35 °C to ensure optimal flow characteristics. These temperature increases can be attributed to the influence of the NPs on the rheological and gelation behavior of the base hydrogel, needing cartridge heating to maintain appropriate extrusion conditions. Regarding pressure, all hydrogels demonstrated good printing performance when a constant pressure of 25 PSI was applied, being sufficient to ensure continuous and stable extrusion across all hydrogels.

As shown in Table 4.3 and Figure 4.13, a clear inverse correlation between printing speed and filament thickness was confirmed. At a slower speed of 300 mm/min, the printed filament exhibited a width of approximately 1.59 mm, corresponding to a percentage deviation of 536% relative to the nominal nozzle diameter. In contrast, at intermediate and higher speeds of 600 mm/min and 900 mm/min, the filament widths decreased to 1.16 mm and 0.67 mm, with associated deviations of 364% and 168%, respectively. This trend is consistent with the expected behaviour: higher speeds diminish the biomaterial at the extrusion nozzle, yielding narrower printed lines [143]. In view of the objective of producing scaffolds with high and well-defined porosity, a higher printing speed was selected to promote more precise and controlled filament deposition.

Table 4.3 – Printing speed W' and % deviation.

	300mm/min	600mm/min	900mm/min
W'	1.59mm	1.16mm	0.67mm
% Deviation	536%	364%	168%

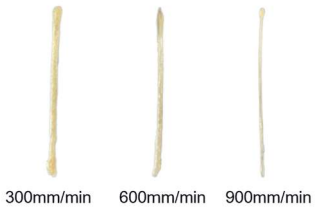

Figure 4.13 – Correlation between printing speed and filament thickness.

Following this test, the correlation between the angles incorporated into the design and the filament thickness at points of directional change was analyzed [Figure 4.14]. Among the evaluated geometries, the angle of 108°, corresponding to the external vertices of the star, yielded the most favorable results, with an average line width of 1.12 mm. This value is close to the line width of 0.90 mm defined for this design, indicating minimal deviation. In contrast, the 90° angle exhibited a broader line width of 1.36 mm, while the acute 36° angle, located at the internal vertices of the star, produced the greatest deviation, with a line width of 1.88 mm, approximately twice the original reference width. These results show that obtuse angles are more effective in maintaining dimensional fidelity to the design [143].

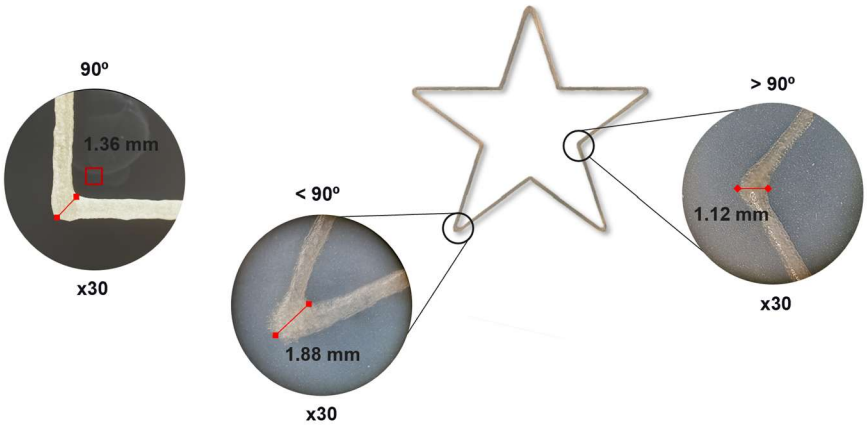

Figure 4.14 – Correlation between design angle and filament thickness.

Finally, the filament strand's resistance to collapse was tested, as illustrated in Figure 4.15. The filament successfully sustained itself at all tested distances, the farthest being 18 mm, without any observable deformation, sagging, or rupture, indicating excellent stability during extrusion and post-deposition. The maintenance of filament morphology suggests that the hydrogel possesses adequate yield stress and viscoelastic recovery to support its own weight before complete crosslinking [143]. It's possible to attribute a high print fidelity and self-supporting capability to this hydrogel, validating its suitability for complex 3D architectures that require precise deposition and dimensional stability.

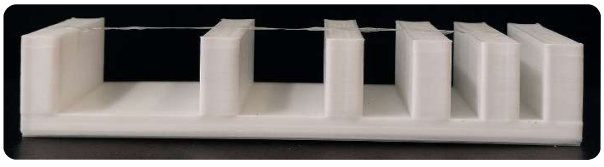

Figure 4.15 – Filament strand resistance to collapse at 3, 4, 6, 10, and 18mm.

After completing the optimization of the printing parameters, the conditions were established to enable the 3D printing of scaffolds for each hydrogel [Figure 4.16].

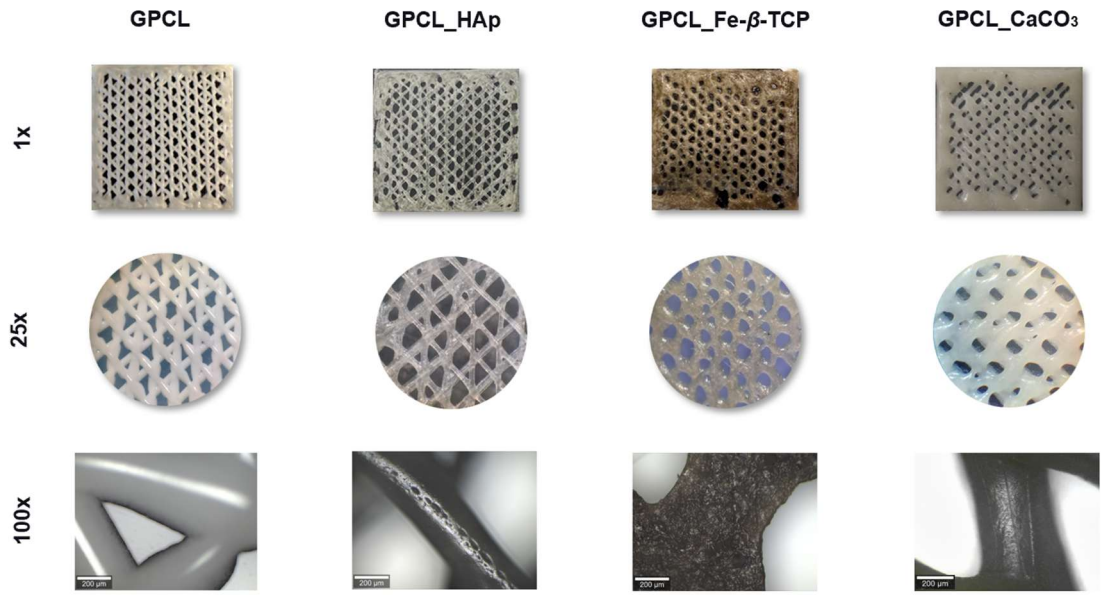

Figure 4.16 – 3D Printed scaffolds for each hydrogel at 1x, 25x, and 100x magnification.

Observing the scaffolds with the magnification of 1x, all 3D structures exhibit a successful reproduction of the designed layered pattern, indicating satisfactory printability and stability during the extrusion-based fabrication process. The GPCL scaffold displays the most regular and homogeneous architecture, characterized by well-defined pores arranged in a consistent pattern, with uniform strand thicknesses. The estimated pore size for GPCL is relatively large and evenly distributed, reflecting the polymer's optimal viscosity and flow behavior during printing. In contrast, the GPCL_HAp scaffold exhibits slightly reduced pore uniformity and a coarser texture, attributed to hydrogel heterogeneities during deposition. GPCL_Fe-*β*-TCP presents a darker coloration, with smaller and less distinct layers and pores. The GPCL_$CaCO_3$ scaffold retains the overall design and has well-defined layers, but presents over gelation at the pore edges.

At 25× magnification, these differences become more evident. The GPCL scaffold maintains smooth and continuous filament surfaces with clearly defined pore boundaries, confirming high structural fidelity. GPCL_HAp reveals visible granularity across the strand surfaces, indicating the uniform incorporation of hydroxyapatite within the polymeric matrix, which contributes to a rougher microtexture that could enhance cell adhesion. GPCL_Fe-*β*-TCP, on the other hand, presents noticeable irregularities and localized dark regions, consistent with the presence of NP agglomerates. GPCL_$CaCO_3$ exhibits a smooth strand surface and reduced definition of pores.

Microscopic observations at 100× magnification further reveal distinctions in strand width and surface roughness. GPCL and GPCL_$CaCO_3$ filaments exhibit a smooth, homogeneous surface with minimal microdefects, confirming uniform extrusion and solidification. GPCL_HAp strands display a moderately rough texture, with small defects along the filament surface. The GPCL_Fe-*β*-TCP scaffold,

in contrast, shows a highly irregular surface with evident porosity and microcavities along the strand walls.

Additionally, it was observed that both GPCL and GPCL_$CaCO_3$ 3D structures exhibited noticeable changes in appearance after 7 days of drying, as shown in Figure 4.17. Immediately after printing, the membranes appeared translucent and glossy; however, after 7 days of drying, the 3D structures became opaque and displayed a more flexible structure compared with GPCL_HAp and GPCL_Fe-*β*-TCP. This visual transition suggests a possible structural rearrangement within the polymer network. The incorporation of $CaCO_3$ may have further influenced this behavior by enhancing matrix densification and reducing the chloroform content during the drying process.

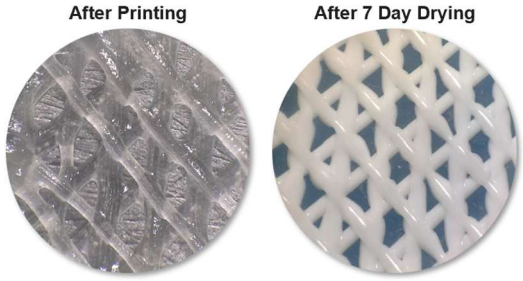

Figure 4.17 – 3D scaffolds for GPCL at 25x magnification, after printing and after 7-day drying.

To further visualize the internal architecture and pore distribution of the hydrogel scaffolds, MicroCT analysis was performed [Figure 4.18]. GPCL control 3D structure exhibits a uniform and orderly pore structure with clearly interconnected channels, as observed in both top and cross-sectional views, with most pores falling within the 500–1000 μm range. The regular stacking pattern and consistent pore morphology indicate a homogeneous gelation process.

Upon the HAp incorporation, the 3D structures display a more compact and less interconnected structure, implying that the HAp may act as nucleation sites during gelation, restricting polymer mobility [144]. This densification could contribute to enhanced mechanical resistance but may simultaneously reduce permeability and hinder efficient nutrient exchange. In contrast, the GPCL_Fe-*β*-TCP membrane exhibits a markedly different microarchitecture, characterized by larger and more irregular pores. The MicroCT reveals both large interconnected cavities and smaller, enclosed pores, reflecting a heterogeneous pore distribution. The color mapping confirms the presence of wide size variability, extending beyond 600 μm, which may result from uneven gelation dynamics.

GPCL_$CaCO_3$ demonstrates the most distinct vertical porosity gradient among all formulations. The full-volume analysis yields a mean pore size of 579.77 ± 383.56 μm, whereas considering only the upper section reduces the mean to 349.68 ± 238.74 μm. This discrepancy indicates that the $CaCO_3$ promotes a nonuniform internal structure, possibly due to particle sedimentation or differential cross-linking density during the curing process.

Comparing all 3D structures, it is evident that the inclusion of NPs affects both the scale and uniformity of porosity in the GPCL-based hydrogels. GPCL maintains the most regular morphology,

while the addition of HAp leads to smaller, denser pores. Fe-*β*-TCP increases pore size variability and overall heterogeneity, and $CaCO_3$ introduces pronounced spatial gradients.

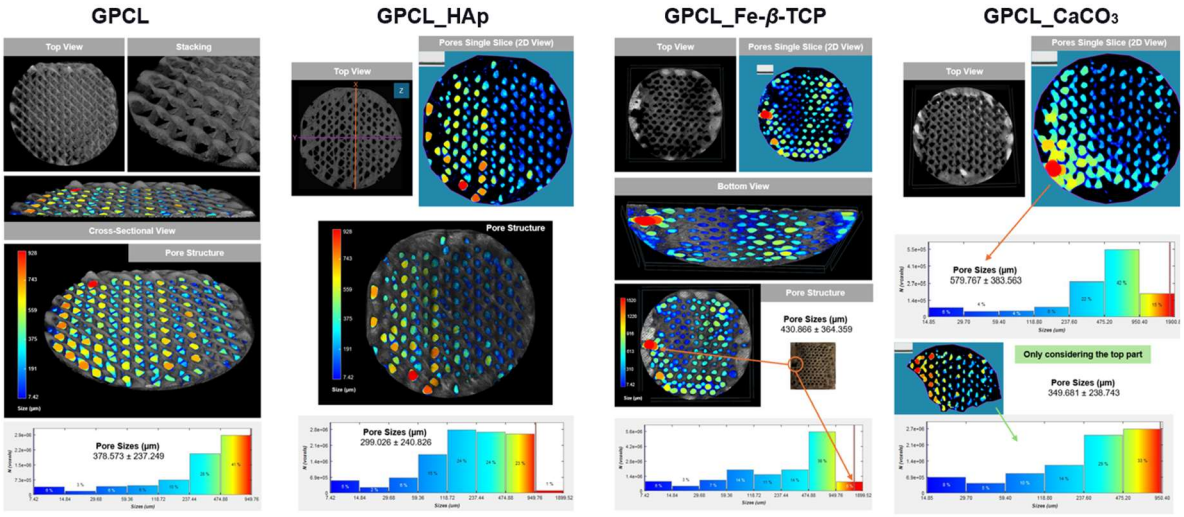

Figure 4.18 – MicroCT of hydrogel membranes.

The SEM analysis [Figure 4.19] provides additional insight into how the nanoscale surface organization reflects the structural behavior previously detected by MicroCT and macro and micrography. The GPCL scaffold displays well-defined and continuous filament surfaces, confirming that its high macroscopic homogeneity is accompanied by a stable microarchitecture with minimal defects along the strand walls. The incorporation of HAp visibly alters the polymer network, producing a rougher and more granular surface coating the filaments. It is also possible to observe agglomerates of particles throughout the membrane. GPCL_Fe-*β*-TCP reveals irregular depressions and microvoids dispersed across the surface, reinforcing the notion of heterogeneous pore development and uneven filament deposition and gelation dynamics, previously evidenced by the broader pore size variability in MicroCT.

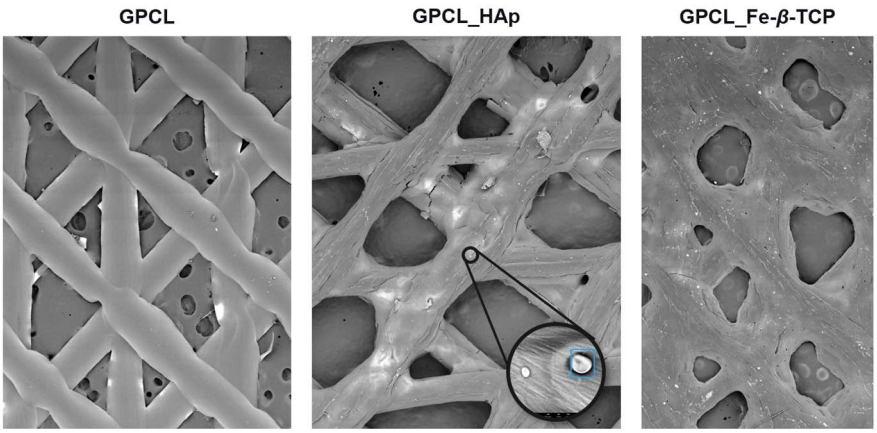

Figure 4.19 – Area overview of hydrogel 3D printed membranes, obtained through SEM.

Finally, a preliminary degradation test was carried out in cell culture medium to evaluate the structural stability of the different 3D-printed hydrogel structures. As shown in Figure 4.20, the GPCL, GPCL_HAp, and GPCL_Fe-*β*-TCP formulations began to lose their stability shortly after immersion,

showing immediate significant disintegration and complete degradation after one hour. In contrast, the GPCL_$CaCO_3$ construct maintained its original geometry during the entire test period, indicating markedly higher resistance and inertia to the cell culture medium. This result further demonstrates that the incorporation of $CaCO_3$ provided enhanced structural stability in the cell culture environment, as previously observed in the SBF tests, making the GPCL_$CaCO_3$ formulation the only 3D structure suitable for subsequent direct biological evaluation.

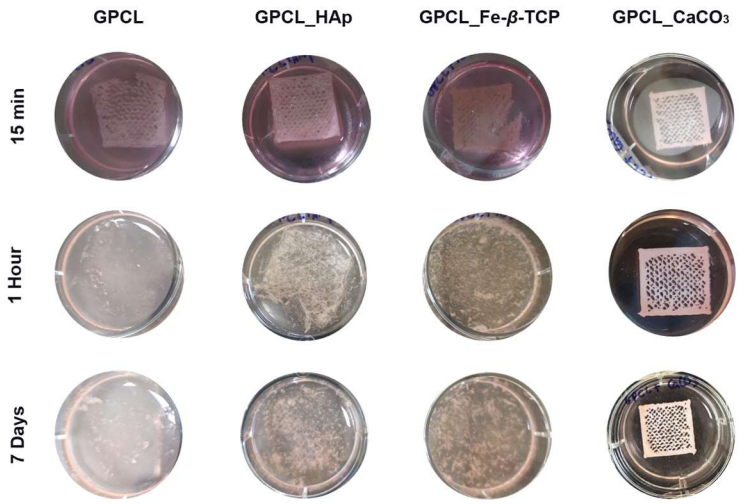

Figure 4.20 – Degradation assessment of hydrogel 3D printed membranes in cell culture medium, after 15 minutes, 1 hour, and 7 days.

4.3.3. Biological characterization

MG63 osteoblastic cells were exposed to the membrane extracts at concentrations of 5% and 10%. Results for 1-day exposure are presented in Figure 4.21. Compared to the control (absence of the extracts), the extracts from GPCL_HAp and GPCL_$CaCO_3$ membranes did not cause deleterious effects, whereas the extracts from the GPCL_Fe-*β*-TCP membrane decreased the metabolic activity (about 25% reduction). The extracts from the GPCL membrane were cytotoxic, especially at a dilution of 10%.

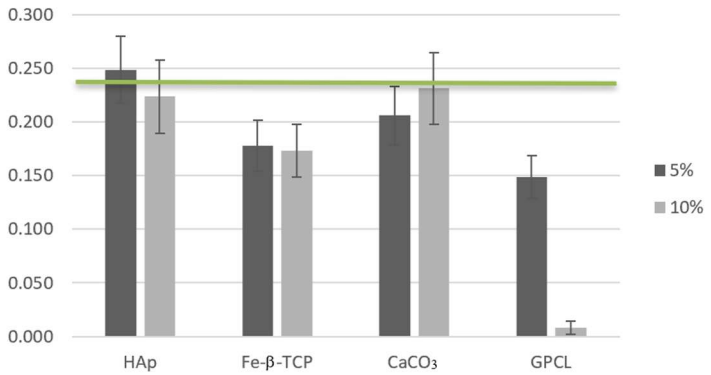

Figure 4.21 – MTT assay of MG63 cultured in the presence of the membranes' extracts, for 1 day.

In the direct assay, cells cultured over the GPCL_$CaCO_3$ membrane maintained the viability/metabolic activity, as exemplified in the cultured membrane for 1 day after reduction of the MTT to a bluish purple formazan product, as illustrated in Figure 4.22.

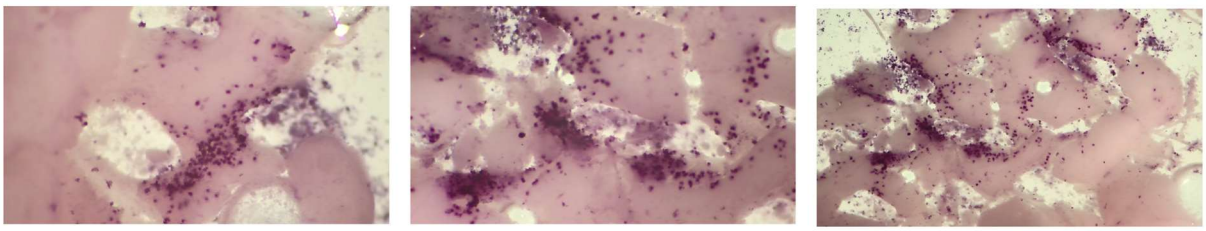

Figure 4.22 – Metabolic activity (MTT assay) of MG63 osteoblastic cells cultured over the GPCL_$CaCO_3$ membrane, for 1 day. Optical microscopy images, x100.

4.4. Conclusion

This study successfully developed and optimized a series of GPCL hydrogels functionalized with inorganic NPs for potential application in regenerative periodontal therapy. By combining the biocompatibility and bioactivity of gelatin with the mechanical stability and resistance to degradation of PCL, the resulting composites exhibited significant improvements in structural integrity compared with conventional gelatin-based hydrogels, maintaining the good printability.

Through physicochemical and structural characterization, it was demonstrated that the inclusion of NPs significantly influenced the hydrogels' rheological behavior, wettability, and degradation kinetics. Among the tested formulations, the GPCL_$CaCO_3$ hydrogel exhibited superior performance, combining high structural stability and moderate swelling. The strong interactions between $CaCO_3$ and the polymeric matrix, confirmed by ATR-FTIR analysis, were directly linked to its enhanced mechanical and morphological properties.

The extrusion-based 3D printing trials confirmed that all formulations were printable, with the GPCL_$CaCO_3$ scaffold also showing exceptional resistance in simulated body fluid and cell culture medium, maintaining its geometry far longer than other variants, making it the most promising candidate for subsequent biological testing.

In conclusion, this work contributes to the advancement of functionalized hydrogel design for tissue engineering by establishing the processing, compositional, and structural parameters necessary for achieving printable, biocompatible, and stable scaffolds tailored for periodontal regeneration. Future studies should further investigate the influence of NP concentration on structural integrity and degradation resistance, alongside comprehensive *in vitro* and *in vivo* biological assessments to validate the osteoconductive and regenerative potential of the GPCL_$CaCO_3$ formulation, paving the way for its translation into clinical periodontal applications.

Chapter 5
Conclusion

This dissertation presented the design and fabrication of gelatin-PCL hydrogels functionalized with inorganic NPs for application in periodontal tissue regeneration.

The first part presented the novel approach to the synthesis of three Ca-based NPs, engineered to provide osteoinductive functionalities. The results confirmed successful crystallization, distinct morphological architectures, laying the groundwork for their incorporation into hydrogel matrices. The second part built on these findings by developing composite hydrogels formed from gelatin and PCL, followed by extensive characterization, rheological analyses, degradation assays, and extrusion-based 3D printing. The study revealed that the NPs significantly influenced the performance of the hydrogels, particularly in terms of stability, printability, and morphology. Among all formulations, the GPCL_$CaCO_3$ hydrogel consistently stood out, exhibiting superior enduring in physiological conditions, thereby positioning itself as the leading candidate for further biological evaluation.

Collectively, the results demonstrate that combining gelatin with PCL and selected inorganic NPs provides a promising platform for developing bioactive and highly printable hydrogels suited for periodontal regeneration.

Although this dissertation establishes a solid foundation for the development of functionalized hydrogel membranes, several paths remain open for future investigation. Upcoming studies should start by studying the influence of particle concentration in the hydrogel matrix in terms of maintaining the improved resistance to degradation, as well as the incorporation of $CaCO_3$ NPs into the other GPCL_NP hydrogels, followed by comprehensive *in vitro* evaluations, including cytocompatibility, osteogenic differentiation, cell adhesion, and assessments under conditions that mimic the periodontal microenvironment.

Furthermore, degradation studies in enzyme-rich and inflammatory media would provide a more accurate prediction of scaffold behavior *in vivo*, while mechanical testing under cyclic loading could offer deeper insights into long-term durability within the oral cavity. Additionally, incorporating controlled-release strategies for antimicrobial, anti-inflammatory agents represents a promising direction to further enhance the therapeutic potential of these 3D structures. Finally, integrating imaging-based modelling into the fabrication of the design may enable the production of patient-specific scaffolds tailored to the unique geometry of periodontal defects, thereby improving fit, retention, and regenerative outcomes.

In conclusion, this dissertation provides a contribution to the improvement in the engineering of gelatine hydrogels and NP-enhanced 3D structures for periodontal tissue regeneration. The findings establish a foundation upon which future research can build toward the development of clinically viable, patient-specific regenerative solutions.

References

[1] A. Łasica, P. Golec, A. Laskus, M. Zalewska, M. Gędaj, and M. Popowska, “Periodontitis: etiology, conventional treatments, and emerging bacteriophage and predatory bacteria therapies,” *Front Microbiol*, vol. 15, Sep. 2024, doi: 10.3389/fmicb.2024.1469414.

[2] D. Trindade, R. Carvalho, V. Machado, L. Chambrone, J. J. Mendes, and J. Botelho, “Prevalence of periodontitis in dentate people between 2011 and 2020: A systematic review and meta-analysis of epidemiological studies,” *J Clin Periodontol*, vol. 50, no. 5, pp. 604–626, May 2023, doi: 10.1111/jcpe.13769.

[3] D. F. Kinane, P. G. Stathopoulou, and P. N. Papapanou, “Periodontal diseases,” *Nat Rev Dis Primers*, vol. 3, no. 1, p. 17038, Jun. 2017, doi: 10.1038/nrdp.2017.38.

[4] T. Kwon, I. B. Lamster, and L. Levin, “Current Concepts in the Management of Periodontitis,” *Int Dent J*, vol. 71, no. 6, pp. 462–476, Dec. 2021, doi: 10.1111/idj.12630.

[5] G. Hajishengallis and R. J. Lamont, “Polymicrobial communities in periodontal disease: Their quasi-organismal nature and dialogue with the host,” *Periodontol 2000*, vol. 86, no. 1, pp. 210–230, Jun. 2021, doi: 10.1111/prd.12371.

[6] G. V. O. Fernandes, G. A. Mosley, W. Ross, A. Dagher, B. G. dos S. Martins, and J. C. H. Fernandes, “Revisiting Socransky’s Complexes: A Review Suggesting Updated New Bacterial Clusters (GF-MoR Complexes) for Periodontal and Peri-Implant Diseases and Conditions,” *Microorganisms*, vol. 12, no. 11, p. 2214, Oct. 2024, doi: 10.3390/microorganisms12112214.

[7] M. M. Haque, K. Yerex, A. Kelekis-Cholakis, and K. Duan, “Advances in novel therapeutic approaches for periodontal diseases,” *BMC Oral Health*, vol. 22, no. 1, p. 492, Nov. 2022, doi: 10.1186/s12903-022-02530-6.

[8] J. Zhou, wen lei Wu, and Y. Liu, “Research progress of hydrogel therapy to improve hypoxic environment of periodontal tissues and promote periodontal regeneration,” *J Oral Biol Craniofac Res*, vol. 15, no. 4, pp. 869–879, Jul. 2025, doi: 10.1016/j.jobcr.2025.06.005.

[9] A. M. Diez-Pascual and A. Rahdar, “Functional Nanomaterials in Biomedicine: Current Uses and Potential Applications,” *ChemMedChem*, vol. 17, no. 16, Aug. 2022, doi: 10.1002/cmdc.202200142.

[10] D. Wang, Q. Li, C. Xiao, H. Wang, and S. Dong, “Nanoparticles in Periodontitis Therapy: A Review of the Current Situation,” *Int J Nanomedicine*, vol. Volume 19, pp. 6857–6893, Jul. 2024, doi: 10.2147/IJN.S465089.

[11] M. Y. Shaheen, “Nanocrystalline hydroxyapatite in periodontal bone regeneration: A systematic review,” *Saudi Dent J*, vol. 34, no. 8, pp. 647–660, Dec. 2022, doi: 10.1016/j.sdentj.2022.09.005.

[12] C. Qiu *et al.*, “Preparation and application of calcium phosphate nanocarriers in drug delivery,” *Mater Today Bio*, vol. 17, p. 100501, Dec. 2022, doi: 10.1016/j.mtbio.2022.100501.

[13] X. Chen, J. Bi, H. Zhang, M. Yuan, J. Wang, and N. Hu, “NIR-responsive CaCO3@ BMP-2/PDA nanocomposite for multifunctional therapy in periodontitis,” *Colloids Surf A Physicochem Eng Asp*, vol. 713, p. 136520, May 2025, doi: 10.1016/j.colsurfa.2025.136520.

[14] X. Hou *et al.*, “Calcium Phosphate-Based Biomaterials for Bone Repair,” *J Funct Biomater*, vol.

13, no. 4, p. 187, Oct. 2022, doi: 10.3390/jfb13040187.

[15] I. Lodoso-Torrecilla, J. J. J. P. van den Beucken, and J. A. Jansen, “Calcium phosphate cements: Optimization toward biodegradability,” *Acta Biomater*, vol. 119, pp. 1–12, Jan. 2021, doi: 10.1016/j.actbio.2020.10.013.

[16] N. Eliaz and N. Metoki, “Calcium Phosphate Bioceramics: A Review of Their History, Structure, Properties, Coating Technologies and Biomedical Applications,” *Materials*, vol. 10, no. 4, p. 334, Mar. 2017, doi: 10.3390/ma10040334.

[17] L. Wu *et al.*, “3D-printed HAp bone regeneration scaffolds enable nano-scale manipulation of cellular mechanotransduction signals,” *Chemical Engineering Journal*, vol. 455, p. 140699, Jan. 2023, doi: 10.1016/j.cej.2022.140699.

[18] M. Montesissa, V. Tommasini, K. Rubini, M. Boi, N. Baldini, and E. Boanini, “State of Art and Perspective of Calcium Phosphate-Based Coatings Coupled with Bioactive Compounds for Orthopedic Applications,” *Nanomaterials*, vol. 15, no. 15, p. 1199, Aug. 2025, doi: 10.3390/nano15151199.

[19] V. Saxena, I. Shukla, and L. M. Pandey, “Hydroxyapatite: an inorganic ceramic for biomedical applications,” in *Materials for Biomedical Engineering*, Elsevier, 2019, pp. 205–249. doi: 10.1016/B978-0-12-816909-4.00008-7.

[20] A.-M. Zhang, P. Lenin, R.-C. Zeng, and M. B. Kannan, “Advances in hydroxyapatite coatings on biodegradable magnesium and its alloys,” *Journal of Magnesium and Alloys*, vol. 10, no. 5, pp. 1154–1170, May 2022, doi: 10.1016/j.jma.2022.01.001.

[21] S. Mondal and U. Pal, “3D hydroxyapatite scaffold for bone regeneration and local drug delivery applications,” *J Drug Deliv Sci Technol*, vol. 53, p. 101131, Oct. 2019, doi: 10.1016/j.jddst.2019.101131.

[22] S. Lara-Ochoa, W. Ortega-Lara, and C. E. Guerrero-Beltrán, “Hydroxyapatite Nanoparticles in Drug Delivery: Physicochemistry and Applications,” *Pharmaceutics*, vol. 13, no. 10, p. 1642, Oct. 2021, doi: 10.3390/pharmaceutics13101642.

[23] P. Szterner, A. Antosik, J. Pagacz, and P. Tymowicz-Grzyb, “Morphology Control of Hydroxyapatite as a Potential Reinforcement for Orthopedic Biomaterials: The Hydrothermal Process,” *Crystals (Basel)*, vol. 13, no. 5, p. 793, May 2023, doi: 10.3390/cryst13050793.

[24] G. Karunakaran *et al.*, “Citric Acid-Mediated Microwave-Hydrothermal Synthesis of Mesoporous F-Doped HAp Nanorods from Bio-Waste for Biocidal Implant Applications,” *Nanomaterials*, vol. 12, no. 3, p. 315, Jan. 2022, doi: 10.3390/nano12030315.

[25] S. Liao *et al.*, “A three-layered nano-carbonated hydroxyapatite/collagen/PLGA composite membrane for guided tissue regeneration,” *Biomaterials*, vol. 26, no. 36, pp. 7564–7571, Dec. 2005, doi: 10.1016/j.biomaterials.2005.05.050.

[26] S. Tamburaci, “Development of Si doped nano hydroxyapatite reinforced bilayer chitosan nanocomposite barrier membranes for guided bone regeneration,” *Materials Science and Engineering: C*, vol. 128, p. 112298, Sep. 2021.

[27] X. Niu *et al.*, “Electrospun polyamide-6/chitosan nanofibers reinforced nano-hydroxyapatite/polyamide-6 composite bilayered membranes for guided bone regeneration,”

Carbohydr Polym, vol. 260, p. 117769, May 2021, doi: 10.1016/j.carbpol.2021.117769.

[28] K. Baskar *et al.*, “Eggshell derived nano-hydroxyapatite incorporated carboxymethyl chitosan scaffold for dentine regeneration: A laboratory investigation,” *Int Endod J*, vol. 55, no. 1, pp. 89–102, Jan. 2022, doi: 10.1111/iej.13644.

[29] Ü. Çayır Bozoğlu, A. Kiremitçi, M. Ç. Yurtsever, and M. Gümüşderelioğlu, “Peek dental implants coated with boron-doped nano-hydroxyapatites: Investigation of in-vitro osteogenic activity,” *Journal of Trace Elements in Medicine and Biology*, vol. 73, p. 127026, Sep. 2022, doi: 10.1016/j.jtemb.2022.127026.

[30] C.-H. Fang *et al.*, “Metformin-Incorporated Gelatin/Nano-Hydroxyapatite Scaffolds Promotes Bone Regeneration in Critical Size Rat Alveolar Bone Defect Model,” *Int J Mol Sci*, vol. 23, no. 1, p. 558, Jan. 2022, doi: 10.3390/ijms23010558.

[31] H. Chaair, H. Labjar, and O. Britel, “Synthesis of β-tricalcium phosphate,” *Morphologie*, vol. 101, no. 334, pp. 120–124, Sep. 2017, doi: 10.1016/j.morpho.2017.06.002.

[32] R. Cuscó, F. Guitián, S. de Aza, and L. Artús, “Differentiation between hydroxyapatite and β-tricalcium phosphate by means of μ-Raman spectroscopy,” *J Eur Ceram Soc*, vol. 18, no. 9, pp. 1301–1305, Jan. 1998, doi: 10.1016/S0955-2219(98)00057-0.

[33] K. Matsunaga, T. Kubota, K. Toyoura, and A. Nakamura, “First-principles calculations of divalent substitution of Ca2+ in tricalcium phosphates,” *Acta Biomater*, vol. 23, pp. 329–337, Sep. 2015, doi: 10.1016/j.actbio.2015.05.014.

[34] M. Bohner, B. L. G. Santoni, and N. Döbelin, “β-tricalcium phosphate for bone substitution: Synthesis and properties,” *Acta Biomater*, vol. 113, pp. 23–41, Sep. 2020, doi: 10.1016/j.actbio.2020.06.022.

[35] I. O. Oladele, S. A. Adekola, N. I. Agbeboh, B. A. Isola-Makinde, and B. O. Adewuyi, “Synthesis and Application of Sustainable Tricalcium Phosphate Based Biomaterials From Agro-Based Materials: A Review,” *Biomed Eng Comput Biol*, vol. 15, Jan. 2024, doi: 10.1177/11795972241293525.

[36] T. Wojcik, F. Chai, V. Hornez, G. Raoul, and J.-C. Hornez, “Engineering Precise Interconnected Porosity in β-Tricalcium Phosphate (β-TCP) Matrices by Means of Top–Down Digital Light Processing,” *Biomedicines*, vol. 12, no. 4, p. 736, Mar. 2024, doi: 10.3390/biomedicines12040736.

[37] S. Vahabzadeh and S. Bose, “Effects of Iron on Physical and Mechanical Properties, and Osteoblast Cell Interaction in β-Tricalcium Phosphate,” *Ann Biomed Eng*, vol. 45, no. 3, pp. 819–828, Mar. 2017, doi: 10.1007/s10439-016-1724-1.

[38] S. L. O. Costa, P. F. Silva, G. K. G. Carvalho, Y. B. A. Almeida, J. R. S. Farias, and A. S. N. Braga, “A brief review of beta tricalcium phosphate (β -TCP) doped with metal ions. ,” *American Journal of Engineering Research (AJER)* , vol. 10, no. 8, pp. 333–344, 2021.

[39] L. Duta, G. Dorcioman, and V. Grumezescu, “A Review on Biphasic Calcium Phosphate Materials Derived from Fish Discards,” *Nanomaterials*, vol. 11, no. 11, p. 2856, Oct. 2021, doi: 10.3390/nano11112856.

[40] A. Susanto, B. C. Prasetyo, and G. W. Norisma, “Use of bone graft alloplast β-tricalcium

phosphate in regenerative periodontal surgery treatment: A systematic review," *Journal of International Oral Health*, vol. 16, no. 1, pp. 42–49, Jan. 2024, doi: 10.4103/jioh.jioh_137_23.

[41] R. Bansal, S. Patil, K. Chaubey, R. Thakur, and P. Goyel, "Clinical evaluation of hydroxyapatite and β-tricalcium phosphate composite graft in the treatment of intrabony periodontal defect: A clinico-radiographic study," *J Indian Soc Periodontol*, vol. 18, no. 5, p. 610, 2014, doi: 10.4103/0972-124X.142455.

[42] N. Tan, M. Sabalic-Schoener, L. Nguyen, and F. D'Aiuto, "β-Tricalcium Phosphate-Loaded Chitosan-Based Thermosensitive Hydrogel for Periodontal Regeneration," *Polymers (Basel)*, vol. 15, no. 20, p. 4146, Oct. 2023, doi: 10.3390/polym15204146.

[43] H. Lu *et al.*, "Current Application of Beta-Tricalcium Phosphate in Bone Repair and Its Mechanism to Regulate Osteogenesis," *Front Mater*, vol. 8, Jul. 2021, doi: 10.3389/fmats.2021.698915.

[44] Y.-Q. Niu *et al.*, "Calcium carbonate: controlled synthesis, surface functionalization, and nanostructured materials," *Chem Soc Rev*, vol. 51, no. 18, pp. 7883–7943, 2022, doi: 10.1039/D1CS00519G.

[45] P. Fadia *et al.*, "Calcium carbonate nano- and microparticles: synthesis methods and biological applications," *3 Biotech*, vol. 11, no. 11, p. 457, Nov. 2021, doi: 10.1007/s13205-021-02995-2.

[46] R. Babou-Kammoe, S. Hamoudi, F. Larachi, and K. Belkacemi, "Synthesis of $CaCO_3$ nanoparticles by controlled precipitation of saturated carbonate and calcium nitrate aqueous solutions," *Can J Chem Eng*, vol. 90, no. 1, pp. 26–33, Feb. 2012, doi: 10.1002/cjce.20673.

[47] B. Tang *et al.*, "Preparation and properties of monodisperse nano-CaCO3 powders," *Journal of Nanoparticle Research*, vol. 27, no. 4, p. 83, Apr. 2025, doi: 10.1007/s11051-025-06279-1.

[48] M. Mateescu, S. M. Doncea, I. Chican, C. L. Nistor, and I. C. Bujanca, "Synthesis of Calcium Carbonate Micro Particles using Emulsion Membrane Process Applied for Drug Release Studies," *Revista de Chimie*, vol. 68, no. 10, pp. 2320–2324, Nov. 2017, doi: 10.37358/RC.17.10.5877.

[49] M. Radune, S. Lugovskoy, Y. Knop, and A. Yankelevitch, "Use of Taguchi method for high energy ball milling of CaCO3," *International Journal of Mechanical and Materials Engineering*, vol. 17, no. 1, p. 1, Dec. 2022, doi: 10.1186/s40712-021-00140-8.

[50] C. A. Weiss *et al.*, "Inluence of Temperature on Calcium Carbonate Polymorph formed from Ammonium Carbonate and Calcium Acetate," *J Nanotech Smart Mater*, vol. 1, pp. 1–6, 2014.

[51] R. Salomão, L. M. M. Costa, and G. M. de Olyveira, "Precipitated Calcium Carbonate Nano-Microparticles: Applications in Drug Delivery," *Advances in Tissue Engineering & Regenerative Medicine: Open Access*, vol. 3, no. 2, Nov. 2017, doi: 10.15406/atroa.2017.03.00059.

[52] Y. F. Ma, Y. H. Gao, and Q. L. Feng, "Effects of pH and temperature on CaCO3 crystallization in aqueous solution with water soluble matrix of pearls," *J Cryst Growth*, vol. 312, no. 21, pp. 3165–3170, Oct. 2010, doi: 10.1016/j.jcrysgro.2010.07.053.

[53] A. Korchef, "Effect of Operating Parameters and Foreign Ions on the Crystal Growth of Calcium Carbonate during Scale Formation: An Overview," in *Crystallization and Applications*, IntechOpen, 2022. doi: 10.5772/intechopen.94121.

[54] A. Yu. Tikhonov, S. K. Myasnikov, and N. N. Kulov, “Kinetics of Nucleation and Growth of Calcium Carbonate and Calcium Sulphate Crystals from Aqueous Solutions,” *Theoretical Foundations of Chemical Engineering*, vol. 54, no. 4, pp. 529–538, Jul. 2020, doi: 10.1134/S0040579520030124.

[55] K. Koo, G. Polimeni, M. Qahash, C. K. Kim, and U. M. Wikesjö, “Periodontal repair in dogs: guided tissue regeneration enhances bone formation in sites implanted with a coral-derived calcium carbonate biomaterial,” *J Clin Periodontol*, vol. 32, no. 1, pp. 104–110, Jan. 2005, doi: 10.1111/j.1600-051X.2004.00632.x.

[56] S. Dizaj, M. Barzegar-Jalali, M. Zarrintan, K. Adibkia, and F. Lotfipour, “Calcium Carbonate Nanoparticles; Potential in Bone and Tooth Disorders,” *Pharmaceutical Sciences*, pp. 175–182, Mar. 2015.

[57] M. Abedi, Y. Ghasemi, and M. M. Nemati, “Nanotechnology in toothpaste: Fundamentals, trends, and safety,” *Heliyon*, vol. 10, no. 3, p. e24949, Feb. 2024, doi: 10.1016/j.heliyon.2024.e24949.

[58] S. N. Kabekkodu, A. Dosen, and T. N. Blanton, “PDF-5+: a comprehensive Powder Diffraction File™ for materials characterization,” *Powder Diffr*, vol. 39, no. 2, pp. 47–59, Jun. 2024, doi: 10.1017/S0885715624000150.

[59] S. Saroj and U. Vijayalakshmi, “Structural, morphological and biological assessment of magnetic hydroxyapatite with superior hyperthermia potential for orthopedic applications,” *Sci Rep*, vol. 15, no. 1, p. 3234, Jan. 2025, doi: 10.1038/s41598-025-87111-7.

[60] S. Srividya, T. P. Sastry, J. D., and S. N., “SYNTHESIS AND CHARACTERIZATION OF A NOVEL BONE GRAFT MATERIAL CONTAINING BIPHASIC CALCIUM PHOSPHATE AND CHITOSAN FORTIFIED WITH ALOE VERA,” *International Journal of Drug Regulatory Affairs*, vol. 2, no. 2, pp. 85–90, Feb. 2018, doi: 10.22270/ijdra.v2i2.134.

[61] E. Bouyer, F. Gitzhofer, and M. I. Boulos, “Morphological study of hydroxyapatite nanocrystal suspension,” *J Mater Sci Mater Med*, vol. 11, no. 8, pp. 523–531, Aug. 2000, doi: 10.1023/A:1008918110156.

[62] A. Bertoluzza, G. Bottura, M. A. Morelli, P. Taddei, and A. Tinti, “Vibrational Spectroscopy of Calcium Phosphate Bioactive Coatings,” in *Spectroscopy of Biological Molecules: Modern Trends*, Dordrecht: Springer Netherlands, 1997, pp. 425–428. doi: 10.1007/978-94-011-5622-6_190.

[63] L. Xie *et al.*, “Fe/Zn-modified tricalcium phosphate (TCP) biomaterials: preparation and biological properties,” *RSC Adv*, vol. 9, no. 2, pp. 781–789, 2019, doi: 10.1039/C8RA08453J.

[64] R. L. Frost, Y. Xi, R. Scholz, A. López, and F. M. Belotti, “Vibrational spectroscopic characterization of the phosphate mineral hureaulite – (Mn, Fe)5(PO4)2(HPO4)2·4(H2O),” *Vib Spectrosc*, vol. 66, pp. 69–75, May 2013, doi: 10.1016/j.vibspec.2013.02.003.

[65] H. L. Jang *et al.*, “In Vitro and In Vivo Evaluation of Whitlockite Biocompatibility: Comparative Study with Hydroxyapatite and *β* -Tricalcium Phosphate,” *Adv Healthc Mater*, vol. 5, no. 1, pp. 128–136, Jan. 2016, doi: 10.1002/adhm.201400824.

[66] P. Somasundaran, “Zeta potential of apatite in aqueous solutions and its change during equilibration,” *J Colloid Interface Sci*, vol. 27, no. 4, pp. 659–666, Aug. 1968, doi: 10.1016/0021-

9797(68)90098-2.

[67] E. SKWAREK and W. JANUSZ, “The Influence of Carbonate Ions on the Structure of the Electrical Double Layer at the Interface of Hydroxyapatite/Electrolyte Solution,” *Materials Science*, vol. 22, no. 2, May 2016, doi: 10.5755/j01.ms.22.2.7817.

[68] M. Jamil, F. Abida, Z. Hatim, M. Elassfouri, and E. Gourri, “Effects of ions traces on the dissolution of bioceramics composed of hydroxyapatite and Î²-tricalcium phosphate,” *Mediterranean Journal of Chemistry*, vol. 4, no. 1, pp. 51–58, Feb. 2015, doi: 10.13171/mjc.4.1.2015.14.03.14.15/jamil.

[69] C. M. Botelho, M. A. Lopes, I. R. Gibson, S. M. Best, and J. D. Santos, “Structural analysis of Si-substituted hydroxyapatite: zeta potential and X-ray photoelectron spectroscopy,” *J Mater Sci Mater Med*, vol. 13, no. 12, pp. 1123–1127, Dec. 2002, doi: 10.1023/A:1021177601899.

[70] C. Rani and S. D. Tiwari, “Temperature variation of surface magnetization in antiferromagnetic six lines ferrihydrite nanoparticles,” *J Magn Magn Mater*, vol. 587, p. 171341, Dec. 2023, doi: 10.1016/j.jmmm.2023.171341.

[71] T. S. S. Carvalho *et al.*, “Magnetic and thermo-responsive microparticles based on calcium phosphates with high potential to produce structures for bone regeneration and local hyperthermia,” *Mater Res Bull*, vol. 185, p. 113274, May 2025, doi: 10.1016/j.materresbull.2024.113274.

[72] K.-H. Yoo, H. Kim, W. G. Sun, Y.-I. Kim, and S.-Y. Yoon, “Fe-doped tricalcium phosphates: crystal structure and degradation behavior,” *Mater Res Express*, vol. 7, no. 12, p. 125403, Dec. 2020, doi: 10.1088/2053-1591/abcee8.

[73] K. Yoshida *et al.*, “Substitution Model of Monovalent (Li, Na, and K), Divalent (Mg), and Trivalent (Al) Metal Ions for β-Tricalcium Phosphate,” *Journal of the American Ceramic Society*, vol. 89, no. 2, pp. 688–690, Feb. 2006, doi: 10.1111/j.1551-2916.2005.00727.x.

[74] K. Liu, X. Xie, J. Yan, S. Zhang, and H. Zhang, “An adsorption isotherm identification method based on CNN-LSTM neural network,” *J Mol Model*, vol. 29, no. 9, p. 301, Sep. 2023, doi: 10.1007/s00894-023-05704-3.

[75] H. S. Ningsih, L. Tannesia, T. Y. Animut, W.-L. Yeh, and S.-J. Shih, “Characterization of mesoporous in β-tricalcium phosphate using electron microscopy,” *Journal of the Australian Ceramic Society*, vol. 58, no. 5, pp. 1445–1454, Dec. 2022, doi: 10.1007/s41779-022-00781-8.

[76] M. A. Goldberg *et al.*, “Effects of Various Ripening Media on the Mesoporous Structure and Morphology of Hydroxyapatite Powders,” *Nanomaterials*, vol. 13, no. 3, p. 418, Jan. 2023, doi: 10.3390/nano13030418.

[77] A.-R. Ibrahim *et al.*, “Synthesis of Spongy-Like Mesoporous Hydroxyapatite from Raw Waste Eggshells for Enhanced Dissolution of Ibuprofen Loaded via Supercritical CO2,” *Int J Mol Sci*, vol. 16, no. 4, pp. 7960–7975, Apr. 2015, doi: 10.3390/ijms16047960.

[78] L. Xu *et al.*, “Pore Structure and Fractal Characteristics of Different Shale Lithofacies in the Dalong Formation in the Western Area of the Lower Yangtze Platform,” *Minerals*, vol. 10, no. 1, p. 72, Jan. 2020, doi: 10.3390/min10010072.

[79] M. U. Munir, S. Salman, A. Ihsan, and T. Elsaman, “Synthesis, Characterization,

Functionalization and Bio-Applications of Hydroxyapatite Nanomaterials: An Overview," *Int J Nanomedicine*, vol. Volume 17, pp. 1903–1925, May 2022, doi: 10.2147/IJN.S360670.

[80] C. Carmen, E. Andronescu, and D. Predoi, "BET and XRD studies on the hydroxyapatite and europium doped hydroxyapatite," *Dig J Nanomater Biostruct*, vol. 6, pp. 1239–1244, Jul. 2011.

[81] A. Fadli, "OPTIMISATION OF THE HYDROXYAPATITE SURFACE AREA PREPARED USING A POROGEN RUBBER SUSPENSION," *Ceramics - Silikaty*, pp. 371–378, Sep. 2023, doi: 10.13168/cs.2023.0037.

[82] Y.-B. Hu, M. Wolthers, D. A. Wolf-Gladrow, and G. Nehrke, "Effect of pH and Phosphate on Calcium Carbonate Polymorphs Precipitated at near-Freezing Temperature," *Cryst Growth Des*, vol. 15, no. 4, pp. 1596–1601, Apr. 2015, doi: 10.1021/cg500829p.

[83] D. Render *et al.*, "Biomaterial-Derived Calcium Carbonate Nanoparticles for Enteric Drug Delivery," *J Nanomater*, vol. 2016, pp. 1–8, 2016, doi: 10.1155/2016/3170248.

[84] U. Magdans, H. Gies, X. Torrelles, and J. Rius, "Investigation of the {104} surface of calcite under dry and humid atmospheric conditions with grazing incidence X-ray diffraction (GIXRD)," *European Journal of Mineralogy*, vol. 18, no. 1, pp. 83–92, Mar. 2006, doi: 10.1127/0935-1221/2006/0018-0083.

[85] C. Matei, D. Berger, A. Dumbrava, M. D. Radu, and E. Gheorghe, "Calcium carbonate as silver carrier in composite materials obtained in green seaweed extract with topical applications," *J Solgel Sci Technol*, vol. 93, no. 2, pp. 315–323, Feb. 2020, doi: 10.1007/s10971-019-05145-6.

[86] J. D. Rodriguez-Blanco, S. Shaw, and L. G. Benning, "The kinetics and mechanisms of amorphous calcium carbonate (ACC) crystallization to calcite, viavaterite.," *Nanoscale*, vol. 3, no. 1, pp. 265–271, 2011, doi: 10.1039/C0NR00589D.

[87] M. M. H. Al Omari, I. S. Rashid, N. A. Qinna, A. M. Jaber, and A. A. Badwan, "Calcium Carbonate," 2016, pp. 31–132. doi: 10.1016/bs.podrm.2015.11.003.

[88] P. Ranjane, M. Deshpande, and P. S. Kulkarni, "Various polymorphs of calcium carbonate and poly(ethylene) glycol as thermal energy storage materials," *J Appl Polym Sci*, vol. 140, no. 41, Nov. 2023, doi: 10.1002/app.54533.

[89] E. Coleman and A. Gupta, "pH-Dependent Zeta Potential Induces Diffusiophoretic Focusing in an Acid-Base Reaction," Jun. 2025, doi: https://doi.org/10.48550/arXiv.2506.05731.

[90] K. Song, J.-H. Bang, S.-C. Chae, J. Kim, and S.-W. Lee, "Phase and morphology of calcium carbonate precipitated by rapid mixing in the absence of additives," *RSC Adv*, vol. 12, no. 30, pp. 19340–19349, 2022, doi: 10.1039/D2RA03507C.

[91] L. Hołysz, M. Chibowski, and E. Chibowski, "Time-dependent changes of zeta potential and other parameters of in situ calcium carbonate due to magnetic field treatment," *Colloids Surf A Physicochem Eng Asp*, vol. 208, no. 1–3, pp. 231–240, Aug. 2002, doi: 10.1016/S0927-7757(02)00149-8.

[92] R. Ranjan, S. D. Narnaware, and N. V. Patil, "A Novel Technique for Synthesis of Calcium Carbonate Nanoparticles," *National Academy Science Letters*, vol. 41, no. 6, pp. 403–406, Dec. 2018, doi: 10.1007/s40009-018-0704-4.

[93] N. Zhang, B. Zhao, P. Yang, and H. Zhang, "Systematic Study of Preparing Porous CaCO3

Vaterite Particles for Controlled Drug Release," *Nanomaterials*, vol. 15, no. 16, p. 1227, Aug. 2025, doi: 10.3390/nano15161227.

[94] B. Zafar, J. Campbell, J. Cooke, A. G. Skirtach, and D. Volodkin, "Modification of Surfaces with Vaterite CaCO3 Particles," *Micromachines (Basel)*, vol. 13, no. 3, p. 473, Mar. 2022, doi: 10.3390/mi13030473.

[95] J. L. Platt, B. M. Ogle, J. A. Piedrahita, and M. Cascalho, "Organogenesis and related approaches for organ replacement," in *Living Donor Organ Transplantation*, Elsevier, 2024, pp. 1501–1520. doi: 10.1016/B978-0-443-23571-9.00049-9.

[96] D. N. Haymanali, "To What Extent Can Tissue Engineering and 3D Bioprinting Be Used to Create Functional and Vascularized Human Organs?," *Next Frontier For Life Sciences and AI*, vol. 8, no. 1, p. 31, Jul. 2024, doi: 10.62802/87vgra44.

[97] P. Agarwal, V. Mathur, M. Kasturi, V. Srinivasan, R. N. Seetharam, and K. S Vasanthan, "A Futuristic Development in 3D Printing Technique Using Nanomaterials with a Step Toward 4D Printing," *ACS Omega*, vol. 9, no. 36, pp. 37445–37458, Sep. 2024, doi: 10.1021/acsomega.4c04123.

[98] N. Sultana, A. Cole, and F. Strachan, "Biocomposite Scaffolds for Tissue Engineering: Materials, Fabrication Techniques and Future Directions," *Materials*, vol. 17, no. 22, p. 5577, Nov. 2024, doi: 10.3390/ma17225577.

[99] J. A. Park, Y. Lee, and S. Jung, "Inkjet-based bioprinting for tissue engineering," *Organoid*, vol. 3, p. e12, Aug. 2023, doi: 10.51335/organoid.2023.3.e12.

[100] R. D. Ventura, "An Overview of Laser-assisted Bioprinting (LAB) in Tissue Engineering Applications," *Medical Lasers*, vol. 10, no. 2, pp. 76–81, Jun. 2021, doi: 10.25289/ML.2021.10.2.76.

[101] J. Wang, C. Xu, S. Yang, L. Wang, and M. Xu, "Continuous and highly accurate multi-material extrusion-based bioprinting with optical coherence tomography imaging," *Int J Bioprint*, vol. 9, no. 3, p. 707, Mar. 2023, doi: 10.18063/ijb.707.

[102] A. S. Priya *et al.*, "Comprehensive Review of Hydrogel Synthesis, Characterization, and Emerging Applications," *Journal of Composites Science*, vol. 8, no. 11, p. 457, Nov. 2024, doi: 10.3390/jcs8110457.

[103] H. Choi, W.-S. Choi, and J.-O. Jeong, "A Review of Advanced Hydrogel Applications for Tissue Engineering and Drug Delivery Systems as Biomaterials," *Gels*, vol. 10, no. 11, p. 693, Oct. 2024, doi: 10.3390/gels10110693.

[104] D. Goder Orbach, O. Sharabani-Yosef, O. Hadad, and M. Zilberman, "Gelatin-Based Polymers Can Be Processed to Highly Resilient Biocompatible Porous Hydrogel Scaffolds for Soft Tissue Regeneration Applications," *Gels*, vol. 10, no. 11, p. 678, Oct. 2024, doi: 10.3390/gels10110678.

[105] Y. Yang, L. Mao, H. Chen, L. Ma, Y. Fu, and Y. Zhang, "The crosslinking sites and molecular conformation of gelatin hydrogel modified by transglutaminase," *Food Hydrocoll*, vol. 154, p. 110132, Sep. 2024, doi: 10.1016/j.foodhyd.2024.110132.

[106] Y. Lin, J. Lou, Y. Xia, and O. Chaudhuri, "Cross-Linker Architectures Impact Viscoelasticity in Dynamic Covalent Hydrogels," *Adv Healthc Mater*, vol. 13, no. 30, Dec. 2024, doi:

10.1002/adhm.202402059.

[107] G. Baishya *et al.*, “Advancements in nanocomposite hydrogels: a comprehensive review of biomedical applications,” *Discov Mater*, vol. 4, no. 1, p. 40, Aug. 2024, doi: 10.1007/s43939-024-00111-8.

[108] H. Caballero-Flores *et al.*, “Development and characterization of a new chitosan-based scaffold associated with gelatin, microparticulate dentin and genipin for endodontic regeneration,” *Dental Materials*, vol. 37, no. 7, pp. e414–e425, Jul. 2021, doi: 10.1016/j.dental.2021.03.016.

[109] M. Dallos Ortega *et al.*, “3D printable gelatin/nisin biomaterial inks for antimicrobial tissue engineering applications,” *Mater Adv*, vol. 5, no. 19, pp. 7729–7746, 2024, doi: https://doi.org/10.1039/d4ma00544a.

[110] R. Huang, W. Tai, M. Ho, and P. Chang, “Combination of a biomolecule-aided biphasic cryogel scaffold with a barrier membrane adhering PDGF-encapsulated nanofibers to promote periodontal regeneration,” *J Periodontal Res*, vol. 55, no. 4, pp. 529–538, Aug. 2020, doi: 10.1111/jre.12740.

[111] J.-W. Kim, Y.-S. Han, H.-M. Lee, J.-K. Kim, and Y.-J. Kim, “Effect of Morphological Characteristics and Biomineralization of 3D-Printed Gelatin/Hyaluronic Acid/Hydroxyapatite Composite Scaffolds on Bone Tissue Regeneration,” *Int J Mol Sci*, vol. 22, no. 13, p. 6794, Jun. 2021, doi: 10.3390/ijms22136794.

[112] J. Han, W. Jeong, M.-K. Kim, S.-H. Nam, E.-K. Park, and H.-W. Kang, “Demineralized Dentin Matrix Particle-Based Bio-Ink for Patient-Specific Shaped 3D Dental Tissue Regeneration,” *Polymers (Basel)*, vol. 13, no. 8, p. 1294, Apr. 2021, doi: 10.3390/polym13081294.

[113] X. Liu *et al.*, “A biodegradable multifunctional nanofibrous membrane for periodontal tissue regeneration,” *Acta Biomater*, vol. 108, pp. 207–222, May 2020, doi: 10.1016/j.actbio.2020.03.044.

[114] S. Dong *et al.*, “A Novel Therapeutic Calcium Peroxide Loaded Injectable Bio-adhesive Hydrogel Against Periodontitis,” *Int Dent J*, Aug. 2024, doi: 10.1016/j.identj.2024.05.013.

[115] F. Oustadi, R. Imani, M. Haghbin Nazarpak, and A. M. Sharifi, “Genipin-crosslinked gelatin hydrogel incorporated with PLLA-nanocylinders as a bone scaffold: Synthesis, characterization, and mechanical properties evaluation,” *Polym Adv Technol*, vol. 31, no. 8, pp. 1783–1792, Aug. 2020, doi: 10.1002/pat.4905.

[116] Y. Dou *et al.*, “A hierarchical scaffold with a highly pore-interconnective 3D printed PLGA/n-HA framework and an extracellular matrix like gelatin network filler for bone regeneration,” *J Mater Chem B*, vol. 9, no. 22, pp. 4488–4501, 2021, doi: 10.1039/D1TB00662B.

[117] C.-K. Sun, C.-J. Ke, Y.-W. Lin, F.-H. Lin, T.-H. Tsai, and J.-S. Sun, “Transglutaminase Cross-Linked Gelatin-Alginate-Antibacterial Hydrogel as the Drug Delivery-Coatings for Implant-Related Infections,” *Polymers (Basel)*, vol. 13, no. 3, p. 414, Jan. 2021, doi: 10.3390/polym13030414.

[118] D. I. Hutomo *et al.*, “The Effect of Carbodiimide Crosslinkers on Gelatin Hydrogel as a Potential Biomaterial for Gingival Tissue Regeneration,” *Gels*, vol. 10, no. 11, p. 674, Oct. 2024, doi: 10.3390/gels10110674.

[119] M. A. Ntrivala *et al.*, “Polycaprolactone (PCL): the biodegradable polyester shaping the future of materials – a review on synthesis, properties, biodegradation, applications and future perspectives,” *Eur Polym J*, vol. 234, p. 114033, Jun. 2025, doi: 10.1016/j.eurpolymj.2025.114033.

[120] C. Wang *et al.*, “Polycaprolactone strengthening gelatin/nano-hydroxyapatite composite biomaterial inks for potential application in extrusion-based 3D printing bone scaffolds,” *Collagen and Leather*, vol. 6, no. 1, p. 27, Dec. 2024, doi: 10.1186/s42825-024-00170-w.

[121] Z. Mirzavandi, S. A. Poursamar, F. Amiri, A. Bigham, and M. Rafienia, “3D printed polycaprolactone/gelatin/ordered mesoporous calcium magnesium silicate nanocomposite scaffold for bone tissue regeneration,” *J Mater Sci Mater Med*, vol. 35, no. 1, p. 58, Sep. 2024, doi: 10.1007/s10856-024-06828-5.

[122] M. Merk, O. Chirikian, and C. Adlhart, “3D PCL/Gelatin/Genipin Nanofiber Sponge as Scaffold for Regenerative Medicine,” *Materials*, vol. 14, no. 8, p. 2006, Apr. 2021, doi: 10.3390/ma14082006.

[123] K. Ren, Y. Wang, T. Sun, W. Yue, and H. Zhang, “Electrospun PCL/gelatin composite nanofiber structures for effective guided bone regeneration membranes,” *Materials Science and Engineering: C*, vol. 78, pp. 324–332, Sep. 2017, doi: 10.1016/j.msec.2017.04.084.

[124] E. Malikmammadov, T. E. Tanir, A. Kiziltay, V. Hasirci, and N. Hasirci, “PCL and PCL-based materials in biomedical applications,” *J Biomater Sci Polym Ed*, vol. 29, no. 7–9, pp. 863–893, Jun. 2018, doi: 10.1080/09205063.2017.1394711.

[125] N. Siddiqui, S. Asawa, B. Birru, R. Baadhe, and S. Rao, “PCL-Based Composite Scaffold Matrices for Tissue Engineering Applications,” *Mol Biotechnol*, vol. 60, no. 7, pp. 506–532, Jul. 2018, doi: 10.1007/s12033-018-0084-5.

[126] J. Shen, W. Yuan, M. Badv, A. Moshaverinia, and P. S. Weiss, “Modified Poly(ε-caprolactone) with Tunable Degradability and Improved Biofunctionality for Regenerative Medicine,” *ACS Materials Au*, vol. 3, no. 5, pp. 540–547, Sep. 2023, doi: 10.1021/acsmaterialsau.3c00027.

[127] M. Yang, X. Gao, Z. Shen, X. Shi, and Z. Lin, “Gelatin-assisted conglutination of aligned polycaprolactone nanofilms into a multilayered fibre-guiding scaffold for periodontal ligament regeneration,” *RSC Adv*, vol. 9, no. 1, pp. 507–518, 2019, doi: 10.1039/C8RA09073D.

[128] Z. Tian *et al.*, “Potential of Trilayered Gelatin/Polycaprolactone Nanofibers for Periodontal Regeneration: An In Vitro Study,” *Int J Mol Sci*, vol. 26, no. 2, p. 672, Jan. 2025, doi: 10.3390/ijms26020672.

[129] Allevi Support, “Print Parameter Optimization Guide.” Accessed: Jul. 28, 2025. [Online]. Available: https://www.allevi3d.com/print-parameter-optimization/

[130] VIEWEG, “Dispensing tip tapered, red.” Accessed: Aug. 02, 2025. [Online]. Available: https://dosieren.de/en/products/dispensing-tips/tapered/501610/dispensing-tip-tapered-red

[131] C. Zhuang, F. Tao, and Y. Cui, “Anti-degradation gelatin films crosslinked by active ester based on cellulose,” *RSC Adv*, vol. 5, no. 64, pp. 52183–52193, 2015, doi: 10.1039/C5RA04808G.

[132] R. Nuryanto, W. Trisunaryanti, I. I. Falah, and Triyono, “Extraction of gelatin from catfish bone using NaOH and its utilization as a template on mesoporous silica alumina,” *IOP Conf Ser Mater*

Sci Eng, vol. 349, p. 012051, Apr. 2018, doi: 10.1088/1757-899X/349/1/012051.

[133] M. Azizi, M. Azimzadeh, M. Afzali, M. Alafzadeh, and S. Mirhosseini, “Characterization and optimization of using calendula officinalis extract in fabrication of polycaprolactone-gelatin electrospun nanofibers for wound dressing applications,” vol. 6, pp. 31–38, Sep. 2018.

[134] A. Haryńska, J. Kucinska-Lipka, A. Sulowska, I. Gubanska, M. Kostrzewa, and H. Janik, “Medical-Grade PCL Based Polyurethane System for FDM 3D Printing—Characterization and Fabrication,” *Materials*, vol. 12, no. 6, p. 887, Mar. 2019, doi: 10.3390/ma12060887.

[135] M. Ozmatara, M. Ozpolat, and T. Gevrek, “Synthesis and characterization of gelatin-based quaternizable hydrogels,” *Araştırma Makalesi* , vol. 27, no. 1, 2025, doi: 10.25092/baunfbed.1571324.

[136] J. Šebek, R. Knaanie, B. Albee, E. O. Potma, and R. B. Gerber, “Spectroscopy of the C–H Stretching Vibrational Band in Selected Organic Molecules,” *J Phys Chem A*, vol. 117, no. 32, pp. 7442–7452, Aug. 2013, doi: 10.1021/jp4014674.

[137] N. Mobaraki and B. Hemmateenejad, “Structural characterization of carbonyl compounds by IR spectroscopy and chemometrics data analysis,” *Chemometrics and Intelligent Laboratory Systems*, vol. 109, no. 2, pp. 171–177, Dec. 2011, doi: 10.1016/j.chemolab.2011.08.011.

[138] M. M. Eid, “Characterization of Nanoparticles by FTIR and FTIR-Microscopy,” in *Handbook of Consumer Nanoproducts*, Singapore: Springer Singapore, 2021, pp. 1–30. doi: 10.1007/978-981-15-6453-6_89-1.

[139] J. De Meutter and E. Goormaghtigh, “Amino acid side chain contribution to protein FTIR spectra: impact on secondary structure evaluation,” *European Biophysics Journal*, vol. 50, no. 3–4, pp. 641–651, May 2021, doi: 10.1007/s00249-021-01507-7.

[140] N. Nagy, “Contact Angle Determination on Hydrophilic and Superhydrophilic Surfaces by Using *r* –θ-Type Capillary Bridges,” *Langmuir*, vol. 35, no. 15, pp. 5202–5212, Apr. 2019, doi: 10.1021/acs.langmuir.9b00442.

[141] S. Bom, M. Carvalho, L. F. Gouveia, P. Pinto, H. M. Ribeiro, and J. Marto, “A Comprehensive Rheological and Texture Protocol to Optimize an Extrusion-Based 3D Printing Process,” 2024, pp. 131–135. doi: 10.1007/978-3-031-67217-0_29.

[142] K. Zhang, K. Xue, and X. J. Loh, “Thermo-Responsive Hydrogels: From Recent Progress to Biomedical Applications,” *Gels*, vol. 7, no. 3, p. 77, Jun. 2021, doi: 10.3390/gels7030077.

[143] S. Bom, R. Ribeiro, H. M. Ribeiro, C. Santos, and J. Marto, “On the progress of hydrogel-based 3D printing: Correlating rheological properties with printing behaviour,” *Int J Pharm*, vol. 615, p. 121506, Mar. 2022, doi: 10.1016/j.ijpharm.2022.121506.

[144] J. L. Barrera Bernal, Í. Gaytán Salvatella, B. I. M. del Campo, M. A. Alvarez Perez, and D. Masuoka-Ito, “Synthesis of Hydroxyapatite-Gelatin Composite Hydrogel for Bone Tissue Application,” *Gels*, vol. 11, no. 8, p. 630, Aug. 2025, doi: 10.3390/gels11080630.

[145] S. Mortazavi-Derazkola, M. Reza Naimi-Jamal, and S. Masoumeh Ghoreishi, “Synthesis, Characterization, and Atenolol Delivery Application of Functionalized Mesoporous Hydroxyapatite Nanoparticles Prepared by Microwave-Assisted Co-precipitation Method,” *Curr Drug Deliv*, vol. 13, no. 7, pp. 1123–1129, Oct. 2016, doi:

10.2174/1567201813666160321115543.

[146] I. Grigoraviciute-Puroniene, A. Zarkov, K. Tsuru, K. Ishikawa, and A. Kareiva, “A novel synthetic approach for the calcium hydroxyapatite from the food products,” *J Solgel Sci Technol*, vol. 91, no. 1, pp. 63–71, Jul. 2019, doi: 10.1007/s10971-019-05020-4.

[147] S. Kuśnieruk, J. Wojnarowicz, A. Chodara, T. Chudoba, S. Gierlotka, and W. Lojkowski, “Influence of hydrothermal synthesis parameters on the properties of hydroxyapatite nanoparticles,” *Beilstein Journal of Nanotechnology*, vol. 7, pp. 1586–1601, Nov. 2016, doi: 10.3762/bjnano.7.153.

[148] T. Friščić, “New opportunities for materials synthesis using mechanochemistry,” *J Mater Chem*, vol. 20, no. 36, p. 7599, 2010, doi: 10.1039/c0jm00872a.

[149] S. Pramanik, A. K. Agarwal, K. N. Rai, and A. Garg, “Development of high strength hydroxyapatite by solid-state-sintering process,” *Ceram Int*, vol. 33, no. 3, pp. 419–426, Apr. 2007, doi: 10.1016/j.ceramint.2005.10.025.

[150] H. Oginuma, K. Kondoh, T. Yamaguchi, and E. Yuasa, “Solid-State Synthesis of Magnesium Silicide via Repeated Plastic Working and Spark Plasma Sintering,” *Materials Science Forum*, vol. 475–479, pp. 2895–2898, Jan. 2005, doi: 10.4028/www.scientific.net/MSF.475-479.2895.

[151] S. A. Hutchens, R. S. Benson, B. R. Evans, H. M. O’Neill, and C. J. Rawn, “Biomimetic synthesis of calcium-deficient hydroxyapatite in a natural hydrogel,” *Biomaterials*, vol. 27, no. 26, pp. 4661–4670, Sep. 2006, doi: 10.1016/j.biomaterials.2006.04.032.

[152] M. A. M. Castro *et al.*, “Synthesis of hydroxyapatite by hydrothermal and microwave irradiation methods from biogenic calcium source varying pH and synthesis time,” *Boletín de la Sociedad Española de Cerámica y Vidrio*, vol. 61, no. 1, pp. 35–41, Jan. 2022, doi: 10.1016/j.bsecv.2020.06.003.

[153] P. Agalya *et al.*, “One-pot ultrasonic-assisted synthesis of magnetic hydroxyapatite nanoparticles using mussel shell biowaste with the aid of trisodium citrate,” *Ceram Int*, vol. 48, no. 19, pp. 28299–28307, Oct. 2022, doi: 10.1016/j.ceramint.2022.06.137.

[154] I. D. Rojas-Montoya *et al.*, “Effect of pH on hydroxyapatite coatings obtained by spray pyrolysis and their use as matrices for antibiotic adsorption by spin coating and release properties,” *J Biomed Mater Res B Appl Biomater*, vol. 112, no. 9, Sep. 2024, doi: 10.1002/jbm.b.35470.

[155] P. R. Dev, C. P. Anand, D. S. Michael, and P. Wilson, “Hydroxyapatite coatings: a critical review on electrodeposition parametric variations influencing crystal facet orientation towards enhanced electrochemical sensing,” *Mater Adv*, vol. 3, no. 21, pp. 7773–7809, 2022, doi: 10.1039/D2MA00620K.

[156] W.-L. Yu, C.-C. Lin, L. Hong, Yaping Zhao, and Qun-Li Rao, “Rapid and continuous synthesis of carbonated hydroxyapatite in supercritical water,” *Chinese Journal of Inorganic Chemistry*, vol. 24, no. 9, pp. 1539–1542, 2008.

[157] S. M. M. Gamal, M. M. Bilal, and S. Soheir El-Sayed El, “Evaluation of the effectiveness of hyaluronic acid plus nanohydroxyapatite versus nanohydroxyapatite alone on bone regeneration in rabbits,” *Tanta Dental Journal*, vol. 19, no. 2, pp. 77–83, Apr. 2022, doi: 10.4103/tdj.tdj_32_21.

[158] A. Karthika, “Biocompatible iron and copper incorporated nanohydroxyapatite coating for

biomedical implant applications," *Mater Today Proc*, vol. 51, pp. 1754–1759, 2022, doi: 10.1016/j.matpr.2020.12.813.

[159] M. Hajinaebi, M. Ganjali, and N. A. Nasab, "Antibacterial Activity and Drug Release of Ciprofloxacin Loaded PVA-nHAp Nanocomposite Coating on Ti-6Al-4 V," *J Inorg Organomet Polym Mater*, vol. 32, no. 9, pp. 3521–3532, Sep. 2022, doi: 10.1007/s10904-022-02361-6.

[160] L. Sinusaite *et al.*, "Fe and Zn co-substituted beta-tricalcium phosphate (β-TCP): Synthesis, structural, magnetic, mechanical and biological properties," *Materials Science and Engineering: C*, vol. 112, p. 110918, Jul. 2020, doi: 10.1016/j.msec.2020.110918.

[161] L. Rodrigues, C. Dias, F. Monteiro, and C. Zavaglia, "SYNTHESIS OF HA AND BETA-TCP USING SOL-GEL PROCESS AND ANALYSIS WITH FTIR ," *Copyright © 2011 by ABCM 21st Brazilian Congress of Mechanical Engineering* , 2011.

[162] I. Roohani *et al.*, "Low-Temperature Synthesis of Hollow β-Tricalcium Phosphate Particles for Bone Tissue Engineering Applications," *ACS Biomater Sci Eng*, vol. 8, no. 5, pp. 1806–1815, May 2022, doi: 10.1021/acsbiomaterials.1c01018.

[163] D. Choi and P. N. Kumta, "Mechano-chemical synthesis and characterization of nanostructured β-TCP powder," *Materials Science and Engineering: C*, vol. 27, no. 3, pp. 377–381, Apr. 2007, doi: 10.1016/j.msec.2006.05.035.

[164] K. Hashimoto, M. Baba, H. Shibata, and K. Yoshida, "Enhanced sinterability and mechanical strength of beta-type tricalcium phosphates ceramics through reaction sintering with hydroxyapatite," *J Eur Ceram Soc*, vol. 45, no. 4, p. 117023, Apr. 2025, doi: 10.1016/j.jeurceramsoc.2024.117023.

[165] B. Mirhadi, "Microwave sintering of nano size powder β-TCP bioceramics," *Science of Sintering*, vol. 46, no. 2, pp. 185–193, 2014, doi: 10.2298/SOS1402185M.

[166] M. Bielec, A. Huang, Y. Xia, and H. Dai, "Microemulsion Synthesis of Mesoporous β-tricalcium Phosphate Powder with a Novel System," *Journal of Wuhan University of Technology-Mater. Sci. Ed.*, vol. 37, no. 4, pp. 773–778, Aug. 2022, doi: 10.1007/s11595-022-2595-y.

Appendix I

Table 1 – Synthesis methods for HAp NPs.

Methods	Benefits	Limitations	Applications	Ref.
Wet Chemical Synthesis				
Precipitation Reaction	Simple and cost-effective	Limited control over particle size	Biomedical applications, bone regeneration	[145]
Sol-gel Process	Better control over particle size/composition	Use of hazardous solvents	Biomedical applications, drug delivery, coatings	[146]
Hydrothermal Synthesis	High crystallinity, well-defined structures, and cost-effective	High temperature and pressure → high energy consumption	Targeted drug delivery in bone-related diseases	[147]
Solid State Reactions				
Mechanochemical Synthesis	Solvent-free and energy-efficient	Longer processing times	Porous materials, MOFs	[148]
Sintering				
Solid-state Sintering	Simple and cost-effective	High temperatures, long processing times	Dense, high-strength structures	[149]
Spark Plasma Sintering	Rapid densification, fine microstructures	Expensive equipment, not suitable for large-scale production	Improved electrical properties	[150]
Biomimetic Synthesis				

Methods	Benefits	Limitations	Applications	Ref.
Biomineralization	Biomimetic, controlled organization	Complex interactions, optimization required	Tissue repair, drug delivery systems	[151]
Template-assisted synthesis	Uniform particle distribution, reduced variability	Template Removal	Biomimetic scaffolds for bone tissue engineering	[151]
Alternative Methods				
Microwave-assisted synthesis	Rapid synthesis, uniform particles, energy-efficient	Specialized equipment; scale-up challenges	Biomedical coatings, nano-HAp for drug delivery	[152]
Ultrassound-assisted synthesis	Enhanced nucleation, reduced agglomeration	Equipment cost, scalability limitations	Nanostructured materials, injectable systems	[153]
Spray Pyrolysis	Continuous process, morphology control	High energy input, complex setup	Industrial-scale HAp, composite powders	[154]
Electrochemical Deposition	Localized deposition, mild conditions	Limited to surface coatings, slow rate	Orthopedic and dental implant coatings	[155]
Supercritical Fluid Synthesis	Green process, tunable particle morphology	High-pressure equipment, costly	High-purity HAp for biomedical and analytical use	[156]

Table 2 – Systematic review of HAp NPs advancements in periodontal pathologies treatment.

NPs	Type of Study	Aim of the Study	Conclusion	Ref.
Si-HAp	*in vitro*	Fabricate a bilayer nanocomposite membrane with a	Novel bilayer nanocomposite	[26]

NPs	Type of Study	Aim of the Study	Conclusion	Ref.
		microporous sublayer composed of chitosan and Si-HAp NPs and a chitosan/polyethylene upper layer.	membranes can be utilized for guided bone regeneration in periodontal applications.	
PA6/CS@HAp/PA6	*in vitro*	Design a novel bilayered membrane to reinforce the mechanical properties of HAp/PA6 composite scaffolds.	Scaffolds exhibited good bioactivity, biocompatibility, and osteoconductivity for bone regeneration.	[27]
HLA-HAp	Animal Study	Compare histologically the bone regenerative ability of the combination of hyaluronic acid with HAp NPs.	Both groups showed bone formation, but with the HLA + HAp group, the bone formation was improved.	[157]
Fe/Cu-HAp	*in vitro*	Develop and assess for biocompatibility and antibacterial activity Fe (III) and Cu (II) incorporated hydroxyapatite coatings (Fe/Cu-HAp) on titanium implants.	The coating on the implant showed uniform deposition with improved biocompatibility and bioactivity. The coating improved antibacterial activity.	[158]
CIP-HAp	*in vitro*	Coat Ti-6Al-4V implants with CIP-HAp to enhance the antibacterial properties of the surface.	The implant showed a crack-free homogenous coating on the surface with sustained release of CIP. The antibacterial activity was enhanced.	[159]
HAp-CMC	*in vitro*	Assess odontogenic differentiation capabilities of porous bio-mineralizable composite scaffolds with eggshell-	PSCs on 1:5 HAp-CMC scaffolds showed enhanced cell viability and	[28]

NPs	Type of Study	Aim of the Study	Conclusion	Ref.
		derived HAp and CMC on dental pulp stem cells.	proliferation along with increased expression of DSPP as well as VEGF.	
B-HAp	*in vitro*	Osteogenic potential of PEEK implants coated with boron-doped HAp on periodontal ligament cells.	Enhanced periodontal ligament cell adhesion and proliferation on the surface of PEEK implants coated with boron-doped HAp compared with untreated PEEK implants.	[29]
GHMS-HAp	*in vitro*	Produce a scaffold using gelatine, nano-hydroxyapatite, and metformin(GHMS) and study its effectiveness in bone regeneration in a rat alveolar bone defect model.	GHMS showed superior bone regeneration compared to the extraction-only, Sinbone, and Bio-Oss Collagen groups.	[30]

Table 3 – Synthesis methods for Fe-*β*-TCP NPs.

Methods	Benefits	Limitations	Applications	Ref.
Wet Chemical Synthesis				
Co-Precipitation	Simple, cost-effective, and enables ion substitution (e.g. Sr, Zn, Fe).	Broad particle size distribution and agglomeration; post-calcination required.	Powders, scaffolds, composite biomaterials, and doped *β*-TCP.	[160]

Methods	Benefits	Limitations	Applications	Ref.
Sol-gel Process	Homogeneous molecular mixing; fine control of composition and stoichiometry.	Control of synthesis parameters, organic residues, and high temperatures.	Thin films, coatings, and homogeneous *β*-TCP powders for composites.	[161]
Hydrothermal Synthesis	Controlled morphology and porosity; high purity at low temperature; good crystallinity.	Long reaction times; specialized autoclaves required; possible residual surfactants.	Porous NPs for drug delivery and scaffold coatings.	[162]
Solid State Reactions				
Mechanochemical Synthesis	Solvent-free, suitable for large-scale production; effective mixing of solid precursors.	High temperature; risk of contamination from milling.	*β*-TCP powders and ion-substituted phases for bone substitutes.	[163]
Sintering				
Solid-state Sintering	Simple and scalable; produces dense and strong *β*-TCP ceramics.	High temperature and processing time; grain growth reduces bioresorbability.	Fabrication of dense *β*-TCP scaffolds and structural bioceramics.	[164]
Microwave-Assisted Sintering	Rapid densification; finer grain microstructures; reduced energy consumption.	Requires a dedicated microwave system; possible non-uniform heating.	Porous *β*-TCP scaffolds and biodegradable coatings.	[165]
Template-Assisted Methods				
Microemulsion / Template-	Control of pore size and structure; high surface area.	Complex process; removal of templates; scalability limited.	Drug delivery, tissue engineering scaffolds.	[166]

Methods	Benefits	Limitations	Applications	Ref.
Assisted Synthesis				
Biomimetic Methods				
One-Pot Low-Temperature Synthesis	Energy-efficient; enables hollow or uniform *β*-TCP; high cytocompatibility.	Sensitive system, possible incomplete conversion.	Injectable NPs, ion-releasing carriers for osteogenis.	[162]

Table 4 – Systematic review of gelatin-based hydrogels and their mechanisms of action in periodontal treatment.

Components	Gelling method	Mechanism of Action	Osteointegration	Antibacterial	Ref.
Gelatin-Chitosan genipin	Crosslinking by genipin and freeze-drying	Porous structures are essential for cell adhesion and proliferation.	Created a suitable microenvironment for tissue regeneration.	Group Ch presented lower CFU/mL on day 6, interfering with bacterial growth.	[108]
Gelatin/nisin	Temperature crosslinking	Disrupts bacterial cell membranes and maintains a sterile environment.	Created a 3D structure for tissue regeneration.	Showed complete efficacy against Staphylococcus aureus and Pseudomonas aeruginosa.	[109]
Gelatin-HAp	Temperature crosslinking	Mimic the extracellular matrix, promoting osteogenesis and cementogenesis.	HAp further enhances osteogenesis, leading to improved periodontal	Does not explicitly mention antibacterial properties.	[110]

Components	Gelling method	Mechanism of Action	Osteointegration	Antibacterial	Ref.
			regeneration.		
Gelatin-HA-HAp	Temperature crosslinking and biomineralization	Provides a conducive microenvironment for cell attachment, proliferation, and differentiation, with HAp enhancing the bioactivity.	Scaffolds with specific structural configurations (like GEHA20-ZZS and GEHA20-45S) showed higher bioactivity, indicating better potential for osteointegration.	Does not explicitly mention antibacterial properties.	[111]
Gelatin-Fibrinogen	Temperature crosslinking	3-D printed scaffold in bio-ink promotes odontogenic differentiation of dental pulp.	The presence of collagen facilitates the integration of the bio-ink with the surrounding bone tissue.	Does not explicitly mention antibacterial properties.	[112]
Gelatin-PLGA-HAp	Treatment with a 95% ethanol solution of EDC and NHS	Mimics the extracellular matrix, facilitating cell adhesion and proliferation in the early stages.	Scaffolds promoted new bone formation and achieved a tighter bond between the scaffold and the original tissue.	Does not explicitly mention antibacterial properties.	[116]
Gelatin-PLA-MgO	Electrospinning	Creates a favorable pH environment for proliferation and produces ROS to inhibit bacterial growth.	*In vitro* studies showed that nMgO enhances osteogenic differentiation.	Hydrogel suppresses bacterial growth by over 90% within 24 hours, in *E. coli* and *S. aureus*.	[113]
Gelatin-PLLA genipin	Crosslinking by genipin	Enhances the mechanical properties of the gelatin	Scaffolds are designed to mimic the natural bone	Does not explicitly mention antibacterial properties.	[115]

Components	Gelling method	Mechanism of Action	Osteointegration	Antibacterial	Ref.
		hydrogel, making it suitable for use as a bone scaffold.	matrix, and PLLA supports cell growth and activity.		
Gelatin-CaO_2	Oxidized dextran	Delivery of antibiotics creates a favorable environment that inhibits bacterial proliferation and promotes healing.	The alkaline environment created by the hydrogel promotes osteogenic differentiation.	Exhibits strong antibacterial properties, particularly against *Porphyromonas gingivalis*.	[114]
Gelatin-Alginate	Transglutaminase crosslinking	Slow-release system for antibiotics, encapsulated within the hydrogel.	Significant improvements in bone volume and structure compared to the control group.	Effective against methicillin-resistant *Staphylococcus aureus* and other bacterial strains.	[117]

Appendix II

Cytocompatibility assay

MG-63 osteoblastic cells

MG-63 osteoblastic cells (ATCC®CRL-1427TM; ATCC, Manassas, USA) were seeded at $5x10^3$ cell/cm^2 in culture medium (basal medium) composed of α-Minimal Essential Medium (α-MEM), 10% fetal bovine serum (FBS), penicillin (100 UI/mL), streptomycin (100 µg/mL), and amphotericin B (0.25 µg/mL, all from Gibco, in 96- and 24-well plates. After 24 hours, the medium was exchanged to basal medium containing HAp, Fe-*β*-TCP, and $CaCO_3$ particles at different concentrations (1, 5, 10, 25, 50, and 100 µg/mL) for periods up to 7 days. The basal medium was used as a control. The cultures were characterized for metabolic activity, alkaline phosphatase (ALP) activity, and DNA content.

Metabolic activity

Metabolic activity was determined by the MTT assay (3-(4,5-dimethylthiazol-2-yl)-2,5-diphenyltetrazolium bromide), based on the reduction of MTT to a purple formazan product by viable cells, on days 1, 4, and 7 for the MG-63 cell cultures and on days 4 and 7 for BM-MSC cultures. The MTT solution (5 mg/mL, Sigma-Aldrich) was added, and the cultures were incubated at 37 ºC, in a humidified atmosphere with 5% CO_2, for 3 hours. Then, the culture medium was removed, and the formazan crystals were dissolved with dimethyl sulfoxide (DMSO, Panreac), and the absorbance was determined at 550 nm in a microplate reader (Synergy HT, BioTeK).

DNA content

Total DNA content was assessed during the culture times. Cells were lysed with 0.1% Triton X-100 (Sigma–Aldrich) for 30 min, and DNA was measured using the Quant-iTTM PicoGreenTM dsDNA Assay kit (Thermo Fisher Scientific), according to the manufacturer's instructions. Fluorescence was measured at 480 nm (excitation) and 528 nm (emission) in a microplate reader (Synergy HT, BioTek). The assay was conducted in triplicate.

TEM analysis

Cultures of BM-MSCs exposed to Hap and Fe-*β*-TCP were characterized by TEM to assess particle internalization. The cells were seeded at $2x10^4$ cells/cm^2 in a 24-well plate and, after 48 hours, they were exposed to Hap and Fe-*β*-TCP (50 µg/mL) for 24 hours. Then, the cells were detached with TrypLE (Gibco) and centrifuged, washed three times with PBS, fixed (2.5% glutaraldehyde with 2% formaldehyde), and post-fixed (1% osmium tetroxide). Ultra-thin sections (50 nm) were prepared on an RMC Ultramicrotome (PowerTome) using Diatome diamond knives and mounted on mesh copper grids. The grids were stained with uranyl acetate and lead citrate for TEM analysis. Samples were photo documented by JEOL JEM 1400 transmission electron microscope (JEOL, Japan).

ALP activity

ALP activity was determined on days 4 and 7 for MG-63 cells and BM-MSCs. After solubilizing the cell layers with 0.1% Triton X-100 for 30 min, the cell lysates were assessed for ALP activity by the hydrolysis of p-nitrophenyl phosphate (pNPP, Sigma-Aldrich) in an alkaline buffer solution (pH 10) for 1 hour at 37 ºC. The absorbance of p-nitrophenol was determined at 400 nm in a microplate reader (Synergy HT BioTek). ALP levels were normalized to total protein content (DCTM Protein Assay; BioRad), and ALP activity was expressed as nanomoles of p-nitrophenol per microgram of protein (nmol/µg) (ALP/PT).

Statistical Analysis

Results were presented as mean ± standard deviation of three independent experiments, with three replicas each. Statistical analysis was performed by one-way analysis of variance, in combination with Tukey's post hoc test. Values of $p < 0.05$ were considered significant.